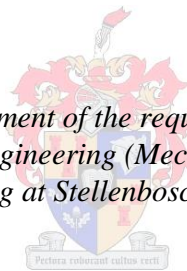


Thermal performance evaluation of artificial protective coatings applied to steam surface condenser tubes

by
John Goodenough

*Thesis presented in fulfilment of the requirements for the degree of
Master of Science in Engineering (Mechanical) in the Faculty of
Engineering at Stellenbosch University*



Supervisor: Prof. Hanno Carl Rudolf Reuter

December 2013

Declaration

By submitting this thesis electronically, I declare that the entirety of the work contained therein is my own, original work, that I am the sole author thereof (save to the extent explicitly otherwise stated), that reproduction and publication thereof by Stellenbosch University will not infringe any third party rights and that I have not previously in its entirety or in part submitted it for obtaining any qualification.

Signature:
J. Goodenough

Date: 2013/09/13

Copyright © 2013 Stellenbosch University
All rights reserved.

Abstract

The coating thermal conductivity, the effective coated-tube thermal conductivity and the coating factor of three artificial protective coatings (APCs) applied to condenser tubes are experimentally evaluated. This testing broadens the limited available knowledge of these coatings, which is necessary for effective condenser refurbishment and operation. The coatings are applied to 25.4 mm brass tubes at thicknesses of 44, 46, 50, and 130 μm . Steady state heat transfer tests are performed on these tubes fitted in a double-pipe counter-flow heat exchanger, with heated water in the annulus and cooling water inside the tube. The experimentally determined thermal conductivities of the coatings range from 0.5 to 2.3 $\text{W/m}\cdot\text{K}$. The effective coated-tube conductivity and the coating factor depend on the tube material and size, as well as the coating thickness. A one-dimensional condenser model is used to parametrically investigate the relative overall effect on condenser performance. From these results, coating guidelines for Admiralty brass tubes are proposed in terms of the minimum and maximum coating conductivity and thickness. The effect of the coating on the thermal performance is equivalent to a Heat Exchange Institute (HEI) cleanliness factor of at least 0.85, when adhering to these guidelines. APCs provide a layer of protection against corrosion, erosion and fouling and can preferentially fill tube-wall pits. They can therefore be used to extend the condenser life-span effectively, but, to ensure minimal impact on the overall condenser performance, the coating thickness and conductivity must be carefully controlled and verified experimentally.

Keywords: Steam surface condensers, coatings, performance, modeling, thermal conductivity, effective conductivity, fouling, corrosion.

Uittreksel

Die termiese geleidingsvermoë, die effektiewe termiese geleidingsvermoë van bedekte buise en die bedekkingsfaktor van drie kunsmatige beskermingsbedekkingslae wat op kondensorbuisse aangewend word, word eksperimenteel geëvalueer. Hierdie evaluering verbreed die beperkte beskikbare kennis oor sodanige bedekkingslae, wat nodig is vir effektiewe kondensator herinrigting en bedryf. Die lae word teen diktes van 44, 46, 50 en 130 μm in 25.4 mm geelkoperbuisse aangewend. Warmteoordragstoetse by gestadige toestande word gedoen op hierdie buise in 'n dubbelpyp-teenvloei-warmteoordraer, met verhitte water in die annulus en verkoelingswater binne-in die buis. Die eksperimenteel bepaalde termiese geleidingkoëffisiënte wissel tussen 0.5 tot 2.3 $\text{W}/\text{m}\cdot\text{K}$. Die effektiewe geleidingsvermoë en bedekkingsfaktor hang af van sowel die buis se materiaal en grootte sowel as die dikte van die bedekkings. 'n Eendimensionele kondensormodel word gebruik om die algehele effek van hierdie beskermingsbedekkingslae op kondensatorwerkverrigting parametries te ondersoek. Riglyne ten opsigte van aanwending van beskermingslae vir buise van "Admiralty" geelkoper word verskaf in terme van die minimum en maksimum geleidingsvermoë en dikte van bedekkingslae. Met behulp van hierdie riglyne word 'n "Heat Exchange Institute" (HEI) ekwivalente skoonheidsfaktor van minstens 0.85 op 'n nuwe buis behaal. Hierdie kunsmatige bedekkingslaeslae bied beskerming teen korrosie, erosie en bevuilding en kan klein kuile in die buiswand vul. Hulle kan dus gebruik word om die lewensduur van die kondensator te verleng, maar hul dikte en geleidingsvermoë moet noukeurig beheer word en moet eksperimenteel geverifieer word.

Sleutelwoorde: Stoom-oppervlakkondensators, beskermingslae, werkverrigting, modelering, termiese geleidingsvermoë, effektiewe geleidingsvermoë, aanpaksel, korrosie

Acknowledgments

I would like to express my sincere gratitude to:

My supervisor Prof. Hanno Reuter for his continued support, guidance, friendship and patience for over two years. In which time, he continually challenged me to exceed expectations, through critical thinking and outstanding mentoring.

My parents for their sponsorship, support, understanding and interest in this thesis. My father who instilled a relentless determination in me to solve engineering problems and to whom I look up to. My sister and brother-in law who found time to assist me whenever necessary.

Members of Eskom including Francois du Preez, Keith Northcott and Wiets Roos, all of whom were instrumental in helping me complete this thesis.

Contents

	Page
Declaration	i
Abstract	ii
Uittreksel	iii
Acknowledgments	iv
Contents	v
List of figures	viii
List of tables	x
Nomenclature	xii
1 Introduction	1
1.1 Fundamentals of power generation based on the Rankine power cycle	1
1.2 Direct versus indirect condensers	4
1.3 Description and operation of a vacuum steam surface condenser . . .	5
1.4 Degradation mechanisms affecting condenser tubes	6
1.5 Combating degradation of condenser tubes	9
1.6 Artificial protective coatings applied to condenser tubes	11
1.7 Motivation for this study	13
1.8 Objectives	14
1.9 Thesis outline	14
2 Applicable theory	16
2.1 Introduction to heat exchanger analysis	16
2.2 Electrical resistance analogy and the overall heat transfer coefficient .	19
2.3 Determining the developed turbulent friction factor	21
2.4 Convection correlations	22
2.5 Evaluating the total thermal resistance	25

CONTENTS

2.6	Methods of analyzing coated tubes	26
2.7	Determining the uncertainty in the measured thermal conductivity	28
2.8	Determining the uncertainty in the effective coated-tube conductivity	39
3	Experimental facility	41
3.1	Description of the apparatus	41
3.2	Measurement techniques and instrumentation	44
3.3	Methodology and test procedures	47
4	Experimental testing	51
4.1	Test tube designation and dimensions	51
4.2	Isothermal tests and energy balances	51
4.3	Uncoated tube tests to determine the outer convection coefficient	55
4.4	Coated tube tests to determine the coating performance	57
4.5	Pressure drop results	64
5	Coated condenser modeling	66
5.1	The HEI method of analysis	66
5.2	Thermal resistance method	67
5.3	Results of the parametric study	74
5.4	Modifying the HEI method to account for APCs	76
5.5	Coating performance and selection guidelines	77
5.6	Relating the single tube tests to the effect on overall condenser performance	78
5.7	Predicted effect on plant performance	79
6	Conclusion	81
6.1	Conclusions	81
6.2	Recommendations	83
	List of references	84
	Appendices	88
A	Properties of fluids	89
A.1	Thermophysical properties of saturated water	89
A.2	Thermophysical properties of saturated water vapor	90
A.3	Thermophysical properties of mixtures of air and water vapor	90
B	Experimental data	91
B.1	Isothermal tests	91
B.2	Uncoated tube tests	92

CONTENTS

B.3	Coated tube tests	94
C	Condenser modeling	97
C.1	Axial variation in condenser tube wall temperature	97
C.2	Modeling parameters	99
C.3	Steam vapor velocity regression	100
D	Sample calculations	101
D.1	Analysis of uncoated tube 15U	101
D.2	Analysis of coated tube 15C	106
D.3	Calculating the heat transfer coefficient using the HEI method	111
D.4	Calculating γ in the thermal resistance model	112
D.5	Actual turbine data from a particular power station	115
E	Instrument certification	116

List of figures

	Page
1.1 Simplified process diagram of a coal-fired power plant operating using the Rankine cycle with indirect wet-cooling	2
1.2 Temperature-entropy diagrams (isentropic expansion and compression)	3
1.3 Examples of direct and indirect condensers	4
1.4 Simplified schematic of a two pass, single compartment steam surface condenser	5
1.5 Example of pitting corrosion in condenser tubes	8
1.6 Micro-graph of a cross-sectioned coated tube	11
1.7 Micro-graph showing preferential filling of a tube-wall pit by coating . . .	12
1.8 Schematic of the condenser in a case study	13
2.1 Double-pipe counter-flow heat exchanger	17
2.2 Temperature variation with heat transfer	18
2.3 Analogy between thermal and electrical resistances	19
2.4 Cross-section of double-pipe heat exchanger showing resistance analogy for heat transfer	20
2.5 Illustration of measurement error	29
2.6 Uncertainty interval and error	30
2.7 Systematic elemental errors affecting variable X	31
2.8 Frequency distribution arising from measurements taken from 1 000 similar instruments tested in the absence of random error sources	32
2.9 Uncertainty propagation including the correlated error effects between uncoated and coated tests	37
2.10 Diagram showing correlation terms between temperature measurements during uncoated and coated tests	38
3.1 Schematic of experimental facility	42
3.2 Piping and instrumentation diagram of apparatus	42
3.3 Cross-sectional view of preconditioning annulus (rotated plan view) . . .	43
3.4 Schematic of a thermopile used to measure temperature differential . . .	45
3.5 Annotated photograph of the hot inlet temperature station	45
3.6 Waterbath used to verify Pt 100 RTD resistances	46

LIST OF FIGURES

3.7	Pressure tapping	47
3.8	Valve orientation and pipe flow comprising ‘calibration’ loop (shaded loop shows original configuration)	48
3.9	Measured inlet temperature profiles from a particular test	49
4.1	Energy balance of uncoated and coated tests	55
4.2	Measured Nusselt numbers compared to calculated values	56
4.3	Measured coating thermal conductivity	58
4.4	Uncertainty magnification factors in the thermal conductivity reduction equation (2.37)	60
4.5	Relative systematic uncertainty contributions from each term in equation (2.71)	61
4.6	Average thermal conductivity comparison of coatings	62
4.7	Average effective conductivity and coating factor of three coatings and one scaled tube	63
4.8	Measured friction factor versus Reynolds number	65
5.1	Modes of condensation	68
5.2	Condensation of steam in the presence of non-condensable gases	69
5.3	Model predicted coefficient versus HEI values as a function of velocity	74
5.4	NTU versus effective coated-tube conductivity ratio for different tube materials (18 BWG 1-inch tubing)	75
5.5	Variation in CF with coating thickness and conductivity (Admiralty brass 18 BWG 1-inch tubing)	76
5.6	Coating thickness versus conductivity	78
5.7	Difference in efficiency with coating conductivity and thickness (18 BWG 1-inch admiralty brass, t_c in μm)	80
C.1	Elemental length of condenser tube	97
C.2	Tube spacing in bundle	100
D.1	Power output versus steam temperature from an actual power plant	115

List of tables

	Page
2.1 Thermal conductivities of condenser tubes	26
3.1 Annulus tubing sizes and test tube diameter ranges	44
3.2 Results from water bath validation test	46
3.3 Maximum and minimum flow rates for outer convection coefficient testing	50
4.1 Dimensions of test tubes	52
4.2 Average hot and cold temperature trends during isothermal tests	52
4.3 Isothermal test deviations between absolute RTD reading and arithmetic mean	53
4.4 Comparison of measured temperature differences using two different temperature sensor types	53
4.5 Isothermal test deviations of flow rate measurement from arithmetic mean	54
4.6 Coating schedule of four test tubes	57
4.7 Random uncertainty of the coating conductivity, $s_{\bar{k}_c}$	59
4.8 Systematic uncertainty component estimates	59
4.9 Random uncertainty of the effective coated-tube, $s_{\bar{k}_{eff}}$	64
4.10 Sensitivity of k_c with d_1 compared to sensitivity of k_{eff} with d_1	64
4.11 Length between pressure tappings for the various tubes	64
5.1 γ regression coefficients in equation (5.20)	73
5.2 Tests performed before and after coating of tube 15C	79
6.1 Effective coated-tube conductivities and coating factors	81
6.2 Measured thermal conductivities	82
B.1 Isothermal tests: recorded temperatures and flow rates	91
B.2 Tube 10U: recorded temperatures and flow rates	92
B.3 Tube 10U: Average temperature trends, mean heat transfer, and inner convection coefficient	92
B.4 Tube 15U: recorded temperatures and flow rates	93
B.5 Tube 15U: Average temperature trends, mean heat transfer, and inner convection coefficient	93

LIST OF TABLES

B.6	Tube 10C: recorded temperatures and flow rates	94
B.7	Tube 10C: processed heat transfer data	94
B.8	Tube 11C: recorded temperatures and flow rates	94
B.9	Tube 11C: processed heat transfer data	95
B.10	Tube 12C: recorded temperatures and flow rates	95
B.11	Tube 12C: processed heat transfer data	95
B.12	Tube 15C: recorded temperatures and flow rates	95
B.13	Tube 15C: processed heat transfer data	96
C.2	Calculated γ values for Admiralty brass and $w = 0.05\%$	100

Nomenclature

Symbols

a	Diameter ratio
A	Area (m^2)
b	Systematic standard uncertainty ($\text{W}/\text{m}\cdot\text{K}$)
c_p	Specific heat at constant pressure ($\text{J}/\text{kg}\cdot\text{K}$)
$CORR$	Correlation term in equation (2.71)
d	Diameter (m)
D_{as}	Diffusion coefficient of water vapor in air (m^2/s)
ϵ	Machine epsilon (2^{-52})
EB	Energy balance
f	Friction factor
F_C	Cleanliness factor
F_M	Material correction factor
F_W	Inlet water temperature correction factor
g	Gravitational constant, 9.81 (m/s^2)
HR	Heat rate ($\text{kJ}/\text{kW}_e\text{h}$)
I	Electric current (A)
i_{fg}	Latent heat of vaporization (J/kg)
k	Thermal conductivity ($\text{W}/\text{m}\cdot\text{K}$)
L	Length (m)
m	Mass flow rate (kg/s)
n	Number of tube vertical tube rows in bundle
NTU	Number of transfer units
p	Static pressure (Pa)
Q	Heat transfer rate (W)
R	Thermal resistance (K/W)
r	Coverage factor, or rate of condensation per unit area ($\text{kgm}^2\cdot\text{s}$)
s	Random standard uncertainty ($\text{W}/\text{m}\cdot\text{K}$)
T	Average/bulk temperature (K)
t	Thickness (μm)

NOMENCLATURE

u	Standard uncertainty (W/m·K)
U	Overall heat transfer coefficient (W/m ² ·K)
U_{HEI}	Corrected overall heat transfer coefficient according to HEI method (W/m ² ·K)
v	Velocity (time averaged) (m/s)
v_{∞}	Vapor velocity based on the maximum flow area
V	Voltage (V), or volumetric flow rate (m ³ /s)
w	Air-steam mass fraction
X	Arbitrary measured variable
i_{fg}^*	Modified latent heat of vaporization (J/kg)
$L_{\Delta P}$	Length between pressure tapings (m)
R''	Fouling factor (m ² ·K/W)
u^+	Expanded uncertainty estimate (W/m·K)
v^+	Modified vapor velocity (m/s)
\bar{k}	Arithmetic mean conductivity (W/m·K)
$\Delta\bar{T}$	Averaged mean temperature difference (K)
F_M^+	Coated material correction factor

Greek letters

α	Elemental error
β	Systematic error
ϵ	Random error
γ	Factor in equation 5.18
ζ	Step size used in numerical differencing
μ	Kinematic viscosity (kg/s.m)
ϕ	Surface roughness (m)
ρ	Density (kg/m ³)
ψ	Void fraction of tube bundle
τ	Shear stress (Pa)

Subscripts

a	Air (non-condensable gas)
ann	Annulus
b	Bulk
c	Coating
ci	Cold inlet
cm	Cold stream mean value
co	Cold outlet
con	Condensate
cw	Cooling water
D	Darcy

NOMENCLATURE

<i>e</i>	Equivalent or hydraulic
<i>eff</i>	Effective
<i>f</i>	Fluid
<i>sh</i>	Shear
<i>h</i>	Convection
<i>hi</i>	Hot inlet
<i>ho</i>	Hot outlet
<i>i</i>	Inner
<i>L</i>	Total number of shared elemental systematic errors
<i>lv</i>	Liquid-vapor interface
<i>m</i>	Mean
<i>o</i>	Outer
<i>p</i>	Condenser pass
<i>s</i>	Steam
<i>t</i>	Tube
<i>th</i>	Thermal
<i>tot</i>	Total
<i>w</i>	Wall or waterside

Dimensionless groups

<i>Nu</i>	Nusselt number, hd/k
<i>Pr</i>	Prandtl number, $\mu c_p/k$
<i>Re</i>	Reynolds number, $\rho v d/\mu$
<i>Re*</i>	Modified Reynolds number



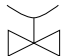
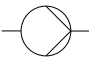
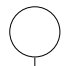
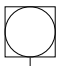
Acronyms

APC	Artificial protective coating
ACTT	Average cold temperature trend
AHTT	Average hot temperature trend
ASME	American Society of Mechanical Engineers
ASTM	American Society of Testing and Materials
BWG	Birmingham wire gage
C	Coated
DRE	Data reduction equation
EMF	Electromotive force
HEI	Heat Exchange Institute
RTD	Resistance temperature detector
S	Scaled
TSM	Taylor series method
T/C	Thermocouple

NOMENCLATURE

TTD Terminal temperature difference
U Uncoated
UMF Uncertainty magnification factor
UPC Mean uncertainty percentage contribution

Process and instrumentation diagram symbols

	Ball valve		Heat exchanger
	Diaphragm control valve		Centrifugal pump
	Local variable measurement		Remote variable measurement

Chapter 1

Introduction

Overview

An introduction to the fundamental thermodynamics of Rankine power cycles is presented, which explains the role of condensers and their influence on power plant performance. After classifying condenser types, a description is given of a vacuum steam surface condenser and its operating principles. The performance degradation mechanisms affecting condenser tubes are discussed and methods of combating these mechanisms are proposed. Artificial protective coatings (APCs) applied to condensers are discussed in terms of previous experience and a case study. Finally the motivation, objectives and scope of work of this thesis are given.

1.1 Fundamentals of power generation based on the Rankine power cycle

Steam power plants operate using a thermodynamic power cycle which is fundamentally based on the Rankine power cycle. Steam may be produced using a number of different heat sources; these may be classified as fossil, nuclear, or renewable. Fossil fuels typically include coal and natural gas. Although controversial, nuclear energy may be considered non-renewable since it requires tritium or uranium, elements which are not replenished as quickly as they are being consumed. Renewable sources may include waste incineration, biomass, solar energy, and geothermal sources. In spite of the numerous heat sources, almost all steam-driven power stations operate using a modified form of the Rankine cycle.

By way of example, consider figure 1.1 which depicts a coal-fired power plant operating using the Rankine cycle with indirect evaporative/wet-cooling.

CHAPTER 1. INTRODUCTION

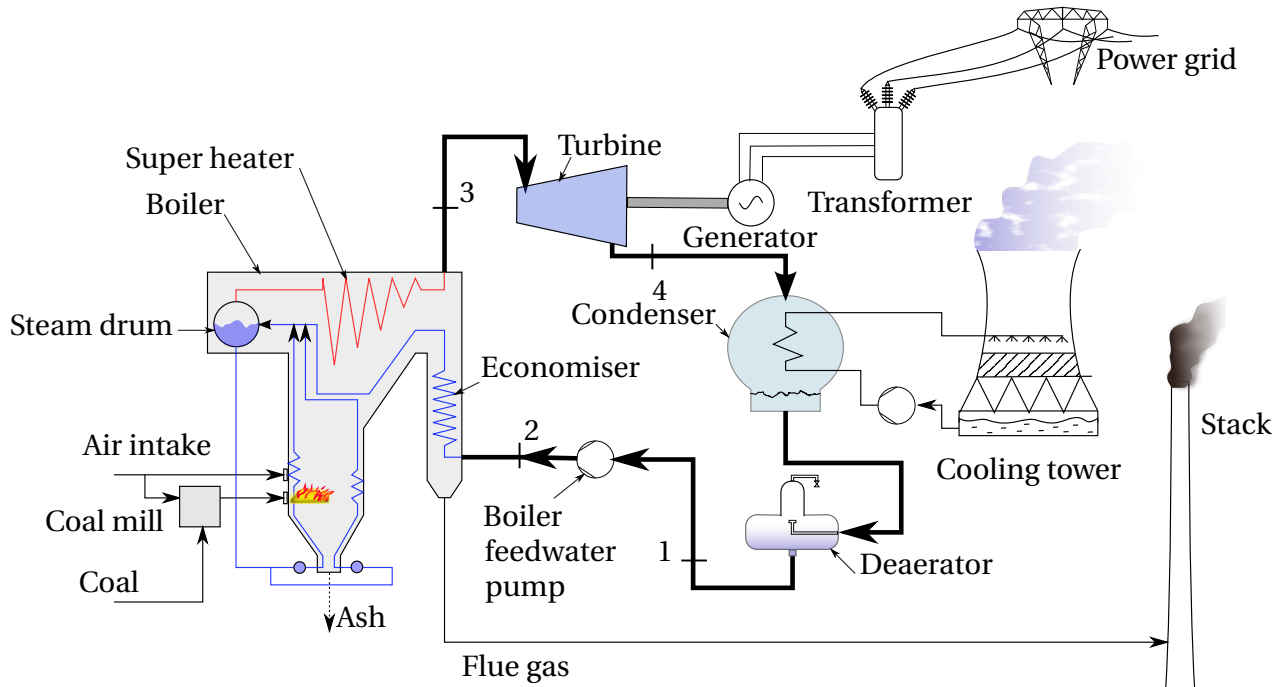


Figure 1.1: Simplified process diagram of a coal-fired power plant operating using the Rankine cycle with indirect wet-cooling

The basic cycle begins by pumping feed water to the boiler (point 1 to 2 in figure 1.1). The water is preheated by the economizer, before passing through the water-wall furnace tubes. The water passing through these tubes is continuously heated until it boils and collects in the steam drum. This saturated steam is then superheated at which point it exits the boiler at point 3.

The resulting super-heated (high-grade) steam then drives a turbine coupled to a generator. The turbine converts the enthalpy of the steam into rotational kinetic energy, which is ultimately converted to electrical energy by the generator. As a consequence of expanding through the turbine, the steam exits at point 4 with a considerably lower enthalpy.

The low-grade steam exiting the turbine is recovered to a liquid state by the condenser, so that it can be pumped back to the boiler. By condensing the vapor, the volumetric flow rate is dramatically reduced so that the least amount of pumping power is required. The steam is condensed at a pressure below atmospheric pressure, in order to afford a greater expansion ratio in the turbine. Therefore, more power can be developed by the cycle. This means the primary function of the condenser is to condense the steam at the lowest possible temperature and hence pressure (within

CHAPTER 1. INTRODUCTION

economic constraints).

The latent heat removed from the steam is rejected by the cooling system to a heat sink. Depending on the type of cooling system, the heat sink may be the hydrosphere (a nearby body of water such as a lake, river or sea) or the atmosphere. In figure 1.1 the heat is rejected to the atmosphere by a wet-cooled (evaporative) system, in which case the heat sink temperature is determined by the wet bulb temperature of the air. The temperature difference between the steam and the cooling water drives the heat transfer within the condenser.

Condensate leaving the condenser usually passes through a deaerator to remove oxygen and other dissolved gases, which may cause corrosion of the boiler and associated pipework. Thereafter it is pumped back to the boiler to complete the cycle.

This super-heated Rankine cycle is plotted on the temperature-entropy diagram in figure 1.2 (a), where it is assumed that the compression and expansion processes are isentropic. The effective power produced by the cycle is equal to the area enclosed by the curve joining points 1 to 4 figure 1.2. Modifications to increase this area and hence the net power can include reheating, as shown by the lines joining points 1-2-4-5-6.

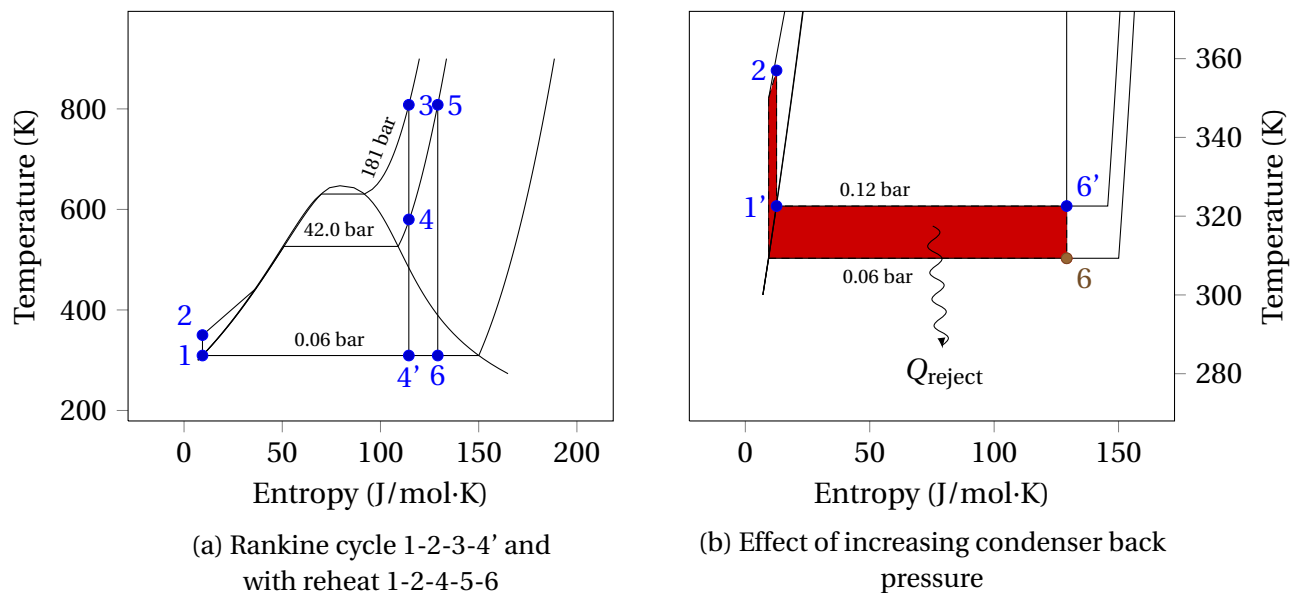


Figure 1.2: Temperature-entropy diagrams (isentropic expansion and compression)

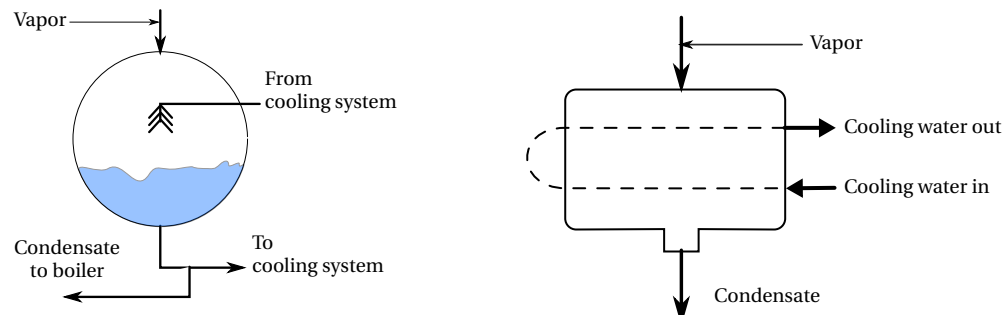
The change in effective power caused by an increase in condenser back-pressure is illustrated in figure 1.2 (b). If the condenser performance deteriorates from its design point as a result of fouling or air-ingress, the steam is then condensed at a higher temperature ($T_{6'}$) and back-pressure. The shaded area represents the additional heat that is rejected to the environment. The net power generated by the cycle decreases

CHAPTER 1. INTRODUCTION

by this amount. Since the condenser determines the temperature at which the steam condenses, its performance has a major impact on the net amount of power generated by the cycle.

1.2 Direct versus indirect condensers

Condensers may either be a direct-contact type or indirect-surface type. The differentiation refers to whether the working fluid and cooling fluid directly contact one another. An example of the direct-contact type of condenser is the direct contact spray condenser, as shown in figure 1.3 (a). Re-cooled water enters the condenser via spray nozzles, which causes the steam to condense directly on the water droplets. A portion of the condensate is sent to the boiler, whilst the rest returns to the cooling system.



(a) Direct type: direct contact spray condenser (b) Indirect type: shell and tube condenser

Figure 1.3: Examples of direct and indirect condensers

Conversely, the indirect type causes condensation of the steam onto a surface which separates the steam and the cooling fluid. The archetypal shell and tube condenser shown in figure 1.3 (b) has cooling water passing through the inside of the condenser tubes. The steam enters the shell space, condenses on the outside of these tubes and falls under the action of gravity. These condensers, also referred to as vacuum steam surface condensers, shall be the sole focus hereafter.

Different shell and tube configurations are necessary depending on the operating requirements and cooling system used. For example, cooling water from rivers, lakes or seas is generally used in single pass condensers to meet environmental requirements, which limit the temperature rise of surface water.

CHAPTER 1. INTRODUCTION

1.3 Description and operation of a vacuum steam surface condenser

A divided, single compartment steam surface condenser with two tube passes is represented in figure 1.4. Re-cooled water enters the waterbox before passing through the right half of the tube bundle. The return waterbox ducts the water to the other half of the tube bundle to complete the second pass. Finally the cooling water exits out the waterbox on the left. Turbine exhaust steam enters the top of the condenser from the turbine neck and flows downward through passages between the tubes. These passages, or steam lanes, are designed to: minimize pressure drop of the steam, mitigate excessively high vapor velocities, and prevent excessive condensate inundation. As latent heat is removed from the vapor, it condenses and falls into the hot-well region under gravity. Air and other non-condensable gases are extracted in the air extraction zone, which is typically positioned in the region of lowest pressure, where the non-condensable gases tend to accumulate.

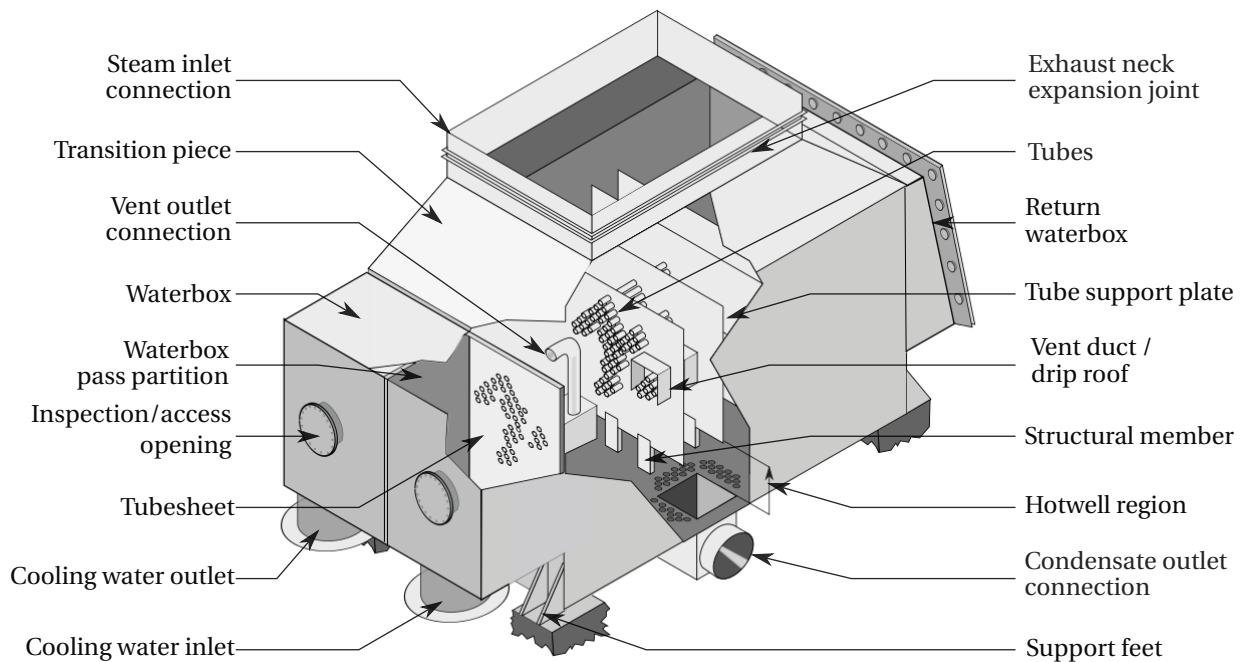


Figure 1.4: Simplified schematic of a two pass, single compartment steam surface condenser

Fundamentally the air extraction is achieved by venting the steam space of the shell, using either steam-jet-air-ejectors or liquid ring vacuum pumps. As shown in figure 1.4 a drip roof is used to form a duct to extract the non-condensibles. It also serves to minimize the amount of entrained water being extracted along with the

CHAPTER 1. INTRODUCTION

non-condensable gases.

Since the condenser is a critical component in the cycle, any significant tube leaks result in forced downtime of the plant. Leaks occur as a result of through-wall perforations or tube-to-tubesheet joint leaks, and cause low-grade cooling water to enter the steam space and contaminate the high-grade condensate. Not only does this increase the corrosivity of the boiler feed water, it can also lead to impingement damage on the turbine blades. The situation is exacerbated by the fact that the condenser operates under vacuum; consequently a relatively small pin hole results in copious amounts of cooling water leaking into the steam space.

Remedial action starts by reducing power output. If a the condenser has a multi-compartment shell, the turbine is operated under partial load. This allows for draining of the affected compartment of the condenser to allow access into the water box. The leak must then be identified, which in itself is a onerous task as typical tube bundles can consist of tubes in excess of 10 000 tubes. The damaged tube is then isolated from service by installing sealing plugs at both of its ends. A high-level water test performed after this ensures that the installed plugs effectively seal the damaged tube.

Putman (2001) characterizes condenser tubes used in steam surface condensers into three main groups: copper-based alloys, stainless steels, and titanium. Selection criteria are based on the operating conditions of the condenser, for example whether the cooling fluid is fresh water or sea water.

Copper-based tubes have been extensively used throughout condenser history. Their relatively high thermal conductivity has contributed to this. Certain alloying elements such as tin and arsenic have been added to increase the copper alloy's resistance to corrosion, particularly in sea water applications.

Stainless steels have a relatively lower thermal conductivity although a generally higher corrosion resistance. For this reason they are often used in air extraction zones and in peripheral areas of tube bundles.

Titanium has the greatest corrosion resistance, but it suffers from stress cracking. As a result the handling and installation of such tubes requires great care. Harmonics must also be considered when replacing existing copper-based alloy tubes with titanium. The relatively low thermal conductivity is countered by the reduced wall thickness, which is achievable by exploiting the good strength properties of titanium.

1.4 Degradation mechanisms affecting condenser tubes

Three important factors affecting thermal and structural performance of condenser tubes are fouling, erosion, and corrosion. Fouling can have a significant impact on the heat rejected by the condenser by forming an additional resistance to heat trans-

CHAPTER 1. INTRODUCTION

fer and flow resistance. Ultimately this results in high turbine back pressure and reduced plant efficiency.

Erosion is caused by high levels of turbidity (a measure of suspended solids) and high velocities. The additional turbulence at the inlet and outlets of the tubes accelerates the erosion mechanism, which is referred to as inlet-outlet erosion.

General corrosion acts on the entire tube and causes material loss along the length of the tube. However, there exist accelerated forms of corrosion which preferentially attack concentrated areas. This rapidly leads to tube leaks and hence premature failure well before their expected lifespan. As already explained, this has critical ramifications because any tube leaks result in contamination of the boiler feed water. The fouling, erosion and corrosion mechanisms are considered in further detail below.

1.4.1 Fouling of condenser tubes

Fouling may be categorized into two main types: macro fouling and micro fouling. According to Tsou (2002), micro fouling may refer to: corrosion, scaling, particulate fouling, and biological fouling. Macro fouling encompasses the restriction of flow through the tubes, by foreign materials such as organic matter and inorganic debris (that cover the tube sheet or become lodged in the tubes). For the purposes of this study only micro fouling will be considered and will be referred to as fouling hereafter.

Scaling and particulate fouling generally increase with time and predominately come about since the solubility of certain ions present in the cooling water decreases with temperature. Two important ions that exhibit this behavior are calcium and magnesium, which form calcium carbonate and magnesium carbonate respectively. Dobersek & Goricanec (2007) studied the linings of such scales on the surfaces of plate and pipe heat exchangers in domestic appliances, and they concluded a significant effect on heat transfer. This results from the relatively low thermal conductivity of calcium carbonate, which has a value in the range of 2 to 3 W/m·K, depending on its porosity. Furthermore, compounding deposition of this scale restricts the cross-sectional flow area of the condenser tubes.

The reduction in cross-sectional area causes an increase in the frictional pressure drop along the tube. This increase in the hydrodynamic system resistance reduces the velocity of the water in the tubes. As a result the internal convection heat transfer coefficient decreases, as it is a function of the water velocity. Hence the resistance to heat transfer is further increased, as the conduction and convection resistances increase.

The increased resistance to heat transfer reduces the performance of the condenser. Therefore, the temperature difference between the steam and cooling system must increase for the same heat duty. Consequently the back pressure rises and the effective power output decreases (see figure 1.2 b). The decreased thermal effi-

CHAPTER 1. INTRODUCTION

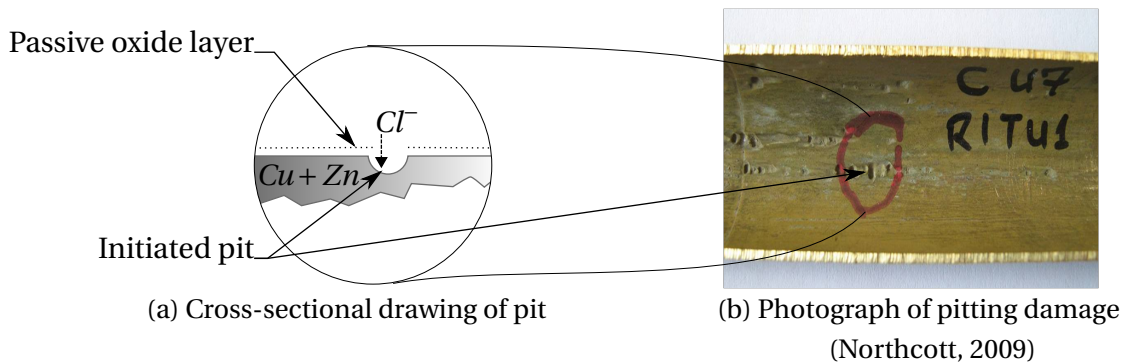


Figure 1.5: Example of pitting corrosion in condenser tubes

ciency means that more fuel needs to be consumed in order to meet power output requirements stipulated by demand from the power grid. In the case of wet cooled systems, this also increases the water consumption. Financially this increases the plant running costs, and hence life cycle costs; it also increases the emissions produced. Additionally this fouling may give rise to degradation of the tubes through corrosion mechanisms. Thus there is an increase in the risk of tube leaks (and hence boiler feed water contamination), ultimately decreasing the station life.

1.4.2 Corrosion and erosion mechanisms

Degradation of the tubes may result from either corrosion-related issues (such as pitting, surface corrosion and/or galvanic corrosion), erosion mechanisms (for example inlet erosion) or a combination thereof. Fouling deposits can give rise to crevice corrosion and erosion-corrosion due to localized flow eddies.

Pitting corrosion usually occurs in condenser tubes which rely on the formation of a passive oxide layer for their corrosion resistance. Such tubes include those made from brass and stainless steel; these constitute approximately 70% of the condenser tubes in South African plants. As shown in figure 1.5, chloride ions present in the cooling water penetrate the oxide layer. Once a pit is initiated, local conditions within the pit worsen because of the reduced flow in this area. Specifically the pH and concentration of chloride ions worsen, and this results in accelerated corrosion within the pit. This condition is autocatalytic as the process stimulates itself once initiated. These highly localized corrosion areas worsen until the remaining material fails.

Dezincification of the brass tubes results when the chloride ions react strongly with the zinc present in the brass alloy. This selective attack of the zinc occurs because the zinc reacts more readily with chloride containing water than copper does. Zinc chloride is produced, leaving a porous copper matrix behind in the parent material. This weakened matrix is left vulnerable to mechanical failures. This has been

CHAPTER 1. INTRODUCTION

a major concern and has led to numerous tube failures which result in down-time of the equipment as well as steam contamination.

A large level of ions in the cooling water has also resulted in relatively thick layers of scale build-up; for example a scale thickness in excess of 1.2 mm was measured on a tube extracted from a power station in June 2012. Operating conditions such as these have arisen from poor quality cooling water, insufficient cleaning maintenance as well as inadequate shut-down-time allocation.

1.4.3 Cooling water quality

Cooling water systems of the open recirculation type, such as those using wet cooling towers, suffer from cycles of high concentration. High concentrations of ions are formed when a portion of the cooling water evaporates as it passes through the cooling tower. To combat this situation blowdown procedures are employed which periodically exchange the cooling water with fresh water.

To mitigate corrosion, the preferred method of operation suggested by McEwan (2004) is to maintain an alkaline cooling water and prevent scale using antiscalant dispersants such as polyacrylates, polymaleics, polyolylesters, and phosphorates. However, cooling water analyses have shown that some condensers have been subjected to out of specification cooling water.

A water analysis of the cooling water on a particular power station in South Africa, performed by Northcott (2009), showed a turbidity exceeding the original design specified limit by over a 100%. Physically this level of turbidity is so high that it means that suspended particles are visible to the naked eye. Particles such as these can cause excessive abrasion and thus wall thinning of the condenser tubes. The same analysis revealed that the tested water had excessive chloride ions present (approximately 28% over the allowable limit).

Water treatment plants are overburdened because of dramatically lower quality water sources. Growing power demands of the country as well as delayed new plant installations have increased pressure placed on plant equipment. Practically this has caused fewer maintenance shut-downs for the water treatment plants. Also, upgrades have not been made to existing plants in order to cope with these matters. Additional stresses placed on the equipment increase their chance of failure.

1.5 Combating degradation of condenser tubes

1.5.1 Mitigation techniques

Principal methods to combat degrading condenser tubes include refurbishment of the existing tubes or replacing the tubes. Refurbishment methods include artificial

CHAPTER 1. INTRODUCTION

protective coatings and liners.

Application of artificial coatings must begin with appropriate preparation of the tube surface before coating. The preparation methods depend on the condition of the tubes and should be decided upon based on case-specific criteria. Scale deposits and other contaminants can be removed using high pressure water lancing, abrasive grit blasting, and or chemical cleaning.

Full-length tube liners have been used in the past although tests cited by Putman (2001) show how detrimental they can be on performance when installed incorrectly. Apparently penalties as high as 30% of the single tube overall heat transfer coefficient result from the use of liners. One reason for this is that undulations in the tube profile cause an air gap between the tube and the liner.

Tube replacement incurs a significant cost, not only due to the loss of production, but also due to the large material and labor costs. The retubing operation involves large volume handling, which is of the order of 200 tonnes. The time taken to accomplish this can be up to three months, and the unit cannot produce any electricity during this period. In instances where the existing tubes have become irreparably damaged, retubing remains the only solution.

1.5.2 The need for condenser refurbishment

The paradigmatic need for condenser refurbishment can be seen as a global issue. However, in the domestic context, the issue is worsened by the fact that South Africa has a growing electricity demand which exceeds its supply. Inglesi & Pouris (2013) state that the country experienced a 50% increase in demand between 1994 and 2007. The authors propose two possible reasons for this: firstly, the implementation of the Free Basic Electricity Policy in 2001, and secondly, economic growth (resulting from the lifting of sanctions). Between 2000 and 2010 the United States Energy Information Administration (2013) estimate a 20% increase in demand in South Africa. However, these estimates show only a 7% increase in installed capacity from 2000 to 2010. This inundation of power demand led to a electricity crisis between 2007 and 2008 resulting in rolling blackouts.

The state utility Eskom plans to commission two new coal-fired power plants, named Medupi (4 788 MW) and Kusile (4 800 MW). However, financial difficulties as well as labour protests have repeatedly delayed the completion of these stations. The six units of Medupi were scheduled to be commissioned at nine-month intervals, with the first unit being commissioned in 2012. As a short-term expansion plan Eskom recommissioned Camden (1 430 MW), Grootvlei (950 MW) and Komati (284 MW) power stations.

The power shortage has forced stations to operate over their original design life-spans. This operation is possible by implementing extension strategies which re-

CHAPTER 1. INTRODUCTION

refurbish current power plant hardware. Therefore the refurbishment of condensers becomes a critical factor in meeting the energy demands of the country.

Condenser refurbishment is case specific, although economic and time constraints often dominate the decision making. Simply retubing the condenser is not always possible. Tubes are imported and the lead time from the date of ordering can take up to two years.

As an interim measure full-length artificial protective coatings have been used. Fraze & Woodruff (1997) investigated condenser tube coating as an alternative to retubing. Their study concluded that condenser tube coating can effectively extend a seawater service condenser's lifespan up to five years. Hence artificial protective coatings as a short-term (5 to 10 years) alternative to retubing was employed in South African power plants from 2004. To date approximately 800 000 tubes have been coated locally.

1.6 Artificial protective coatings applied to condenser tubes

A possible solution to comprehensively address the issue of fouling and degradation of condenser tubes is to coat the internal surface of the tubes with an artificial protective coating (APC). As depicted in figure 1.6, the coating acts as a layer of protection against corrosion and erosion. The micro-graph shows the coating applied to a new tube, and indicates how thinly these coatings can be applied. This is a crucial factor when evaluating the performance of different coatings.

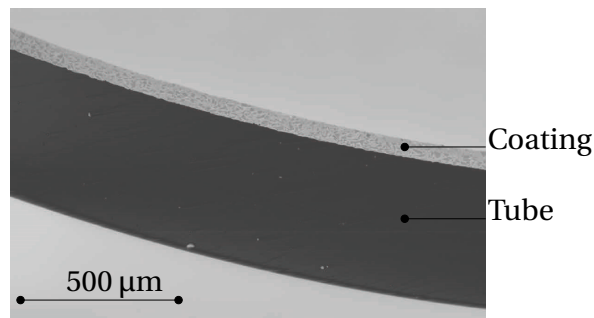


Figure 1.6: Micro-graph of a cross-sectioned coated tube (Northcott, 2009)

Figure 1.7 shows how certain coatings techniques tend to fill pits in the tube wall, creating a smoother surface. Effectively this retards the accelerated corrosion process causing the pitting. Moreover, the number of nucleation sites for fouling are reduced and the flow velocity may also increase. Ultimately this has the potential to

CHAPTER 1. INTRODUCTION

significantly reduce the fouling rate. Sato, Nosetani & Hotta (1985) concluded from field tests that APCs are an effective countermeasure against corrosion and fouling.

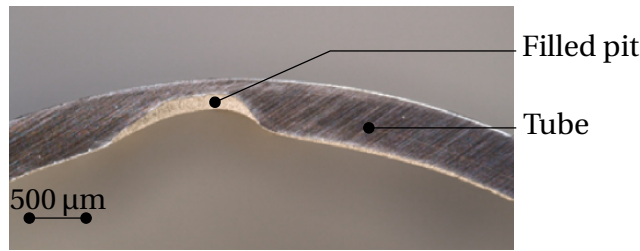


Figure 1.7: Micro-graph showing preferential filling of pit by coating (Sieberts, 2011)

However, this coating also increases the conduction resistance to heat transfer. The thermal performance impact of coating the internal surface of condenser tubes depends most importantly on the thermal conductivity of the coating, and the coating thickness. The relative contribution from the inner and outer convection heat transfer resistances also needs to be taken into account in order to determine the relative impact on the overall heat transfer coefficient. Often the conduction resistance is several orders of magnitude smaller than the dominant convection resistances.

Although from a thermal performance viewpoint, the coating thickness should be minimized, there are two factors which limit the coating thickness. The first is the corrosion resistance, which increases with coating thickness. Obviously depending on the quality of the cooling water, the required corrosion resistance will limit the minimum thickness of the coating which will offer sufficient corrosion resistance. The second physical factor limiting the thickness is imposed by the application process, which depends on the type of coating to be used. At very low thicknesses, less than about 25 μm, the coating film tends to be discontinuous; this leaves areas of the tube surface exposed and compromises the efficacy of the coating.

Studies performed by Frazee & Woodruff (1997) have shown that some condenser tube coatings had no negative effect on the operating heat transfer rate. This is presumably because the thermal conductivity of the coated tube (after removal of the fouling layer) was comparable to the conductivity of the fouled tube. Furthermore it was discovered that the coated tubes had better heat transfer performance after three years of service than typical “cleaned” tubes in the unit. The reason suggested by them for this better heat transfer was that the coated tubes did not foul as quickly as the uncoated tubes.

Consider the following local case study of a particular power station. As part of a restoration project in 2009, a condenser was refurbished by applying an APC. The condenser is a single shell, two pass, single pressure, divided compartment type as depicted in figure 1.8. Each pass contains approximately 6500 tubes so that each compartment has 13000 tubes.

CHAPTER 1. INTRODUCTION

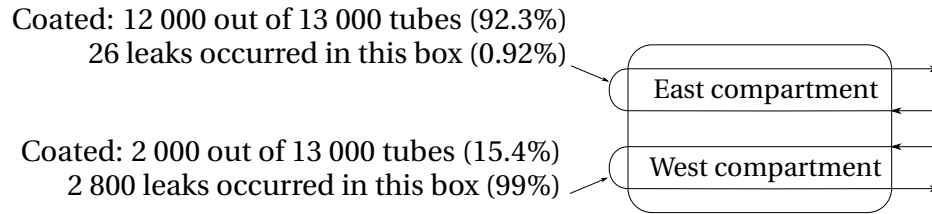


Figure 1.8: Schematic of the condenser in a case study

Although the station planned to retube the condenser in the future, an APC was chosen to delay the retubing operation. It was decided that eddy current testing would be used to identify the tubes that had the greatest general wall loss. The station planned to use these results to only coat the worst effected tubes. Due to time constraints only 53% of the whole condenser was coated.

Approximately 12000 of the 13000 tubes were coated in the east compartment (see figure 1.8). The other compartment had only 2500 tubes coated. Hence 92% of the east compartment was coated and only 15.4% of the west compartment was coated.

During operation from 2009 to 2013, roughly 2826 tube leaks occurred. Of these leaks, 2800 occurred in the west compartment (15.4% of which was coated), and only 26 leaks occurred in the east compartment that had 92% of its tubes coated.

In spite of slightly different operating temperatures between the two compartments, 99% of the tube leaks occurred in the compartment which only had 19% of its tubes coated. This fact provides strong evidence to support the notion that artificial protective coatings can be used to extend condenser tube life-spans.

1.7 Motivation for this study

Considering the tube failures resulting from general wall thinning, poor cooling water quality, dezincification and insufficient maintenance shut-downs, it was decided in 2004 to use full length APCs as a short-term (5 to 10 year) strategy to extend condenser operating life-spans.

The research question associated with these coatings is, "what will their affect on the overall condenser performance be?" Although other studies had been performed overseas, they were not specific to the coatings being manufactured and applied domestically. Specifically the thermal conductivities of the coatings being used were unavailable from the suppliers. Also, the application techniques developed in South Africa differ from those used worldwide. Furthermore, heat transfer research is crit-

CHAPTER 1. INTRODUCTION

ical in developing enhanced performance coatings for this specific purpose. Experimental studies are therefore essential.

Such testing would need to evaluate the coated thermal performance of the condenser tube as well as its hydraulic resistance. The performance evaluation has to be completed at similar operating conditions to those experienced in service. In this way single-tube test results can offer insight into the overall condenser behavior as a result of coatings. As will be discussed later, the only exception to this is that water is used on the outer surface of the tube instead of steam. The reason for this is to achieve higher repeatability of the outer convection heat transfer coefficient.

1.8 Objectives

The objectives of this testing are to:

1. evaluate the thermal performance of three condenser tube coatings applied to single brass tubes, which are developed and applied in South Africa;
2. measure the static pressure drop along the internal surface of these coated tubes;
3. predict the overall performance impact on the condenser as a result of these coatings; and
4. determine a practical method to formulate selection criteria for APCs.

1.9 Thesis outline

This document consists of a main body composed of six chapters, and an appendix with five sections. Each of these chapters is summarized below:

Chapter 1 – Introduction The fundamental principles of the Rankine power cycle are described, and the role of the steam condenser in this cycle is indicated. A description of a vacuum steam surface condenser is provided together with the operational aspects. Condenser tubes are then discussed, particularly focusing on degradation mechanisms as well as mitigation techniques. Details pertaining to artificial protective coatings and their role in combating degradation mechanisms are covered. The chapter concludes with the motivation and objectives of this investigation.

CHAPTER 1. INTRODUCTION

Chapter 2 – Applicable theory The log mean temperature method of analysis presented in this chapter is used to analyze a double-pipe counter-flow heat exchanger. Convection correlations in the literature are summarized, together with the published thermal conductivities of relevant condenser tubes. The thermal resistances are then quantified, and these equations are tailored to the analysis of coated tubes. This chapter underpins analysis of the experimental data in chapter 4 as well as the model condenser in chapter 5.

Chapter 3 – Experimental facility Details of the test facility that was designed, built and commissioned for this investigation, are followed by a description of the methodology and test procedures. The relevant calibration procedures are also reported.

Chapter 4 – Experimental testing Using the apparatus and method described in chapter 3, the experimental results are presented. These include the isothermal tests and energy balance checks necessary to validate the experimental results.

Chapter 5 – Coated condenser performance modeling Using data from the Heat Exchange Institute (2012) standard, a mathematical model is developed and used to investigate the relative effect of coating on the overall performance of the condenser. The sensitivities to coating thickness and thermal conductivity are explored. Thereafter the implications of the results with respect to actual service tubes are discussed.

Chapter 6 – Conclusion Conclusions concerning the thermal performance as well as the feasibility of condenser coatings are stated. Recommendations are also included which identify a warranted need to further investigate the coating resistance to fouling.

Appendices The appendices supplement this paper with relevant thermo-physical property data equations, experimental observations, and sample calculations. Calibration certificates are also appended.

Chapter 2

Applicable theory

Overview

In this chapter the necessary equations describing the heat transfer rate and pressure drop of a double-pipe counter-flow heat exchanger are presented. After extending the fundamental equations to analyze coated tubes, measurement data is used in chapter 3.1 to determine the thermal conductivity of different coatings. The basic theory presented here is used in chapter 5 to create a mathematical model of a steam surface condenser.

2.1 Introduction to heat exchanger analysis

A heat exchanger facilitates heat transfer between two fluids that are at different temperatures. Distinction is made between open type and closed type heat exchangers; the latter type separates the fluids by means of a solid wall. The analysis of such heat exchangers involves determining the overall heat transfer coefficient UA , which accounts for the total thermal resistance to heat transfer. This overall heat transfer coefficient is multiplied by a suitably chosen average temperature difference, resulting in the total heat transferred from the hot to the cold fluid.

The total rate of heat transfer is expressed in an analogous form to Newton's law of cooling as

$$Q_{tot} = UA\Delta T_m \quad (2.1)$$

where ΔT_m is a suitably chosen average temperature difference based on the inlet and outlet temperatures. The overall heat transfer coefficient is based on the outside surface area of the tube (A_o).

The simplest type of closed heat exchanger, namely a double-pipe (or tube-in-tube) heat exchanger, is analyzed first. In chapter 5 the analysis is extended to include

CHAPTER 2. APPLICABLE THEORY

steam surface condensers. Two¹ principle modes of heat transfer occur in these types of heat exchangers. The first mode of heat transfer is convection at the solid-fluid interface. The second mode is conduction through the tube wall. Evaluating the outer convection coefficient is the salient difference between the double-pipe heat exchanger and the condenser analyses.

Consider the double-pipe counter-flow heat exchanger presented in figure 2.1. To clearly distinguish between the two different fluids, they will be referred throughout this text as the cold stream and hot stream. The cold stream refers to the fluid flowing through the inner tube, whereas the hot stream is used to designate the annular fluid.

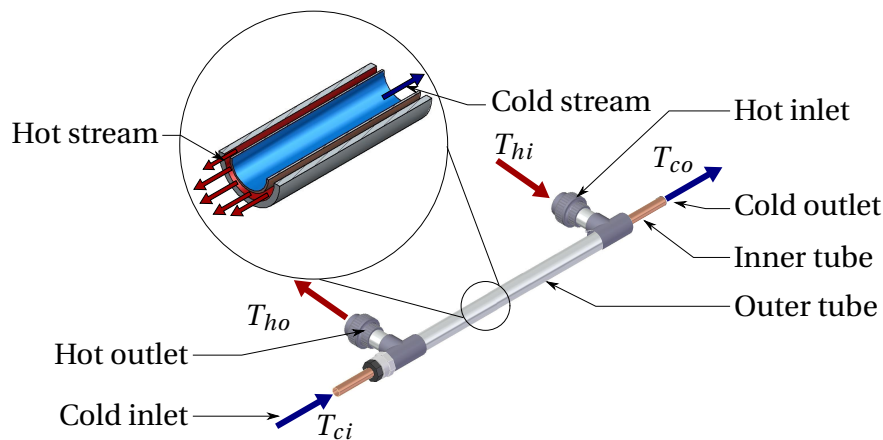


Figure 2.1: Double-pipe counter-flow heat exchanger

The cold fluid enters the inner tube at a temperature T_{ci} , and exits at a higher temperature T_{co} . Conversely the hot fluid enters the annular region at a temperature T_{hi} , and flows in a counter-current fashion to the cold stream. The hot fluid then exits at a lower temperature T_{ho} .

The temperature differences between the two fluids and hence the heat transfer, vary with axial length. Therefore, the temperature variation is plotted in figure 2.2 (a) against the normalized heat transfer. Q_{tot} is defined to be the total heat transfer for the heat exchanger. Q refers to the heat transfer calculated from the heat exchanger inlet up to a certain length along the heat exchanger.

Hypothetically a condenser represents a special case of heat exchanger, whereby the phase change results in the hot fluid condensing at constant temperature (figure 2.2 b). Two important temperature differences are also defined in figure 2.2 (b). These are the terminal temperature difference (TTD) and initial temperature differ-

¹In fact a third mode of heat transfer is radiation, although it is typically of negligible value in comparison to the principle modes of heat transfer already mentioned.

CHAPTER 2. APPLICABLE THEORY

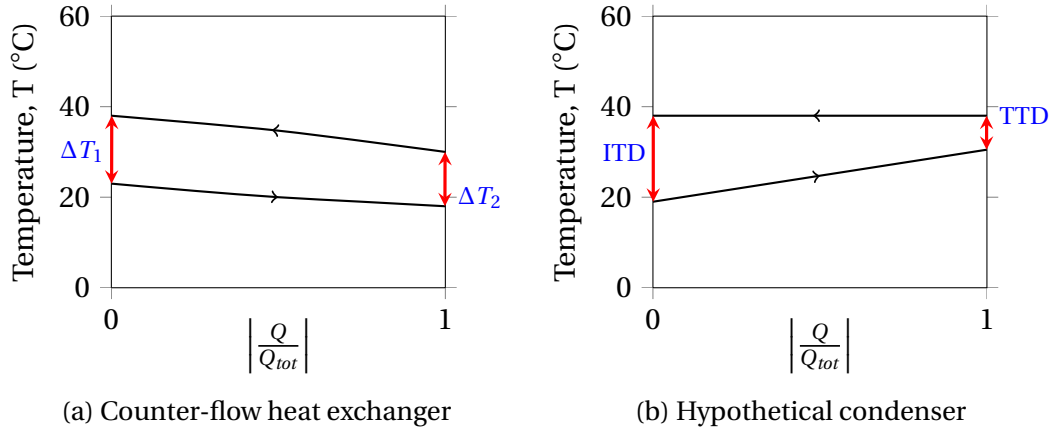


Figure 2.2: Temperature variation with heat transfer

ence (ITD). In reality, the steam temperature is not constant throughout the condenser. But considering the uncertainty inherent in estimating the steam-side convection (Heat Exchange Institute, 2012) it proves useful to proceed under the premise of an assumed constant steam temperature.

For both situations illustrated in figure 2.2 it can be shown that the appropriate temperature difference used to determine the overall heat transfer rate is logarithmic (Cengel & Ghajar, 2011). This log mean temperature difference (ΔT_{lm}) is defined as

$$\Delta T_{lm} = \frac{(T_{hi} - T_{co}) - (T_{ho} - T_{ci})}{\ln\left(\frac{T_{hi} - T_{co}}{T_{ho} - T_{ci}}\right)} \quad (2.2)$$

The overall rate of heat transfer may also be determined by applying the first law of thermodynamics to each fluid stream. By assuming constant specific heats, the heat transfer rate from the hot fluid is

$$\begin{aligned} Q_h &= m_h c_{p,h} (T_{hi} - T_{ho}) \\ &= m_h c_{p,h} \Delta T_h \end{aligned} \quad (2.3)$$

and similarly the heat transfer rate to the cold stream is

$$\begin{aligned} Q_c &= m_c c_{p,c} (T_{co} - T_{ci}) \\ &= m_c c_{p,c} \Delta T_c \end{aligned} \quad (2.4)$$

Substituting equation (2.2) into equation (2.1) and rearranging yields

$$UA = \frac{Q_{tot} \ln\left(\frac{T_{hi} - T_{co}}{T_{ho} - T_{ci}}\right)}{(T_{hi} - T_{co}) - (T_{ho} - T_{ci})} \quad (2.5)$$

CHAPTER 2. APPLICABLE THEORY

2.2 Electrical resistance analogy and the overall heat transfer coefficient

To evaluate the overall heat transfer coefficient, an electrical resistance analogy is used (Cengel & Ghajar, 2011). This analogy exploits the similarity of the functional relationships between electric current and heat transfer. The electromagnetic force (EMF) or potential difference in electrical circuits is what causes current to pass through a resistor. Similarly a temperature difference causes heat to flow through a medium. The situation is sketched in figure 2.3.

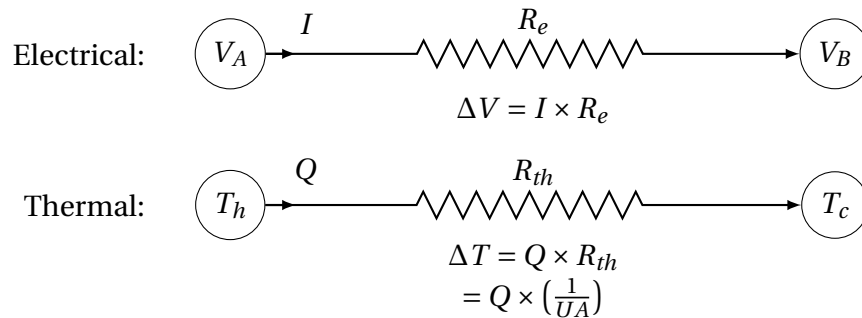


Figure 2.3: Analogy between thermal and electrical resistances

Comparing the equalities in figure 2.3, the total thermal resistance is equal to

$$R_{tot} = \frac{1}{UA} \quad (2.6)$$

The heat exchanger is considered to be well insulated so that heat transfer to the surroundings is negligibly small. Steady state conditions are presumed and changes in kinetic and potential energy are neglected. A one-dimensional model is developed, which only considers radial conduction and omits axial conduction.

Consider the path for heat transfer in the cross-sectional view in figure 2.4. Two modes of heat transfer occur. The first mode involves convection from the annular fluid to the inner tube wall. The thermal resistance representing this mode of heat transfer is denoted R_{h_o} . Incropera, Dewitt, Bergman & Lavine (2007) show that the thermal resistance to convection heat transfer is equal to

$$R_{h,ann} = \frac{1}{h_{ann}A_{ann}} \quad (2.7)$$

where h_o is the annular convection coefficient and A_o is the outer surface area of the

CHAPTER 2. APPLICABLE THEORY

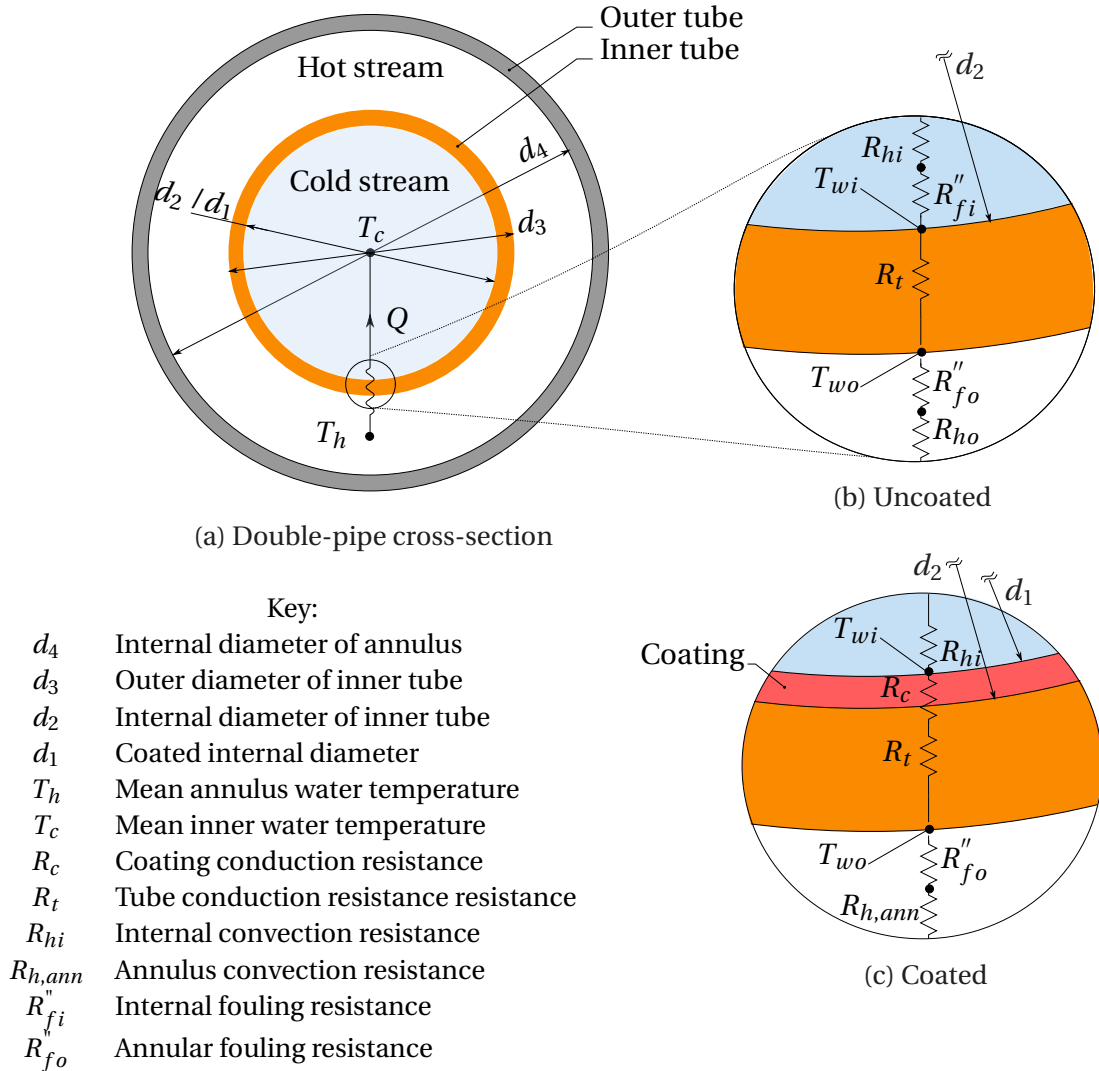


Figure 2.4: Cross-section of double-pipe heat exchanger showing resistance analogy for heat transfer

inner tube. Similarly for the internal convection

$$R_{hi} = \frac{1}{h_i A_i} \quad (2.8)$$

The second mode of heat transfer is radial conduction through the tube wall. The resistance R_t caused by the tube wall is calculated according to Incropera, Dewitt,

CHAPTER 2. APPLICABLE THEORY

Bergman & Lavine (2007) as

$$R_t = \frac{\ln \frac{d_3}{d_2}}{2\pi k_t L_{eff}} \quad (2.9)$$

where L_{eff} is the effective heat transfer length and k_t is the thermal conductivity of the tube in W/m·K. The variable d_1 is reserved to represent the coated internal diameter, which will be introduced later. Conduction resistances are also offered by the fouling layers on the outer and inner surfaces. The descriptors R''_{fo} and R''_{fi} represent the fouling factors of the outer and inner surfaces respectively. Hence the total thermal resistance to heat transfer becomes

$$R_{tot} = \frac{1}{h_{ann} A_{ann}} + \frac{R''_{fo}}{A_{ann}} + \frac{\ln \frac{d_3}{d_2}}{2\pi k_t L_{eff}} + \frac{R''_{fi}}{A_i} + \frac{1}{h_i A_i} \quad (2.10)$$

The convection coefficients in equation (2.10) are governed by the fluid motion. In the case of turbulent flow, no closed form solution is available. Thus these coefficients are evaluated using empirical correlations, many of which are a function of the friction factor and Reynolds number.

2.3 Determining the developed turbulent friction factor

The friction factor describes the velocity boundary layer at the surface at which the convection heat transfer is taking place. Solution of the velocity profile is necessary before the friction factor can be evaluated. This classical boundary layer analysis of internal flows is adopted from White (2005), Kröger (1998) and Munson, Young & Okiishi (2006).

The velocity boundary layer arises from the interaction between the fluid and the solid wall interface. The criterion of the no-slip condition means that the fluid velocity must be zero at this interface. By virtue of the viscous forces experienced by the fluid particles, a momentum change occurs as the fluid velocity increases from zero at the wall to a maximum at the free stream velocity. Consider the average velocity profile at a particular cross-section along the tube. The gradient of this curve, evaluated at the wall, is proportional to the shear stress applied to the wall, τ_{wall} . Considering Newtonian fluids, the constant of proportionality is termed the dynamic viscosity, μ . Although termed constant, this fluid property exhibits a temperature dependence, which is accounted for later. The velocity profile, and hence the shear stress at the wall, is dependent on the flow regime, whether it is either laminar, transitional, or turbulent.

CHAPTER 2. APPLICABLE THEORY

The flow regime is characterized according to the value of the Reynolds number. This dimensionless group is defined in terms of the hydraulic diameter d_e , as

$$Re_d = \frac{\rho v d_e}{\mu} \quad (2.11)$$

where $d_e = \frac{4 \times \text{wetted perimeter}}{\text{cross-sectional area}}$. For the inner tube the hydraulic diameter reduces to the internal diameter, i.e. d_1 (see figure 2.4). However, the hydraulic diameter for the annulus is equal to the difference in diameters between the outer jacket and the inner tube, i.e. $d_4 - d_3$. Fully turbulent flow is said to exist if the Reynolds number is greater than 4000 (Kröger, 1998). Having characterized the flow as fully turbulent, and hence determining the velocity profile, the shear stress at the wall can be determined.

The shear stress caused by the wall results in a pressure drop over a length of tube, $l_{\Delta p}$. Weisbach (1855), cited by Kröger (1998), showed that

$$\begin{aligned} \Delta p &= 4 \tau_w \left(\frac{L_{\Delta p}}{d} \right) \\ &= f_D \left(\frac{L_{\Delta p}}{d} \right) \left(\frac{\rho v^2}{2} \right) \end{aligned} \quad (2.12)$$

where f_D is termed the Darcy-Weisbach friction factor.

For smooth tubes Konakov, cited by Gnielinski (2009), calculated this friction factor as

$$f_D = (1.8 \log_{10} Re - 1.5)^{-2} \quad (2.13)$$

Generally the turbulent friction factor depends on the Reynolds number and relative surface roughness of the tube. For small relative surface roughnesses, Haaland (1983), cited by Kröger (1998), proposed

$$f_D = 2.7778 \left\{ \log_{10} \left[\left(\frac{7.7}{Re} \right)^3 + \left(\frac{\phi/d_1}{3.75} \right)^{3.33} \right] \right\}^{-2} \quad (2.14)$$

where ϕ is the surface roughness

The rate of convective heat transfer is dependent on the boundary layer. The boundary layer is in turn described by the friction factor. Empirical correlations used to estimate the convective heat transfer coefficient are often written in terms of this friction factor, as will be seen next.

2.4 Convection correlations

Empirical correlations are expressed in terms of the dimensionless Nusselt number, defined as

$$Nu = \frac{h d_e}{k_f} \quad (2.15)$$

CHAPTER 2. APPLICABLE THEORY

where h is the average convection coefficient, k_f is the thermal conductivity of the fluid, and the hydraulic diameter d_e is as defined above.

2.4.1 Smooth tube correlations

A well known correlation proposed by Dittus and Boelter, cited by Kröger (1998) and Incropera, Dewitt, Bergman & Lavine (2007), has the following forms:

$$Nu = 0.0265Re^{4/5}Pr^{0.3} \quad (\text{cooling}) \quad (2.16)$$

$$Nu = 0.0243Re^{4/5}Pr^{0.4} \quad (\text{heating}) \quad (2.17)$$

Rabas & Cane (1983) specifically considered heating water inside a tube with fully developed flow, and found the Nusselt number to be

$$Nu = 0.015Re^{0.835}Pr^{0.462} \quad (\text{heating}) \quad (2.18)$$

Petukhov & Krillov (1958), cited by Gnielinski (2009), developed an equation for fully developed flow

$$Nu = \frac{\left(\frac{f_d}{8}\right) RePr}{k_1 + 12.7\left(\frac{f_d}{8}\right)^{0.5} (Pr^{2/3} - 1)} \quad (2.19)$$

where

$$k_1 = 1.07 + \frac{900}{Re} - \frac{0.63}{1 + 10Pr} \quad (2.20)$$

which is applicable for the following ranges:

$$\begin{aligned} 2300 &< Re < 10^6 \\ 0.5 &< Pr < 10^4 \\ 0 &< \frac{d}{L} < 1 \end{aligned}$$

In the work conducted by Gnielinski (2009), it was discovered that reducing the above factor to

$$k_1 = 1 \quad (2.21)$$

produced the best correlation for the data in the fully developed region. The final form of the correlation is

$$Nu = \frac{\left(\frac{f_D}{8}\right) RePr}{1 + 12.7\left(\frac{f_D}{8}\right)^{0.5} (Pr^{2/3} - 1)} \quad (2.22)$$

Kröger (1998) used the following modification for developing flow:

$$Nu = \frac{\left(\frac{f_D}{8}\right) (Re - 1000) Pr \left[1 + \left(\frac{d}{L}\right)^{0.67}\right]}{1 + 12.7\left(\frac{f_D}{8}\right)^{0.5} (Pr^{2/3} - 1)} \quad (2.23)$$

CHAPTER 2. APPLICABLE THEORY

2.4.2 Annular flow correlations

Prandtl (1944), cited by Gnielinski (2009), proposed a semi-empirical equation for fully developed annular convection of the form

$$Nu_{ann} = \frac{\left(\frac{f_D}{8}\right) Re Pr}{1 + 8.7 \left(\frac{f_D}{8}\right)^{0.5} (Pr^n - 1)} \quad (2.24)$$

Dirker & Meyer (2005) have shown that the annular convection coefficient depends on the diameter ratio of the annulus, defined as

$$a = \frac{d_4}{d_3} \quad (2.25)$$

Due to the different velocity profile within the annulus, the annular friction factor $f_{D,ann}$, depends on this ratio. Gnielinski (2009) showed that this annular friction factor can be determined from

$$f_{D,ann} = (1.8 \log_{10} Re^* - 1.5)^{-2} \quad (2.26)$$

where

$$Re^* = Re \frac{(1 + a^2) \ln a + (1 - a^2)}{(1 - a)^2 \ln a} \quad (2.27)$$

Taking this into consideration, Gnielinski (2009) proposed the following correlation for annular convective heat transfer (outer tube insulated):

$$Nu_{ann} = \frac{\left(\frac{f_{D,ann}}{8}\right) Re_h Pr_h}{k_1 + 12.7 \left(\frac{f_{D,ann}}{8}\right)^{0.5} (Pr_h^{2/3} - 1)} \left[1 + \left(\frac{d_h}{L_{eff}}\right)^{2/3} \right] F_{ann} K \quad (2.28)$$

where,

$$k_1 = 1.07 + \frac{900}{Re_h} - \frac{0.63}{(1 + 10 Pr_h)} \quad (2.29)$$

With the annulus outer jacket insulated, and heat transfer only through the inner tube, Gnielinski (2009) suggests using the following factor in equation (2.28):

$$F_{ann} = 0.75 a^{-0.17} \quad (2.30)$$

CHAPTER 2. APPLICABLE THEORY

2.5 Evaluating the total thermal resistance

The total resistance for heat transfer of an uncoated tube is repeated for convenience

$$R_{tot} = \frac{1}{h_{ann}A_{ann}} + \frac{R''_{fo}}{A_{ann}} + \frac{\ln \frac{d_3}{d_2}}{2\pi k_t L_{eff}} + \frac{R''_{fi}}{A_i} + \frac{1}{h_i A_i} \quad (2.10)$$

Unless otherwise stated, it will be assumed that the inner and outer surfaces of the tube are clean, that is $R''_{fi}, R''_{fo} = 0$. Each of the remaining resistance terms are evaluated using the correlations presented previously.

The inner convection is based on the internal surface area which is calculated as

$$A_i = \pi d_2 L_{eff} \quad (2.31)$$

Using this area and the correlation given by equation (2.19), the inner convection term is

$$\frac{1}{h_i A_i} = \left[\pi L_{eff} k_{fc} \cdot \frac{\left(\frac{f_D}{8}\right) (Re_c) Pr_c}{1 + 12.7 \left(\frac{f_D}{8}\right)^{0.5} (Pr^{2/3} - 1)} \right]^{-1} \quad (2.32)$$

The outer convection term in equation 2.36 is based on the outer surface area of the tube, which means

$$A_o = \pi d_3 L_{eff} \quad (2.33)$$

The annular correlations presented previously are restricted to fully developed flow conditions within the annulus. Depending on the heat exchanger geometry, there may be significant edge effects. Obviously the edge effects are most significant for relatively short heat exchangers. Such effects are experimentally investigated later, when the measured outer convection coefficient will be compared to the fully developed correlations.

For the sake of generality, the outer convection term is expressed in terms of the outer Nusselt number. This generality also lends itself to the condenser analysis of chapter 5. The outer convection term is

$$\frac{1}{h_{ann} A_o} = [\pi L_{eff} k_{fh} \cdot Nu_o]^{-1} \quad (2.34)$$

The third term of equation (2.10) represents the conduction resistance offered by the tube wall. This depends on the thermal conductivity of the tube. Literature values for the relevant tube materials are shown in table 2.1. Although these tubes are manufactured according to standards which specify the allowable ranges of alloying elements, the thermal conductivities will still vary within a narrow range. This range

CHAPTER 2. APPLICABLE THEORY

Table 2.1: Thermal conductivities of condenser tubes

Name	ASTM code	Thermal conductivity		Reference
		W/m·K	k_t BTU·ft/(hr·ft ² ·°F)	
Admiralty brass	B 111	111, 111	64.0, 64.0	[1], [2]
Cartridge brass	n/a	120, 109–121	69.3, 63.0–69.9	[2], [3]
Stainless steel	A 249 TP 304	14.9	8.6	[1]
Titanium	B 338 GR2	22.0	12.7	[1]

[1]: Heat Exchange Institute (2012)

[2]: Davis (2001)

[3]: Goodfellow Cambridge Ltd. (2013)

will depend on the standard to which the supplier adheres to. For example, Goodfellow Cambridge Ltd. (2013) manufactures cartridge brass with a conductivity between 109 W/m·K and 121 W/m·K, which represents an approximate variance of 10%.

Substituting equations (2.32), (2.34) and (2.10) into (2.6) yields

$$\begin{aligned}
 UA_o = & \left[(\pi L_{eff} k_{fh} \cdot Nu_{ann})^{-1} + \frac{R''_{fo}}{A_o} + \frac{\ln \frac{d_3}{d_2}}{2\pi k_t L_{eff}} \right. \\
 & \left. + \frac{R''_{fi}}{A_i} + \left(\pi L_{eff} k_{fc} \cdot \frac{\left(\frac{f_D}{8}\right) (Re_c) Pr_c}{1 + 12.7 \left(\frac{f_D}{8}\right)^{0.5} (Pr^{2/3} - 1)} \right)^{-1} \right]^{-1} \quad (2.35)
 \end{aligned}$$

The aim of the preceding analysis is to set forth the necessary correlations needed to analyze a double-pipe counter-flow heat exchanger. Next the analysis is extended to enable quantifying the thermal performance of coated tubes.

2.6 Methods of analyzing coated tubes

The fundamental heat exchanger analysis may be extended to include the effects of coating the inside surface of the inner tube using three variant approaches. Consideration is first given to an overview of each method, which places them in context and clarifies their nuances. Thereafter each method is considered in detail.

2.6.1 Overview of three coated tube methods of analysis

The first method considers the tube to be composite, i.e. the coating is treated as a cylindrical wall in contact² with the tube wall. The internal convection coefficient is

²The contact resistance is considered zero because the coating has a near perfect inter-facial contact. De-lamination would be an exception, however all the coatings are thoroughly checked for this.

CHAPTER 2. APPLICABLE THEORY

determined according to the actual coated diameter. Coatings can be compared objectively in this manner, because their conductivity is an intensive material property.

The second method involves considering coating to be a layer of negligible thickness in relation to the tube. This means that the internal convection coefficient is based on the uncoated diameter. The error associated with using the uncoated diameter of the tube is then included in the determination of the represented factor of the coating, $R''_{f,c}$. Using this method, comparison of different coating factors is only possible assuming constant coating thicknesses.

Alternatively the third method assumes the tube and coating combination to be homogeneous, in which case the effective thermal conductivity of the coated tube combination k_{eff} is determined. As in the second method coating comparisons using this method rely on fixed thicknesses.

The suitability of the second and third methods depends on the coating thicknesses. Obviously the error introduced by neglecting the coated diameter becomes more significant for larger coating thicknesses. However, for design purposes merit can be found in their simplistic use.

2.6.2 Composite tube method of analysis

By considering the coated tube to be a composite tube, an additional conduction resistance is added to equation (2.35) giving

$$U_o A_o = \left(\frac{1}{h_o A_{ann}} + \frac{R''_{fo}}{A_o} + \frac{\ln \frac{d_3}{d_2}}{2\pi k_t L_{eff}} + \frac{\ln \frac{d_2}{d_1}}{2\pi k_c L_{eff}} + \frac{R''_{fi}}{A_i} + \frac{1}{h_i A_i} \right)^{-1} \quad (2.36)$$

where d_1 is the *coated* inner diameter of the tube, and k_c is the thermal conductivity of the coating. The outer convection coefficient remains unchanged, although the inner convection coefficient h_i , is now calculated using d_1 instead of d_2 .

In order to compare different coatings it is necessary to determine their thermal conductivity. The overall heat transfer coefficient is substituted into equation (2.5) to provide an expression for the conductivity of the coating:

$$k_c = \frac{\ln \left(\frac{d_2}{d_1} \right)}{2\pi L_{eff}} \left[\frac{(T_{hi} - T_{co}) - (T_{ho} - T_{ci})}{Q_m \ln \left(\frac{T_{hi} - T_{co}}{T_{ho} - T_{ci}} \right)} - \left(\frac{\pi d_3 L_{eff} k_{fh}}{d_4 - d_3} \cdot Nu_{ann} \right)^{-1} - \frac{\ln \left(\frac{d_3}{d_2} \right)}{2\pi k_t L_{eff}} - \left(\pi L_{eff} k_{fc} \cdot \frac{\left(\frac{fD}{8} \right) Re_c Pr_c}{1 + 12.7 \left(\frac{fD}{8} \right)^{0.5} (Pr^{2/3} - 1)} \right)^{-1} \right]^{-1} \quad (2.37)$$

CHAPTER 2. APPLICABLE THEORY

2.6.3 Coating factor method of analysis

The coating factor may be defined as R_c'' , in which case R_{fi}'' in equation (2.36) is replaced by the coated factor. Substituting equation (2.5) into equation (2.36) and solving for the coating factor:

$$R_c'' = \pi d_2 L_{eff} \left[\frac{(T_{hi} - T_{co}) - (T_{ho} - T_{ci})}{Q_m \ln \left(\frac{T_{hi} - T_{co}}{T_{ho} - T_{ci}} \right)} - \left(\frac{\pi d_3 L_{eff} k_{fh}}{d_4 - d_3} \cdot Nu_{ann} \right)^{-1} - \frac{\ln \left(\frac{d_3}{d_2} \right)}{2\pi k_t L_{eff}} - \left(\pi L_{eff} k_{fc} \cdot \frac{\left(\frac{f_D}{8} \right) Re_c Pr_c}{1 + 12.7 \left(\frac{f_D}{8} \right)^{0.5} (Pr^{2/3} - 1)} \right)^{-1} \right] \quad (2.38)$$

2.6.4 Effective conductivity method of analysis

The thermal conductivity k_{eff} is determined by equating terms 3 and 4 of equation (2.36) to an effective conduction resistance term

$$\frac{\ln \frac{d_3}{d_1}}{2\pi k_{eff} L_{eff}} = \frac{\ln \frac{d_3}{d_2}}{2\pi k_t L_{eff}} + \frac{\ln \frac{d_2}{d_1}}{2\pi k_c L_{eff}} \quad (2.39)$$

Substituting this term into equation (2.36) and rearranging yields

$$k_{eff} = \frac{\ln \left(\frac{d_3}{d_1} \right)}{2\pi L_{eff}} \left[\frac{(T_{hi} - T_{co}) - (T_{ho} - T_{ci})}{Q_m \ln \left(\frac{T_{hi} - T_{co}}{T_{ho} - T_{ci}} \right)} - \left(\frac{\pi d_3 L_{eff} k_{fh}}{d_4 - d_3} \cdot Nu_{ann} \right)^{-1} - \left(\pi L_{eff} k_{fc} \cdot \frac{\left(\frac{f_D}{8} \right) Re_c Pr_c}{1 + 12.7 \left(\frac{f_D}{8} \right)^{0.5} (Pr^{2/3} - 1)} \right)^{-1} \right]^{-1} \quad (2.40)$$

2.7 Determining the uncertainty in the measured thermal conductivity

It is necessary to clarify the difference between experimental error and uncertainty before estimating the uncertainty in the measured conductivity. Consideration of error propagation, using the Taylor Series Method (TSM), follows. The error propagation gives rise to correlated uncertainties, which are dealt with in terms of random and systematic correlated uncertainties. Indeed, by proper analysis of each uncertainty component the overall uncertainty is reduced as far as possible through careful experimental planning.

CHAPTER 2. APPLICABLE THEORY

2.7.1 Error versus uncertainty of a single measured variable

Any measured variable is subject to experimental error. As shown in figure 2.5, the experimental error δ , is equal to the difference between the measured value of a variable and the true value. The true value of a measured variable X , may then be written as

$$X_{\text{true}} = X + \delta \quad (2.41)$$

The issue is that the error is of unknown sign and magnitude in actual measurements. In the absence of the true value the measured value is used instead, although the expected uncertainty is reported alongside the measured value. The uncertainty then refers to the estimate of the limits of the error associated with this measured value.

With reference to figure 2.5, the error of the i^{th} measurement of variable X has two components, such that

$$\delta_i = \beta - \epsilon_i \quad (2.42)$$

where β represents the systematic error and ϵ_i represents the random error associated with the i^{th} measurement. The systematic error represents the error which does not vary during the test duration, and therefore is unaffected by taking successive readings. The random error, however, is considered variable over the test duration and is likely to change with successive readings.

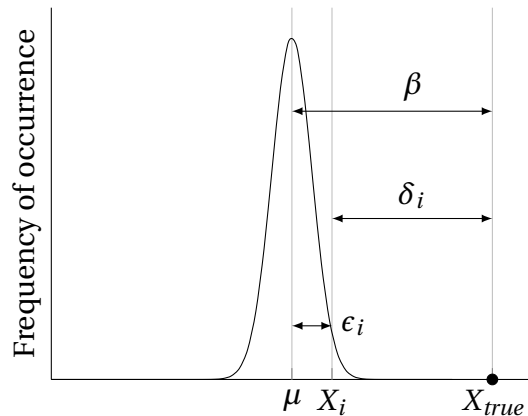


Figure 2.5: Illustration of measurement error

An uncertainty analysis requires estimating the interval around the measured variable which encompasses the true value. The interval is depicted in figure 2.6, which is equal to $X \pm u_X^+$. This estimate is usually made within a certain confidence level. Unless otherwise stated, a 95% confidence level will be presumed throughout. Numerically stated, if 100 measurements are taken of the variable X , it is expected that the true value will lie within the interval $X \pm u_X^+$ 95 times out of 100.

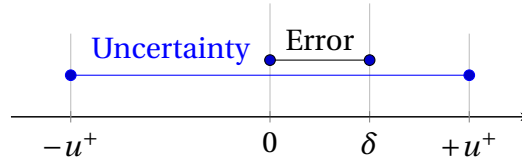


Figure 2.6: Uncertainty interval and error

Statistical methods are used to associate a confidence level with the associated uncertainty u_X^+ . As Coleman & Steele (2009) point out, the Central Limit Theorem states that the error distribution will approach the Gaussian distribution. This allows values from the t -distribution to associate a confidence level to the interval. Specifically the uncertainty is determined as

$$u_X^+ = r_{\%} u_X \quad (2.43)$$

where $r_{\%}$ is the coverage factor and u_X is termed the standard uncertainty of X . The standard uncertainty is in effect the standard deviation of the distribution of the total error δ . Using the large sample approximation, Coleman & Steele (2009) show that

$$u_X^+ \approx 2u_X \quad (2.44)$$

In fact, the total standard uncertainty is composed of a systematic uncertainty component and a random uncertainty component (American Society of Mechanical Engineers (ASME), 2006):

$$u_{X_i} = \sqrt{(s_{X_i})^2 + (b_{X_i})^2} \quad (2.45)$$

The random uncertainty s_X accounts for the random error ϵ , and similarly the systematic uncertainty b_X accounts for the systematic error β .

2.7.2 Random uncertainty

Hypothetically if infinite measurements of the variable X could be taken, the amount of scatter caused by the random uncertainty could be statistically characterized by the population standard deviation, σ . For a normally (Gaussian) distributed population the resulting frequency distribution is plotted in figure 2.5. Also the population mean, or average reading, could be described by the parameter μ . Practically only a finite number of measurements of the variable are possible, in which case the population mean (μ) is approximated using the sample mean (\bar{X}). This means for N measurements of X

$$\mu \approx \bar{X} = \frac{1}{N} \sum_{i=1}^N X_i \quad (2.46)$$

CHAPTER 2. APPLICABLE THEORY

Similarly the population standard deviation is approximated using the sample standard deviation s_X , where

$$s_X = \sqrt{\sum_{i=1}^N \frac{(X_i - \bar{X})^2}{N - 1}} \tag{2.47}$$

The error introduced by approximating the population standard deviation using the sample standard deviation can be reduced by increasing the number of measurements taken. Assuming the random standard uncertainty is normally distributed as well, the interval defined by $\bar{X} \pm 2s_{\bar{X}}$ estimates the true population mean with 95% confidence. The random standard uncertainty of the sample mean $s_{\bar{X}}$, is determined according to

$$s_{\bar{X}} = \frac{s_X}{\sqrt{N}} \tag{2.48}$$

2.7.3 Systematic uncertainty

The systematic uncertainty represents the error which does not change with the number of readings taken. Historically this has been referred to as the ‘bias’. According to the American Society of Mechanical Engineers (ASME) (2006) the elemental sources causing the systematic error may include imperfect calibration corrections, measurement methods and data reduction techniques. Notwithstanding the assumption that all calibration corrections have been applied, a systematic error is still evident, although it is reduced as far as practically possible. Calibration therefore minimizes the systematic error as far as possible.

The total systematic error β_X affecting variable X generally arises from a number of elemental systematic error sources denoted β_{X_k} , where the second subscript k , denotes a specific error source. The elemental systematic errors affecting the measurement of variable X are shown in figure 2.7.

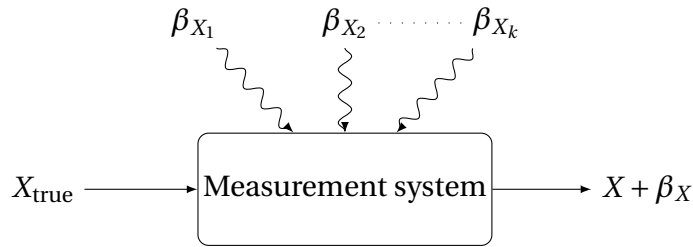


Figure 2.7: Systematic elemental errors affecting variable X

Although each systematic error source contributes a fixed error, the actual value of this error is unknown. By postulating that the elemental systematic error source

CHAPTER 2. APPLICABLE THEORY

comes from a hypothetical population of possible error values, statistical tools are used to estimate the interval in which the error lies. This interval is estimated using the standard deviation of the hypothetical population, which is termed the systematic standard uncertainty b_{X_k} .

The total systematic uncertainty of the measured variable X is calculated as

$$b_X = \left(\sum_{k=1}^K b_k^2 \right)^{\frac{1}{2}} \quad (2.49)$$

Estimating the systematic standard uncertainty for the error sources can be done in a number of different ways. These include using calibration data, the manufacturer's accuracy specifications, as well as additional specifically designed experiments (performed separately from the original experiment).

This concept is clarified by considering the common elemental error source resulting from imperfect calibration. Suppose a manufacturer produces 1 000 particular model instruments and calibrates them to within an accuracy of $\pm A$. If those instruments are re-tested under the same conditions, a distribution shown in figure 2.8 is likely to arise.

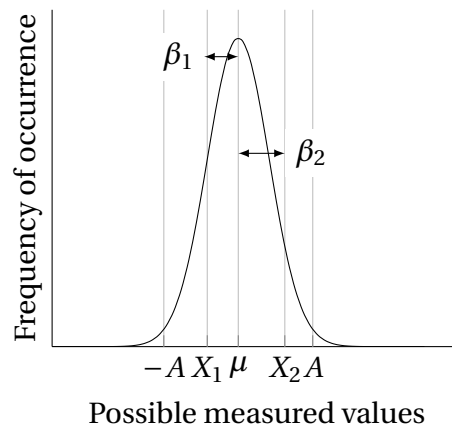


Figure 2.8: Frequency distribution arising from measurements taken from 1 000 similar instruments tested in the absence of random error sources

By assuming a normal (Gaussian) distribution, it is estimated that 950 of the instruments will read a value within the interval $[-A; A]$ when subjected to exactly the same measurement condition (assuming 95% confidence). The systematic standard uncertainty then represents the sample standard deviation of this distribution. Although for a particular instrument the systematic error is still fixed, the frequency analysis of 1 000 similar instruments yields an estimate for the likely value of one particular instrument. Thus the use of the postulated distribution for the systematic

CHAPTER 2. APPLICABLE THEORY

errors does not contradict the definition of a systematic error, but rather is a tool for estimating the value of this error.

2.7.4 Error propagation and the Taylor Series Method

The previous section has dealt with the uncertainty in a single measured variable X . However, the experimental result is often not directly measured but calculated from other measured variables. Consider the thermal conductivity calculated in equation (2.37). In addition to Nu_{ann} , the conductivity depends on the following measured variables:

$$k_c = f^{cn}(L_{eff}, d_4, d_3, d_2, d_1, k_t, V_h, V_c, T_{hi}, T_{ho}, T_{ci}, T_{co}, \Delta T_c, \Delta T_h) \quad (2.50)$$

Each elemental error associated with these measured variables is propagated through the data reduction equation (DRE), i.e. equation (2.37), resulting in a total error δ_{k_c} . To calculate the uncertainty which estimates the limits of this error, each elemental uncertainty is propagated through the DRE. Two methods of propagating the uncertainties are the Taylor Series Method (TSM) and the Monte Carlo method. The TSM is used in this thesis.

The uncertainty in the calculated thermal conductivity k_c , is determined according to

$$u_{k_c}^2 = s_{k_c}^2 + b_{k_c}^2 \quad (2.51)$$

where s_{k_c} represents the random standard uncertainty and b_{k_c} is the systematic standard uncertainty.

Coleman & Steele (2009) derive the TSM propagation equation which, applied to the random uncertainty in the measured conductivity, yields

$$s_{k_c}^2 = \sum_{j=1}^J \left(\frac{\partial k_c}{\partial X_j} \right)^2 s_{X_j}^2 + \left(\begin{array}{c} \text{random correlated} \\ \text{uncertainties} \end{array} \right) \quad (2.52)$$

where X_j refers to the j^{th} functional variable of k_c , and J is the total number of these variables. The partial derivative terms are referred to as the sensitivity coefficients. The correlated uncertainties arise when elemental errors affecting the measured variables are not independent. An example is when two temperature probes are calibrated against the same standard. The correlated uncertainties are dealt with in section 2.7.5.

Similarly for the systematic uncertainty in the measured thermal conductivity

$$b_{k_c} = \sum_{j=1}^J \left(\frac{\partial k_c}{\partial X_j} \right)^2 b_{X_j}^2 + \left(\begin{array}{c} \text{systematic correlated} \\ \text{uncertainties} \end{array} \right) \quad (2.53)$$

CHAPTER 2. APPLICABLE THEORY

Considering equations (2.52) and (2.53), it is clear that the root sum square approach of the TSM effectively magnifies the largest uncertainty contributors. Tacitly implied by the partial derivatives is the fact that the TSM assumes the function k_c to be continuous.

The partial derivatives of the absolute sensitivity coefficients are evaluated numerically using the following central differencing formula:

$$\frac{\partial k_c}{\partial X_j} = \frac{k_c(X_j + h) - k_c(X_j - h)}{2\zeta} \quad (2.54)$$

where the step size ζ is determined as

$$\zeta = \sqrt{\text{eps}X_j} \quad (2.55)$$

and eps is the machine epsilon (2^{-52}). These coefficients may be normalized by multiplying by X_j/k_c . The resulting normalized sensitivity coefficients are referred to as uncertainty magnification factors (UMFs) because they indicate the relative influence a variable has on the systematic uncertainty. Thus

$$\text{UMF}_j = \frac{X_j}{k_c} \frac{\partial k_c}{\partial X_j} \quad (2.56)$$

If the UMF of a variable is greater than unity, it means that the uncertainty in that variable magnifies the overall systematic uncertainty, as it propagates through the data reduction equation. Likewise, an UMF less than unity indicates a diminishing influence of the uncertainty in that particular variable, as it propagates through the data reduction equation.

Methods of estimating the correlated uncertainties are provided in the following section.

2.7.5 Accounting for correlated uncertainties

Correlated uncertainties exist in equations (2.52) and (2.53) because not all the errors affecting each of the measured variables are necessarily independent of one another. As will be seen, the effect of correlated uncertainties may be to either increase the overall error or reduce it, depending on their sign.

Consider a steady state experiment using the heat exchanger in figure 2.1. If an external factor caused a slight fluctuation in the stream inlet temperature, the inlet and outlet temperature sensors would both be affected in the same way. This is an example of a random correlated error between the inlet and outlet temperature sensors. These sensors may also share a systematic correlated error. Supposing that

CHAPTER 2. APPLICABLE THEORY

they were calibrated against the same standard, each sensor would share the same imperfect calibration error.

Random correlated uncertainties are difficult to determine individually. However, they can be included in the overall uncertainty in the measured conductivity by direct calculation. This involves directly calculating the standard deviation from M determinations of k_c . Specifically if measurements are taken every 2 seconds in the above-mentioned steady-state experiment, then the conductivity can be calculated at 2 seconds, 4 seconds, ... M seconds. Then Coleman & Steele (2009) show that direct calculation of the standard deviation is equal to

$$(s_{k_c})_{\text{direct}} = \left[\frac{1}{M-1} \sum_{i=1}^M (k_{c_i} - \overline{k_c})^2 \right]^{\frac{1}{2}} \quad (2.57)$$

where the mean conductivity is calculated using

$$\overline{k_c} = \frac{1}{M} \sum_{i=1}^M k_{c_i} \quad (2.58)$$

The random uncertainty in the mean conductivity is then

$$s_{\overline{k_c}} = \frac{(s_{k_c})_{\text{direct}}}{\sqrt{M}} \quad (2.59)$$

Calculating the random uncertainty in this way incorporates the random correlated uncertainties automatically. On the other hand, systematic correlated uncertainties can be approximated using the TSM approach and covariance factors.

The systematic correlated uncertainties are approximated using covariance factors. Specifically suppose that variables X_j and X_i share identical systematic error sources. The systematic covariance factor between these two variables is then called $b_{X_j X_i}$. Brown *et al.* (1996), cited by Coleman & Steele (2009), found the most satisfactory estimation of the covariance factor to be

$$b_{X_j X_i} = \sum_{\alpha=1}^L b_{X_{j\alpha}} b_{X_{i\alpha}} \quad (2.60)$$

where L is the total number of shared elemental systematic errors.

The systematic uncertainty in the measured conductivity, including the correlation uncertainties, is then equal to

$$b_{k_c}^2 = \sum_{j=1}^J \left(\frac{\partial k_c}{\partial X_j} \right)^2 b_{X_j}^2 + 2 \sum_{j=1}^{J-1} \sum_{l=j+1}^J \left(\frac{\partial k_c}{\partial X_j} \right) \left(\frac{\partial k_c}{\partial X_l} \right) b_{X_j X_l} \quad (2.61)$$

CHAPTER 2. APPLICABLE THEORY

where the terms containing b_{X_j, X_l} are the covariance factors.

Most importantly the covariance factor terms in equation (2.61) are not squared. This means that if the partial derivatives of k_c with respect to variables j and l are of opposing sign, then the covariance term will be negative. This will effectively reduce the systematic uncertainty in the measured conductivity. Exploiting this fact, a significant reduction in the systematic error can be achieved by careful experimental planning.

Suppose that the inner tube of the heat exchanger shown in figure 2.1 is initially uncoated. If a number of tests are conducted on the heat exchanger, the outer Nusselt number can be measured for various flow rates. The outer Nusselt number can then be regressed over this range of Reynolds numbers. The outer Nusselt number is written as

$$Nu_{ann} = A_{Nu} Re_h^{B_{Nu}} Pr_h^{0.3} \quad (2.62)$$

where A_{Nu} and B_{Nu} are experimentally determined regression coefficients. The seemingly arbitrary nature of the choice of these coefficients will be clarified in chapter 4. The regression coefficients are determined from the uncoated test data. Hence the outer Nusselt number may be written functionally as

$$Nu_{ann} = f^{cn}(A_{Nu}, B_{Nu}, Re_{h_{new}}, Pr_{h_{new}}) \quad (2.63)$$

where $Re_{h_{new}}$ and $Pr_{h_{new}}$ are the values at which the Nusselt number is being calculated, also

$$A_{Nu} = f^{cn}(T_{hi}(i), T_{ho}(i), T_{ci}(i), T_{co}(i), V_h(i), V_c(i), \Delta T_h(i), \Delta T_c(i)) \quad (2.64)$$

and likewise for B_{Nu} . i refers to a particular uncoated test.

The left-hand path in figure 2.9 shows the systematic errors affecting the uncoated tests. Let N denote the number of uncoated tests used in determining the regression coefficients.

Next consider coating the inner tube and testing it at the same conditions, as shown in the right-hand side of figure 2.9. The regression data from the uncoated tests can then be used to estimate the outer Nusselt number. In so doing, the systematic error associated with the temperature and volumetric flow rate measurements will be correlated. This is because exactly the same equipment is used, and the elemental systematic errors affecting the instruments remain unchanged (assuming negligible drift). As already noted, if the partial derivatives of the covariance terms are of opposing signs, then the effect of these correlated systematic errors will be to reduce the overall uncertainty in the measured thermal conductivity.

Furthermore, L_{eff} , d_4 , d_3 and d_2 are measured only once and these measured values are used in the uncoated as well as the coated tests. The uncertainties associated with these variables are effectively frozen in the regression data from the uncoated

CHAPTER 2. APPLICABLE THEORY

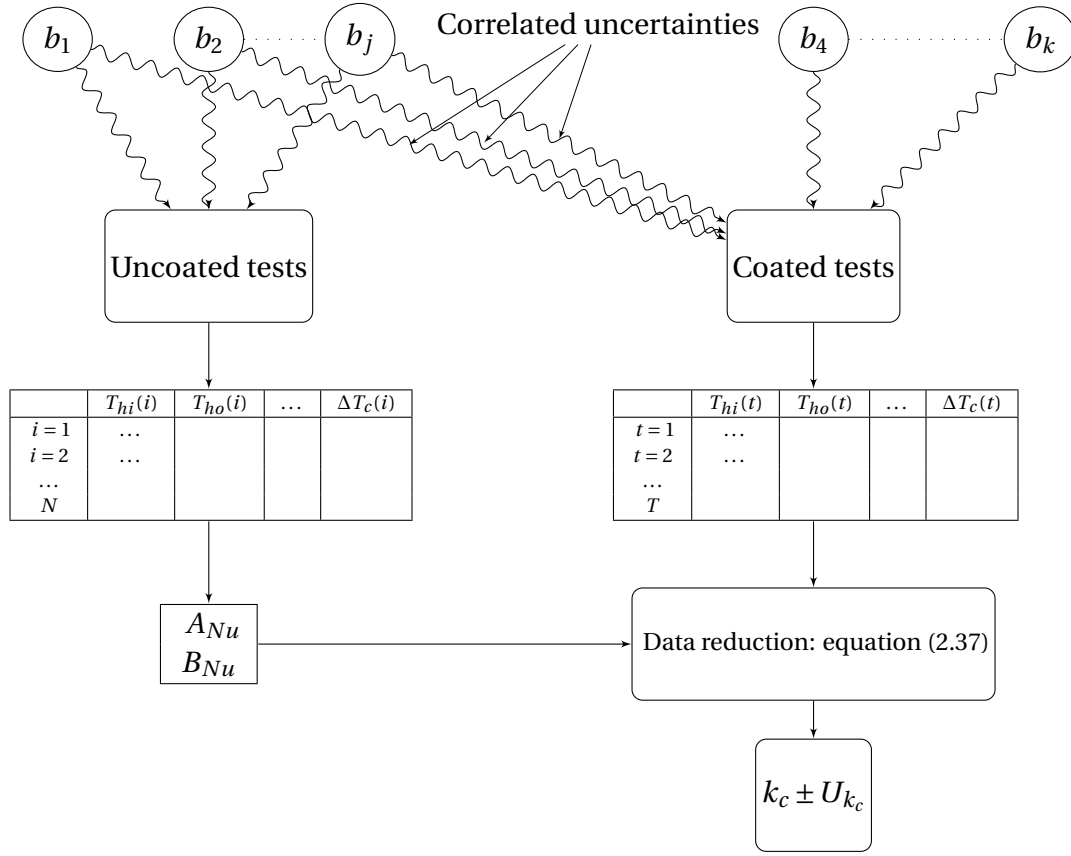


Figure 2.9: Uncertainty propagation including the correlated error effects between uncoated and coated tests

tests. Thus they do not contribute to the systematic uncertainty in the coating conductivity. Also the thermal conductivity of the tube k_t remains the same. As such equation (2.50) reduces to

$$k_c = f^{cn}(d_1, T_{hi}, T_{ho}, T_{ci}, T_{co}, V_h, V_c, \Delta T_h, \Delta T_c, A_{Nu}, B_{Nu}) \quad (2.65)$$

Hence the experimental approach to test the tube before and after coating reduces the systematic uncertainty in two ways. First, the uncertainty associated with the variables: L_{eff} , d_4 , d_3 , d_2 , and k_t are effectively calibrated out of the uncertainty equation. Second, the correlated uncertainties between common instruments may be of opposing sign, which will reduce the overall uncertainty further. The means of determining the overall uncertainty in the measured conductivity, including these correlated uncertainties, is dealt with next.

2.7.6 Uncertainty in the measured conductivity including the regression uncertainty

By experimentally testing the annular convection coefficient, the conductivity becomes a function of the regression coefficients A_{Nu} and B_{Nu} (equation 2.65). The uncertainty associated with these coefficients must also be propagated through the DRE. The correlated uncertainties that arise must once again be accounted for by determining the covariance factors.

Consider the correlated uncertainties associated with the hot stream inlet temperature measurement $T_{hi}(t)$, shown in figure 2.10. Since the temperature sensors are assumed to be calibrated against the same standard, and the same equipment is used, their uncertainties will be correlated.

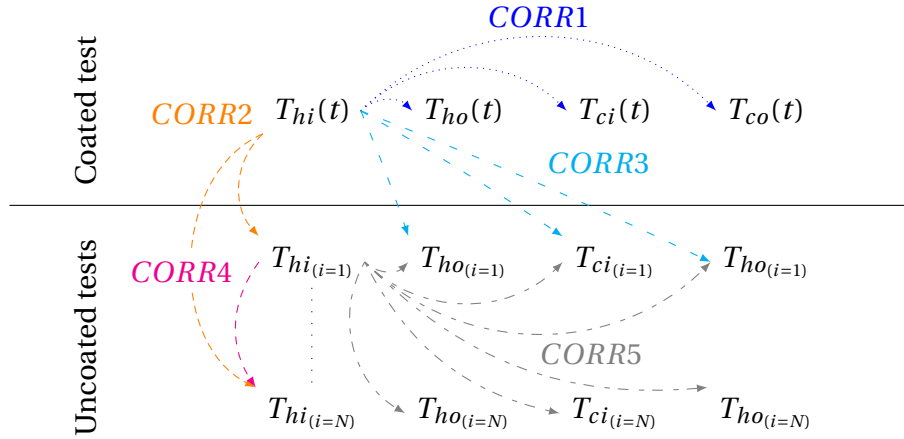


Figure 2.10: Diagram showing correlation terms between temperature measurements during uncoated and coated tests

In the coated test, the covariance terms between $T_{hi}(t)$ and the inlet and outlet temperatures, denoted $CORR1$, is equal to

$$CORR1 = 2 \sum_{j=1}^{J-1} \sum_{l=j+1}^J \left(\frac{\partial k_c}{\partial X_j(t)} \right) \left(\frac{\partial k_c}{\partial X_l(t)} \right) b_{X_j(t)X_l(t)} \quad (2.66)$$

Similarly for the uncoated tests

$$CORR5 = 2 \sum_{i=1}^N \sum_{m=1}^N \sum_{j=1}^{J-1} \sum_{l=j+1}^J \left(\frac{\partial k_c}{\partial X_{ji}} \right) \left(\frac{\partial k_c}{\partial X_{lm}} \right) b_{X_{ji}X_{lm}} \quad (2.67)$$

$CORR2$ and $CORR4$ represent the correlation between variables in the coated and uncoated tests, which are measured with the same equipment. These are calculated

CHAPTER 2. APPLICABLE THEORY

respectively as

$$CORR2 = 2 \sum_{i=1}^N \sum_{j=1}^J \left(\frac{\partial k_c}{\partial X_j(t)} \right) \left(\frac{\partial k_c}{\partial X_{j_i}} \right) b_{X_j(t)X_{j_i}} \quad (2.68)$$

and

$$CORR4 = 2 \sum_{i=1}^N \sum_{m=i+1}^N \sum_{j=1}^J \left(\frac{\partial k_c}{\partial X_{j_i}} \right) \left(\frac{\partial k_c}{\partial X_{j_m}} \right) b_{X_{j_i}X_{j_m}} \quad (2.69)$$

Lastly the correlations between $T_{hi}(t)$ measured during a coated test and the other temperatures measured during uncoated tests is calculated according to

$$CORR3 = 2 \sum_{i=1}^N \sum_{j=1}^{J-1} \sum_{l=1, l \neq j}^J \left(\frac{\partial k_c}{\partial X_j(t)} \right) \left(\frac{\partial k_c}{\partial X_{l_i}} \right) b_{X_j(t)X_{l_i}} \quad (2.70)$$

These correlation terms are added together with the regression uncertainty (using the TSM approach) to equation (2.61) to yield the total standard systematic uncertainty in the measured conductivity, namely

$$b_{k_c}^2 = \sum_{j=1}^J \left(\frac{\partial k_c}{\partial X_j(t)} \right)^2 b_{X_j(t)}^2 + \sum_{i=1}^N \sum_{j=1}^J \left(\frac{\partial k_c}{\partial X_{j_i}} \right)^2 b_{X_{j_i}}^2 + CORR1 + CORR2 + CORR3 + CORR4 + CORR5 \quad (2.71)$$

Every term appended with a (t) in the above-mentioned equation refers to a variable from the coated test data set. The other terms refer to the variables from the uncoated test data sets which are used in the regression of the annular Nusselt number.

2.8 Determining the uncertainty in the effective coated-tube conductivity

The uncertainty in the effective coated-tube conductivity can be determined analogously to the methods put forth in the previous section. However, the prominent difference is that the effective coated-tube conductivity does not directly depend on the tube internal diameter d_2 . Only A_{Nu} and B_{Nu} depend on this variable.

$$k_{eff} = f^{cn}(T_{hi}, T_{ho}, T_{ci}, T_{co}, V_h, V_c, \Delta T_h, \Delta T_c, A_{Nu}, B_{Nu}) \quad (2.72)$$

Therefore, from inspection,

$$(s_{k_{eff}})_{\text{direct}} = \left[\frac{1}{M-1} \sum_{i=1}^M (k_{eff_i} - \bar{k}_{eff})^2 \right]^{\frac{1}{2}} \quad (2.73)$$

CHAPTER 2. APPLICABLE THEORY

where the mean effective coated-tube conductivity is calculated using

$$\bar{k}_{eff} = \frac{1}{M} \sum_{i=1}^M k_{eff_i} \quad (2.74)$$

The random uncertainty in the mean effective coated-tube conductivity is then

$$s_{\bar{k}_{eff}} = \frac{(s_{k_{eff}})_{direct}}{\sqrt{M}} \quad (2.75)$$

Finally the total standard systematic uncertainty in the effective coated-tube conductivity is

$$\begin{aligned} b_{k_{eff}}^2 = & \sum_{j=1}^J \left(\frac{\partial k_{eff}}{\partial X_j(t)} \right)^2 b_{X_j(t)}^2 + \sum_{i=1}^N \sum_{j=1}^J \left(\frac{\partial k_{eff}}{\partial X_{j_i}} \right)^2 b_{X_{j_i}}^2 \\ & + 2 \sum_{j=1}^{J-1} \sum_{l=j+1}^J \left(\frac{\partial k_{eff}}{\partial X_j(t)} \right) \left(\frac{\partial k_{eff}}{\partial X_l(t)} \right) b_{X_j(t)X_l(t)} \\ & + 2 \sum_{i=1}^N \sum_{j=1}^J \left(\frac{\partial k_{eff}}{\partial X_j(t)} \right) \left(\frac{\partial k_{eff}}{\partial X_{j_i}} \right) b_{X_j(t)X_{j_i}} \\ & + 2 \sum_{i=1}^N \sum_{j=1}^{J-1} \sum_{l=1, l \neq j}^J \left(\frac{\partial k_{eff}}{\partial X_j(t)} \right) \left(\frac{\partial k_{eff}}{\partial X_{l_i}} \right) b_{X_j(t)X_{l_i}} \\ & + 2 \sum_{i=1}^N \sum_{m=i+1}^N \sum_{j=1}^J \left(\frac{\partial k_{eff}}{\partial X_{j_i}} \right) \left(\frac{\partial k_{eff}}{\partial X_{j_m}} \right) b_{X_{j_i}X_{j_m}} \\ & + 2 \sum_{i=1}^N \sum_{m=1}^N \sum_{j=1}^{J-1} \sum_{l=j+1}^J \left(\frac{\partial k_{eff}}{\partial X_{j_i}} \right) \left(\frac{\partial k_{eff}}{\partial X_{l_m}} \right) b_{X_{j_i}X_{l_m}} \end{aligned} \quad (2.76)$$

In summary, determining the uncertainty in the measured coating conductivity and effective coated-tube conductivity requires estimating the random and systematic uncertainties. Since neither the coating conductivity nor the effective coated-tube conductivity is directly measured, the respective uncertainties must be propagated through the data reduction equations. This gives rise to correlated random and systematic uncertainties. Random uncertainty, including the random correlated uncertainty, can be estimated directly from the calculated result in a steady state test. Conversely the systematic uncertainty is determined using the TSM approach, and the use of covariance factors are needed to account for the systematic correlated uncertainty. Reducing the overall uncertainty requires testing the tube before and after coating, using exactly the same apparatus. The apparatus used in such testing is detailed in the following chapter.

Chapter 3

Experimental facility

Overview

The performance data obtained in this thesis are experimentally determined using a convection heat transfer facility that was designed, built and commissioned for this study. This chapter provides a description of this apparatus, including the process and instrument diagrams. Details pertaining to the instrumentation and measurement techniques are then considered in depth. Finally the methodology and test procedures are clearly stated, which highlight the test tube surface preparation.

3.1 Description of the apparatus

The convection heat transfer facility consists of two main fluid circuits: the cold and hot water loops. The schematic is provided in figure 3.1. The horizontal double-pipe counter-flow heat exchanger (6) is used to test the performance of a single test tube. The facility features 12 kW of heating input as well as a 24 kW evaporative cooling tower³. The piping and instrument diagram (figure 3.2) illustrates these two closed circuits and shows the position of the measurement points.

The first circuit begins by pumping heated water (at approximately 38 °C) through a 30 mm orifice plate which is 80 mm upstream of point 1 in figure 3.1. The orifice plate is used to promote mixing, so that the bulk hot inlet temperature can be measured effectively. Thereafter the heated water enters the annular region of the heat exchanger. The effective heat transfer length is 1981 mm. After exiting the heat exchanger at a lower temperature, the hot stream passes through another 30 mm orifice plate before the bulk temperature is measured at point 3 in figure 3.1. An electromagnetic 1 inch flow meter determines the flow rate by measuring the voltage produced

³Heat duty based on water inlet temperature of 32 °C, air dry-bulb temperature of 30 °C and wet-bulb temperature of 20 °C.

CHAPTER 3. EXPERIMENTAL FACILITY

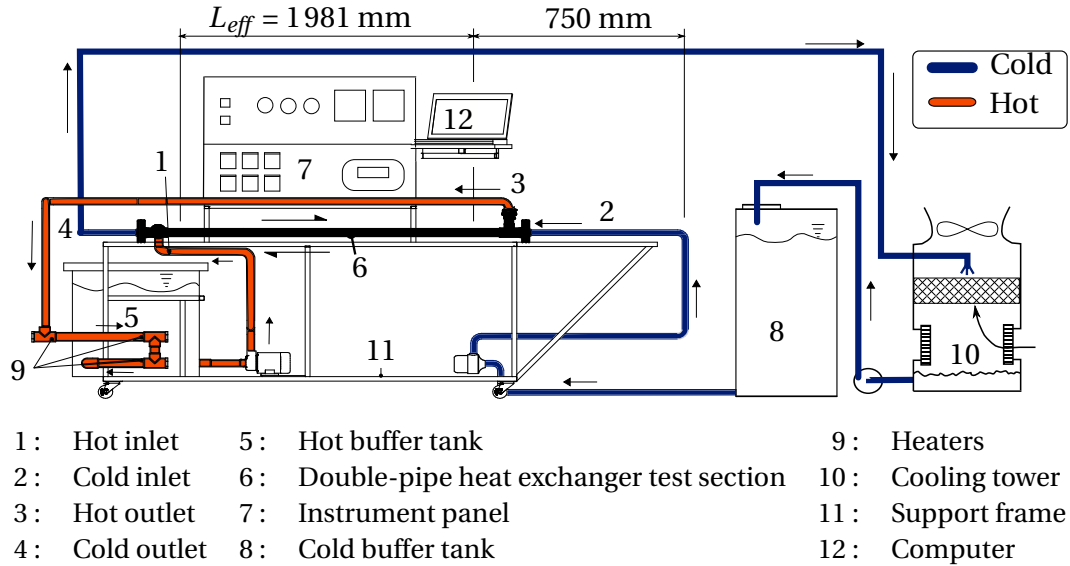


Figure 3.1: Schematic of experimental facility

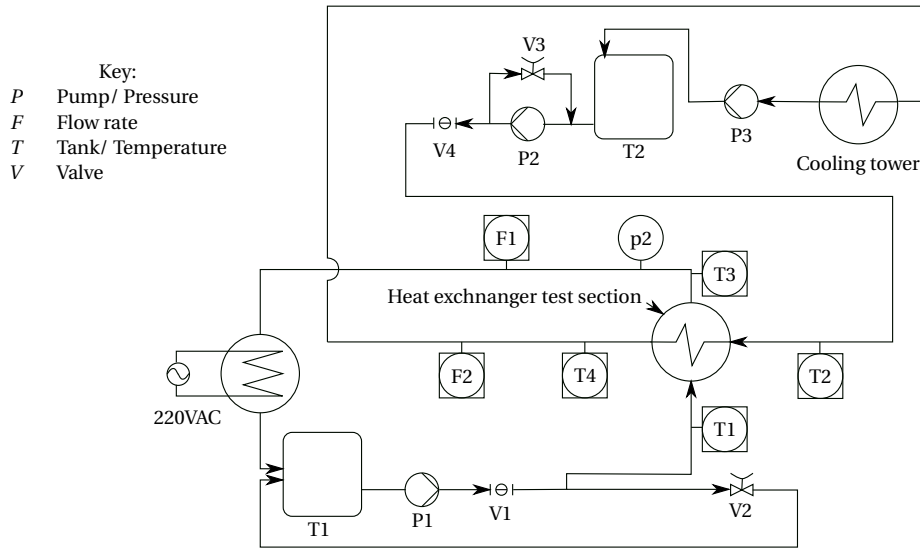


Figure 3.2: Piping and instrumentation diagram of apparatus

as the water passes through the imposed magnetic field. Three 3 kW in-line heaters and three 1.5 kW immersion heaters are controlled using a thyristor to heat the returning water (point 9, figure 3.1).

Cooling water supplied from a 2500 L polyethylene cold reservoir (8) passes through a similar orifice plate before its bulk temperature is measured at point 2. It then flows

CHAPTER 3. EXPERIMENTAL FACILITY

through the inside of the test tube, where an entrance length of 760 mm provided before entering the heat exchanger. The exit temperature is measured at point 4, and thereafter an identical type flow meter measures the cold stream flow rate. Finally the cold stream is pumped to the cooling tower (10) before returning to the cold reservoir.

The actual conditions experienced by the condenser tubes in service are replicated as far as possible. The salient difference is that hot water instead of condensing steam is used on the outside surface of the tube. The principle reason for using hot water instead of condensing steam is to reduce the additional uncertainty inherent in the outer convection heat transfer coefficient.

As illustrated in figure 3.3, each heat exchanger comprises two flow preconditioning annuli. The preconditioning annuli are necessary to remove distortions in the flow pattern caused by the circular to annular area transition. Heat transfer is essentially prevented in this section by means of an air gap.

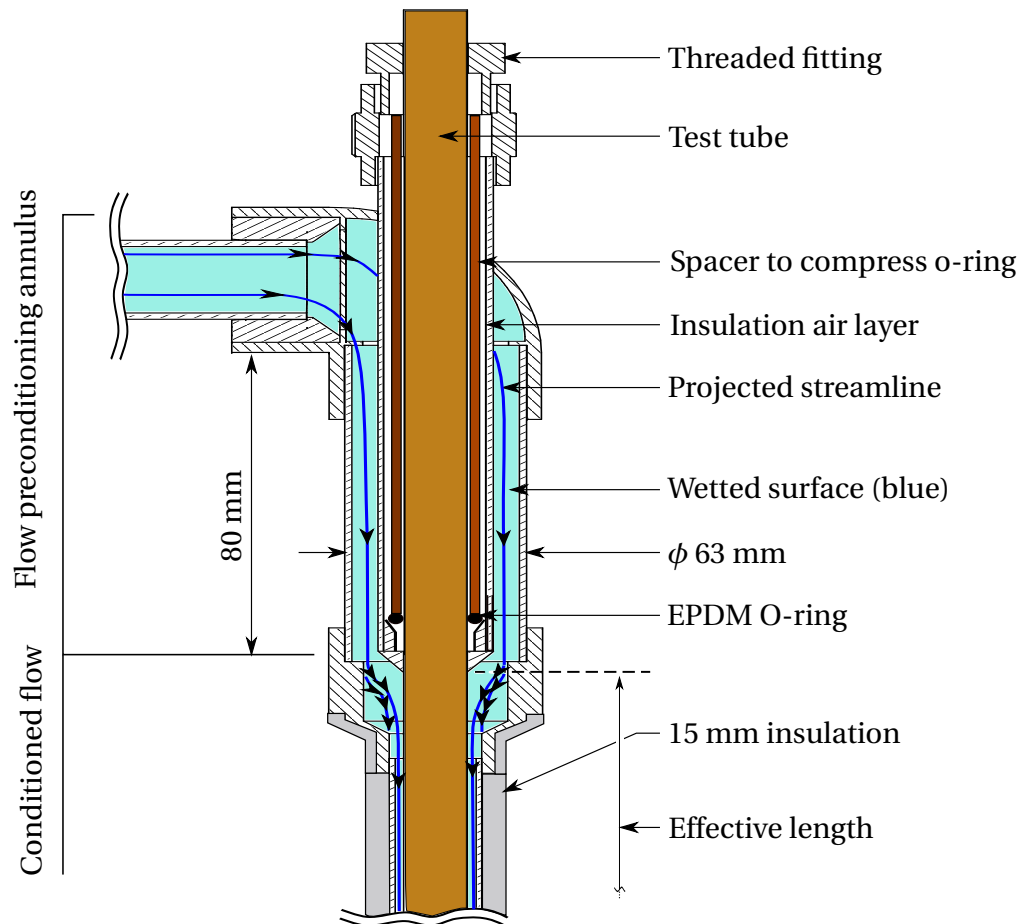


Figure 3.3: Cross-sectional view of preconditioning annulus (rotated plan view)

CHAPTER 3. EXPERIMENTAL FACILITY

The resulting flow field is thus more uniform before it comes into contact with the test tube. With such a smooth transition, flow separation is minimized and the flow approaches fully developed flow. This allows comparison with existing convection coefficient correlations which are determined for fully developed flow conditions. The o-ring glands form a non-permanent seal allowing interchangeability of test tubes.

The heat exchanger annulus is varied according to the test tube diameter. Using 32 mm and 40 mm class 12 PVC clear tubing, test tubes in the ranges shown in table 3.1 are tested. PVC has a very low thermal conductivity of 0.19 W/m·K (Cengel & Ghajar, 2011), which limits heat transfer with the surroundings. Furthermore, 15 mm closed-cell polyethylene foam is wrapped tightly around the heat exchanger.

Table 3.1: Annulus tubing sizes and test tube diameter ranges

Heat exchanger	Outer jacket diameter mm	Inner jacket diameter mm	Test tube diameter mm
1	32	27	19–23
2	40	33.55	24–26

3.2 Measurement techniques and instrumentation

The measurement system includes four resistance temperature detectors (RTDs), eight type J thermocouples, two flow rate meters, and a differential pressure transducer. A total of 15 channels are sequentially sampled every 2 seconds using a *DT80 Datalogger* data logger (certificate in section E). Details of each subsystem are explained below.

3.2.1 Temperature measurement

The heat exchanger analysis (chapter 2) required accurate measurements of the bulk fluid temperatures. Most importantly the bulk temperature difference between each inlet and outlet is required. Furthermore the point temperatures at the inlet and outlets are required to determine the thermophysical property data.

To measure the bulk fluid temperature, temperature sensing probes are inserted into the flow, as close as possible to the inlets and outlets of the heat exchanger. When selecting the type of temperature sensors, consideration must be given to the operating temperatures (between 5 °C and 50 °C), the required accuracy and budget allowances. For this application, class AA *Pt100* resistance temperature detectors (RTDs), and type J thermocouples (T/C's) are selected. An accurate measurement of the temperature difference between the inlets and outlets, is achieved by using a

CHAPTER 3. EXPERIMENTAL FACILITY

thermopile as illustrated in figure 3.4. By connecting the two T/C pairs in this series arrangement, the sensitivity is doubled. In general the electromotive force (EMF) is proportional to the number of thermocouple pairs. The RTDs provide an absolute

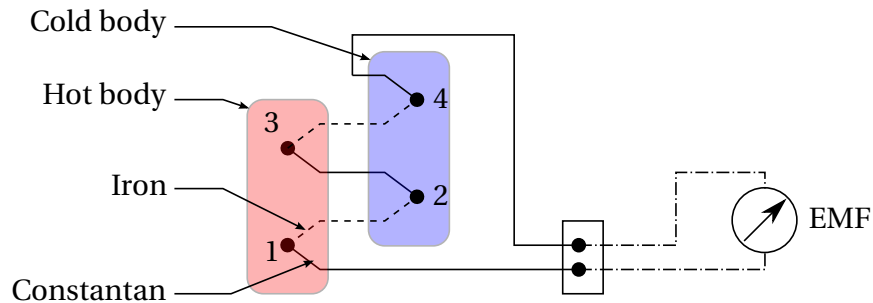


Figure 3.4: Schematic of a thermopile used to measure temperature differential

temperature measurement that is used to calculate the fluid thermodynamic properties. They are also used to indirectly measure the temperature difference, and these readings are compared to those measured using the thermopiles in a later section.

The arrangement of the temperature probes is shown in figure 3.5. To achieve the maximum insertion depth, the probes are inserted into a 90° T-piece, thereby reducing adverse heat transfer from the surroundings.

Orifice plates are installed upstream of the measurement points. The constriction in the flow causes effective mixing within the fluid, allowing for a more representative measurement of the bulk fluid temperature.

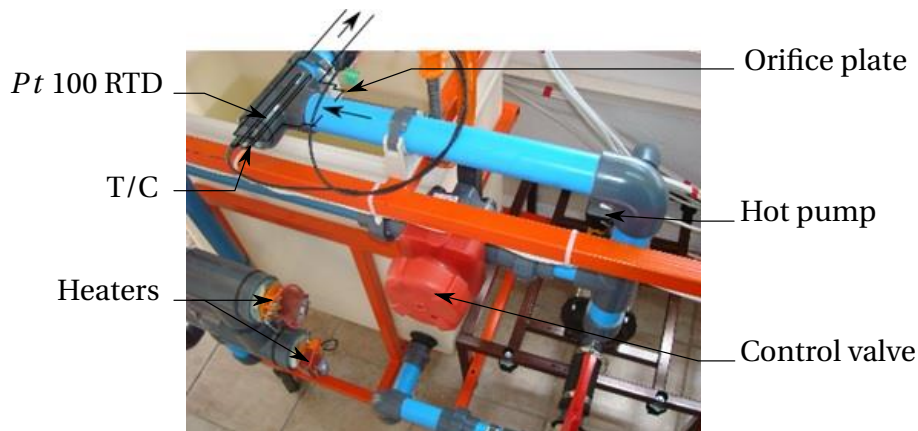


Figure 3.5: Annotated photograph of the hot inlet temperature station

Although the certificates of conformance were ordered with the class AA RTDs, these were not supplied by the manufacturer. For this reason, each of the sensor re-

CHAPTER 3. EXPERIMENTAL FACILITY

sistances are verified at 0.01 °C using the apparatus shown in figure 3.6. A *Fluke* reference thermometer of accuracy 0.05 °C is used to determine the absolute temperature of the water bath and to monitor its stability.

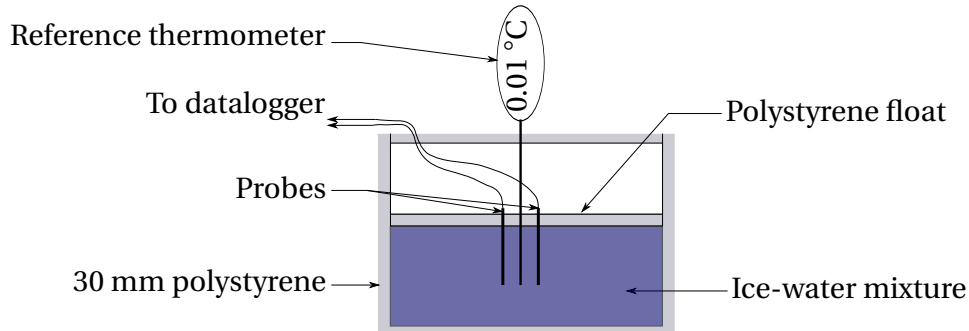


Figure 3.6: Waterbath used to verify *Pt* 100 RTD resistances

The results from this validation test is tabulated in table 3.2. The measured resistances at 0.01 °C indicate conformance of these probes to the tolerance of $\pm 0.06 \Omega$ at 0 °C set out in DIN-IEC-751. The measured resistances are converted to temperatures using the linearized coefficient equal $0.003850 \frac{\Omega}{^{\circ}\text{C}}$ in accordance with DIN43760-1980, IEC751-1983.

Table 3.2: Results from water bath validation test

Probe	Resistance Ω
Hot inlet	100.03
Hot exit	100.04
Cold inlet	100.00
Cold exit	100.01
Reference temperature $0.01 \pm 0.05 \text{ }^{\circ}\text{C}$	

3.2.2 Pressure measurement

The pressure drop measurement is achieved using a *Bailey and Mackey* differential pressure transducer. The manufacturer states the sensor's accuracy is 1% of the actual reading, calibrated from 0 to 100 mbar (certificate in appendix E). Static pressures are measured at two points along the tube, specifically at the inlet and outlet of the heat exchanger. An entrance length of 20 diameters precedes each tapping point.

Each tapping point has an aluminum pipe saddle which is fitted over a rubber gasket. The gasket is grooved so as to form an annular chamber when fitted over

CHAPTER 3. EXPERIMENTAL FACILITY

the tube, as depicted in figure 3.7. Three circumferential tapping holes feed into this chamber to provide an average reading of the static pressure. The chamber is connected to the transducer via 8 mm internal diameter tubing. The 1 mm transverse holes are drilled circumferentially at 0 °, 45 ° and 90 °. Needle reamers are used to remove any burrs around the tapping hole.

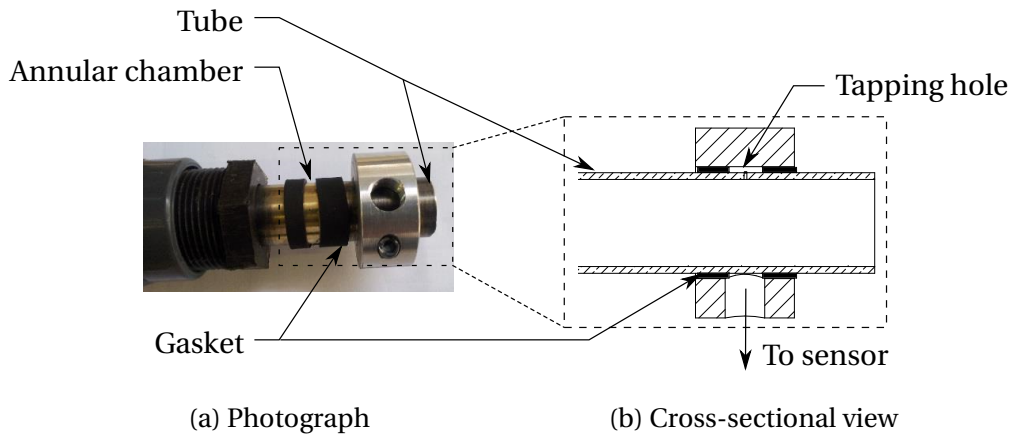


Figure 3.7: Pressure tapping

3.3 Methodology and test procedures

The methodology used in this testing is centered around enforcing repeatable test conditions. A major facet of this, is the test tube surface preparation which is discussed first. Then the test procedures used to conduct the isothermal and load tests are stated. Finally the post-testing inspection discusses how to ensure there are no discontinuities in the coating film.

3.3.1 Test tube surface preparation

The outer surface of the tube is prepared by polishing it to a high metallic luster. The two step polishing preparation begins by sanding the surface using 1 200 grit sandpaper, and then buffing the surface using metal polish. The outer surface preparation process is vital to remove any excessive oxidation or other contaminants on the tube, and thus enforce repeatable testing between different tubes.

Thereafter the inner and outer surfaces of the tube are washed thoroughly using acetone and a lint-free cloth. This is to remove any manufacturing oils and any residue left from polishing.

CHAPTER 3. EXPERIMENTAL FACILITY

After the polishing and cleaning, the tube can be inspected for significant defects which may affect the flow patterns.

3.3.2 Isothermal tests

The 'calibration' loop shown in figure 3.8 is used to conduct isothermal testing. These tests measure losses to the surroundings and therefore check whether adequate insulation is used. Three way valves are used to change between the normal configuration loop and the calibration loop.

In this 'calibration' state, both flow meters and all the temperature probes measure conditions from the same fluid stream. The flow meters are compared against one another to check whether they read the same value within their accuracy tolerances. Provision is also made to check the flow rate with a bucket and stop-watch. After installing the tube into the heat exchanger, a leak test is conducted.

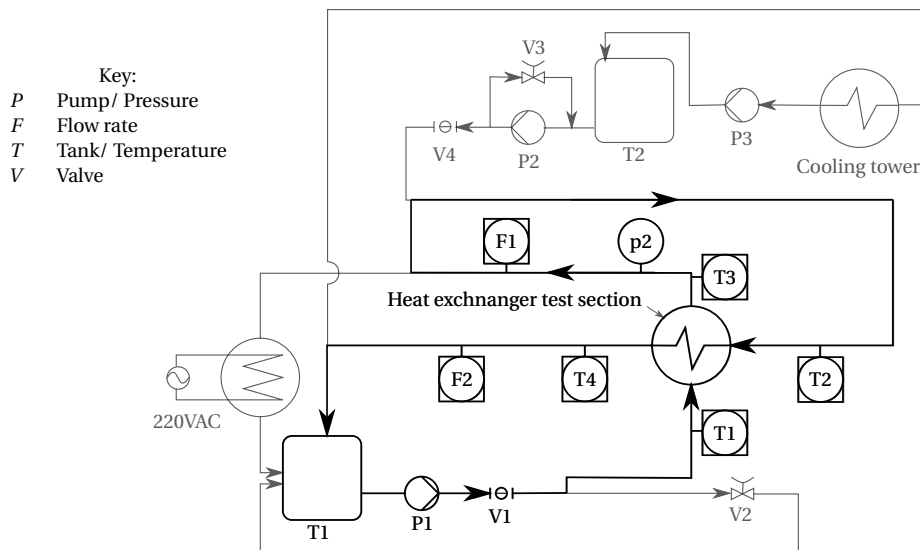


Figure 3.8: Valve orientation and pipe flow comprising 'calibration' loop (shaded loop shows original configuration)

3.3.3 Apparatus heating time constant

Figure 3.9 shows the temperature profiles and ramp-up time after the load test is initiated. The hot water reservoir is preheated to approximately 30 °C. Thereafter the time to reach steady state is approximately 40 minutes, as seen in the figure. The hot inlet temperature trend is also used to confirm this.

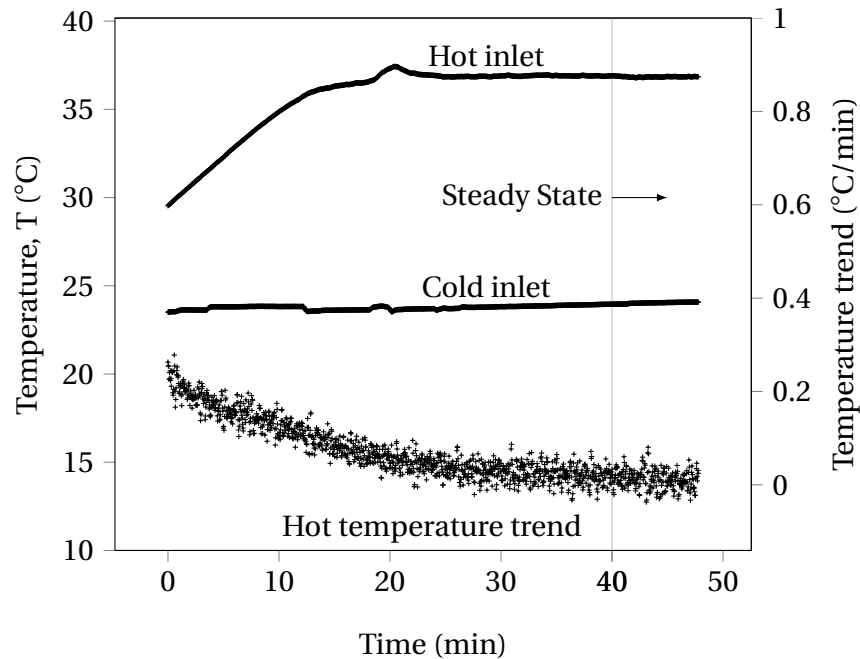


Figure 3.9: Measured inlet temperature profiles from a particular test

3.3.4 Coating the tube and measuring the dry film thickness

After testing the uncoated tube, the heat exchanger is removed from the apparatus as a complete unit with the test tube. All the water is removed from inside the tube before coating. The coating is then applied following exactly the same procedure as is done in-situ (the details of which are proprietary).

The mass of coating, which is applied to the tube, is recorded and later used to determine the dry film thickness of the coating. This enables the average coating thickness to be determined along the length of the tube. Furthermore, by using the same procedure as is used during in-situ coating, the test results accurately reflect the expected performance of actual tubes.

3.3.5 Load tests

Load tests are used to determine the outer Nusselt number as a function of Reynold's number on an uncoated tube. The tube is then coated and the subsequent load tests determine the thermal conductivity of the coating.

The load test begins by adjusting valve V1 (figure 3.2) to its fully open position and closing V2 completely. Ensuring the hot reservoir (T1) level is at its maximum, the hot pump is started and allowed to run for 30 s to purge any air from the system. Valves V1 and V2 are then adjusted in unison to achieve the required flow rate, whilst not

CHAPTER 3. EXPERIMENTAL FACILITY

exceeding 2.5 bar line pressure. Using an external light source, the sight glasses are examined for any air bubbles which may be present as a result of insufficient venting or cavitation. If so, the system must be purged again using the method described previously.

With the hot stream purged and running, the hot temperature controller is set to approximately 38 °C, and the heaters are turned on. Once the temperature of the hot reservoir has reached 80 % of the set temperature, the cold stream may be started. Since the cooling tower is open to atmosphere the cold loop is self venting. Valves V3 (figure 3.2) and V4 are adjusted to reach the required flow rate, as stipulated in table 3.3.

Table 3.3: Maximum and minimum flow rates for outer convection coefficient testing

	Hot flow rate	Cold flow rate	Unit
Min	0.6	0.7	L/s
Max	1.8	1.0	L/s
Set point	[0.85,0.95,...,1.55]	0.79	L/s

Once all the flow rates are set, the data logger is initiated and measurements are taken every 2 seconds. The apparatus is run for 40 minutes to stabilize and reach steady state. A further 5 to 10 minutes are provided to collect steady state data. During this time, the flow rates and temperature readings are monitored to ensure no irregularities occur and all the readings are stable. The test is concluded by following the reverse procedure of start up.

3.3.6 Post-testing inspection

The conductivity testing culminates in a post-test inspection of the coating. Specifically the coating must be inspected for any discontinuities or defects. Traditional methods to verify continuity of the coating include sponge and spark testing. However these methods are ineffective for use on such thin coatings (approximately 50 µm). After exploring different approaches, the most successful method was found to be a visual inspection after longitudinally sectioning the tube.

Depending on the coating, visual inspection is effective for identifying any discontinuities (misses) in the dry coating film. Any coatings that exhibit discontinuities are rejected since they erroneously over-predict the coating performance.

Chapter 4

Experimental testing

Overview

This chapter begins by describing the test tube designation and dimensions. Thereafter the isothermal, uncoated and coated heat transfer tests are expounded in terms of this notation. The uncoated test data is used to determine regression coefficients for the annular Nusselt number as a function of Reynolds number. Using this data, the thermal performance of three coatings is then compared, using the methods of chapter 2 and this regression data. Finally the pressure drop results are included to validate the smooth tube assumption.

4.1 Test tube designation and dimensions

The tubes are numbered sequentially and appended with letters C, U, or S. Each letter represents whether the tube is coated (C), uncoated (U), or scaled (S). For example 10C refers to tube 10, which is coated. Using this notation the relevant tube dimensions are summarized in table 4.1. The annulus of the heat exchanger has an inner diameter (d_4) of 33.55 mm, and the effective heat transfer length (L_{eff}) is 1981 mm.

4.2 Isothermal tests and energy balances

The steady state analysis (chapter 2) presumes negligible heat transfer from the heat exchanger to its surroundings. To ensure this assumption is met, the heat exchanger is thermally insulated. As stated in section 3.1, the heat exchanger material is selected such that it has a very low thermal conductivity. Furthermore the heat exchanger is wrapped with 15 mm polyethylene foam. To physically measure the heat transfer to

CHAPTER 4. EXPERIMENTAL TESTING

Table 4.1: Dimensions of test tubes

Tube	Outer diameter d_3 mm	Uncoated internal diameter d_2 mm	Coated internal diameter d_1 mm	Average coating thickness $(d_2-d_1)/2$ μm
10C	25.480	23.13	23.030	50
11C	25.360	23.17	22.909	130
12C	25.353	23.13	23.037	46
15C	25.340	23.12	23.032	44
16S	25.300	23.13	22.920	103

the surroundings, and thereby verify the adequacy of this insulation, isothermal tests are conducted.

These tests are performed using the calibration loop in figure 3.8 with the heaters switched off. To investigate whether the temperatures are actually constant during the isothermal test, the average temperature trend is measured. This involves calculating the temperature gradient at each sample time (2 s) using the previous six readings, and then averaging these values. The results are shown in table 4.2. The slightly positive trends indicate heat transfer to the working fluid. This heat transfer can result from conduction through the pump housings, originating from the electric motors driving the pumps. However the magnitude of these trends is negligibly small in comparison to accuracy of the temperature sensors.

Table 4.2: Average hot and cold temperature trends during isothermal tests

Tube	Hot temperature trend $^{\circ}\text{C}/\text{min}$	Cold temperature trend $^{\circ}\text{C}/\text{min}$
15U	0.14	0.14
10C	0.09	0.09
12C	0.13	0.13
15C	0.11	0.11

The arithmetic mean of the RTD sensors is denoted T_m . Table 4.3 shows the differences between T_m and the measured value from each RTD. The differences are less than ± 0.05 $^{\circ}\text{C}$, indicating the RTD sensors are calibrated to within the required tolerance.

The temperature difference between the hot and cold streams is directly measured using two thermopiles (as explained in section 3.2). These differences are denoted ΔT_h and ΔT_c for the hot and cold streams respectively. In addition the RTD probes indirectly measure these temperature differences, i.e. $T_{hi} - T_{co}$ and $T_{co} - T_{ci}$.

CHAPTER 4. EXPERIMENTAL TESTING

Table 4.3: Isothermal test deviations between absolute RTD reading and arithmetic mean

Tube	$T_{hi} - T_m$ K	$T_{ho} - T_m$ K	$T_{ci} - T_m$ K	$T_{co} - T_m$ K
15U	0.02	0.01	-0.02	-0.01
10C	0.03	0.01	-0.02	-0.01
12C	0.01	0.00	-0.01	0.00
15C	0.02	0.01	-0.02	-0.01

Comparison between these temperature differences measured using both types of sensors is shown in table 4.4. Again the temperature differences are smaller than the accuracy of the sensors, which means that heat losses to the surrounding have been sufficiently limited.

Table 4.4: Comparison of measured temperature differences using two different temperature sensor types

Tube	Thermopile		RTD	
	ΔT_h K	ΔT_c K	$T_{hi} - T_{ho}$ K	$T_{co} - T_{ci}$ K
15U	0.01	0.02	0.01	0.02
10C	-0.01	0.08	0.02	0.01
12C	0.04	-0.01	0.00	0.02
15C	0.02	0.02	0.02	0.02

Since the accuracy of the RTDs is comparable to the accuracy of the thermopiles, equal confidence can be given to the temperature difference measured using either the RTDs or thermopiles. The results from table 4.4 confirm this. However a significant reduction in the uncertainty of the temperature difference measurement can be achieved by averaging the measurements. Specifically the arithmetic mean is calculated between the temperature difference measured using the thermopiles, as well as the RTD probes. Therefore the averaged mean hot temperature difference is defined such that

$$\Delta \overline{T}_h = 0.5 (\Delta T_{\text{Thermopile}} + \Delta T_{\text{RTD}}) = 0.5 [\Delta T_h + (T_{hi} - T_{ho})] \quad (4.1)$$

and similarly the averaged mean cold temperature difference is

$$\Delta \overline{T}_c = 0.5 (\Delta T_{\text{Thermopile}} + \Delta T_{\text{RTD}}) = 0.5 [\Delta T_c + (T_{co} - T_{ci})] \quad (4.2)$$

During the isothermal testing, both flow meters are arranged in series. V_m denotes the arithmetic mean flow rate measured between the flow meters. As shown in table 4.5, the maximum percentage deviation in the measured flow rates and the

CHAPTER 4. EXPERIMENTAL TESTING

Table 4.5: Isothermal test deviations of flow rate measurement from arithmetic mean

Tube	$V_h - V_m$ %	$V_c - V_m$ %
15U	0.39	-0.39
10C	0.40	-0.40
12C	0.34	-0.34
15C	0.44	-0.44

average value is 0.44%. This is less than the flow meter accuracy, which is specified in the calibration certificate as $\pm 0.5\%$ of the actual reading (appendix E).

In spite of adequate insulation and calibrated flow meters, the calculated hot and cold stream heat transfer rates (equations (2.3) and (2.4) respectively) may be similar but not necessarily be identical. The discrepancy is caused by experimental error. However, the uncertainty associated with this error can be greatly reduced by taking the arithmetic mean of hot and cold stream heat transfer rates. The averaged mean heat transfer rate is then

$$Q_m = 0.5(m_h c_{ph} \Delta \overline{T}_h + m_c c_{pc} \Delta \overline{T}_c) \quad (4.3)$$

It is noted that the accuracy of the heat transfer calculated from the hot and cold streams is equal, in which case taking the arithmetic mean of these values is appropriate. This is not always the situation, particularly for other heat exchanger types, where measurements from one of the fluid streams has a larger uncertainty than the other.

The error between the measured hot and cold stream heat transfer rates is quantified by defining an energy balance EB , such that

$$EB = \frac{Q_c - Q_h}{\frac{1}{2}(Q_c + Q_h)} \quad (4.4)$$

Figure 4.1 shows that the energy balance errors are less than $\pm 1.8\%$. These values are comparable to similar heat transfer tests conducted by Dirker & Meyer (2005), who reported to have 90% of their energy balances less than 1%. In this case 90% of the values are less than 1.1%. The energy balance errors displayed in figure 4.1 appear equally positive and negative. This suggests that the energy balance errors are therefore dominated by random errors and not systematic errors. This highlights the inherent random uncertainty turbulent convection testing, and also means that the calibration is successful.

CHAPTER 4. EXPERIMENTAL TESTING

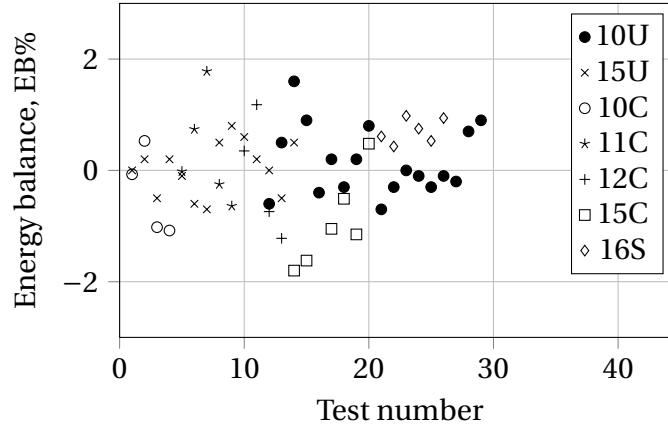


Figure 4.1: Energy balance of uncoated and coated tests

4.3 Uncoated tube tests to determine the outer convection coefficient

It is necessary to test the tubes before applying the coating, to determine the annular Nusselt number as a function of Reynolds number (see chapter 2). However, the measured data is first compared to two well known correlations to determine the accuracy of the data. Ensuing this, the regression analysis is used to predict the annular Nusselt numbers for use in the coated tests.

From equations (2.5) and (2.35), the annular convection Nusselt number is expressed as:

$$Nu_{ann} = \frac{d_4 - d_3}{k_{fh} \pi d_3 l_{eff}} \left[\frac{T_{hi} - T_{co} - (T_{ho} - T_{ci})}{Q_m \ln \left(\frac{T_{hi} - T_{co}}{T_{ho} - T_{ci}} \right)}, -\frac{1}{\pi l_{eff} k_{fc} h_c} - \frac{\ln \frac{d_3}{d_2}}{2\pi k_t l_{eff}} \right]^{-1} \quad (4.5)$$

The measured annular Nusselt numbers (Nu_{ann}) are compared to the calculated Nusselt number (Nu_{calc}), using two different correlations. The first is the Gnielinski correlation (Gnielinski, 2007) in figure 4.2 (a) and the second is the Dittus-Boelter correlation (Kröger, 1998) in figure 4.2 (b).

In figure 4.2 (a), the results are within $\pm 10\%$ of the calculated values. A similar level of scatter is observed in the data conducted by McMillen & Larson (1994), presented by Gnielinski (2007). They also performed tests using water as the working fluid, and had the same diameter ratio⁴. Their data showed a difference of approximately $\pm 12.5\%$ with the Gnielinski correlation.

⁴The annular convection coefficient depends on the diameter ratio because of the modified velocity profile (Dirker & Meyer, 2005)

CHAPTER 4. EXPERIMENTAL TESTING

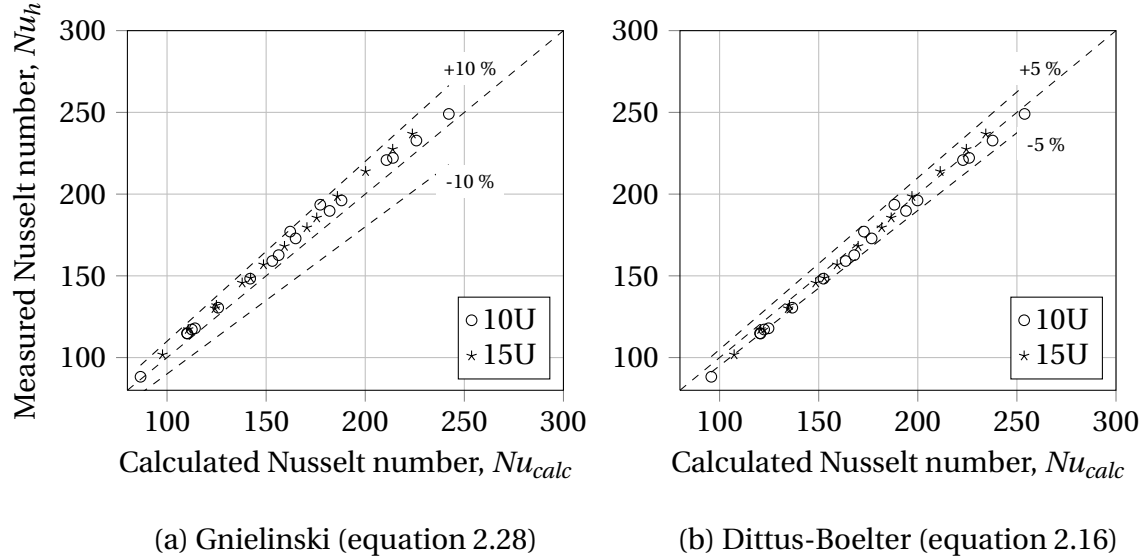


Figure 4.2: Measured Nusselt numbers compared to calculated values

There is even closer agreement in figure 4.2 (b) between the measured Nusselt number and the Dittus-Boelter correlation. The difference is less than $\pm 5\%$. This close agreement with two fully-developed flow correlations is sufficient to conclude that the design of the preconditioning annulus (section 3.1) is efficacious, and indeed fully-developed flow conditions are created within the test heat exchanger.

The similarity in the data between tests conducted on separate tubes 10U and 15U, indicates repeatability in the apparatus and testing procedures. Tubes 11C and 12C were already coated when supplied and therefore were not tested in the uncoated condition. Therefore the data from tubes 10U and 15U is also used to predict the annular Nusselt numbers of tubes 11C and 12C. A small uncertainty in the outer and inner tube diameter and tube conductivity is introduced by doing this, but this is accounted for by including these variables in equation (2.65).

Considering the Dittus-Boelter correlation (Kröger, 1998) in equation 2.16 and the Rabas & Cane (1983) correlation (equation 2.18), the annular Nusselt number can be written in the general form

$$Nu_{ann} = A_{Nu} Re_{ann}^{B_{Nu}} Pr_{ann}^{0.3} \quad (4.6)$$

where A_{Nu} and B_{Nu} are experimentally determined coefficients. Solving for these coefficients using the method of least squares results in the following:

$$10U: Nu_{ann} = (0.01496 \pm 0.0018) Re_{ann}^{(0.8530 \pm 0.0014)} Pr_{ann}^{0.3} \quad (4.7)$$

$$15U: Nu_{ann} = (0.01343 \pm 0.0017) Re_{ann}^{(0.8646 \pm 0.0014)} Pr_{ann}^{0.3} \quad (4.8)$$

The regression equations are applicable for

CHAPTER 4. EXPERIMENTAL TESTING

$$4000 \leq Re_{ann}^{0.8} Pr_{ann}^{0.3} \leq 9000$$

and are used for evaluating the annular Nusselt number in the coated tests.

4.4 Coated tube tests to determine the coating performance

The coating thermal performance is compared using three measures, as introduced in chapter 2. These measures are: the coating conductivity k_c (equation 2.37), the effective coated-tube conductivity k_{eff} (equation 2.40), and the coating factor R_c'' (equation 2.38). The subject of this thesis, involves determining these thermal performance measures for three coatings: A, B, and C.

4.4.1 Coating schedule

Shown in table 4.6, is the coating schedule of four cartridge brass tubes. Although cartridge brass is no longer used in most condensers, it is commercially available and a predecessor to admiralty brass. Admiralty brass differs from the cartridge brass (which is a 70-30 copper-zinc alloy), by the addition of 1% tin, 0.04% arsenic, as well as antimony and phosphorous (Putman, 2001). The small amounts of these alloying agents are used to increase its dezincification resistance, particularly in sea water conditions. The thermal conductivities of these tube materials differ by 8.1% (table 2.1), but this is accounted for in the analysis and it is within the expected variance from different tube suppliers. Also the relative testing before and after coating of the tube (10C and 15C), eliminates the tube conductivity from the calculation.

Table 4.6: Coating schedule of four test tubes

Coating	Tube numbers	Tube material	Thickness μm
A	10C	Cartridge brass	50
B	11C,15C	Cartridge brass	130,44
C	12C	Cartridge brass	46

It is noted from Table 4.6 that coating C is applied to both tubes 11C and 15C, albeit at two different thicknesses. The reason for this is twofold. Firstly, it allows the repeatability of the test procedure to be investigated. Secondly, the uncertainty in the coating conductivity is very sensitive to coating thickness. It is therefore necessary to test coating C (which will be shown to have a relatively high conductivity) at a greater thickness to reduce the uncertainty in the result.

CHAPTER 4. EXPERIMENTAL TESTING

4.4.2 The measured coating conductivity

The measured conductivity of the three coatings is illustrated in figure 4.3 in terms of the average heat transfer rate. In general the thermal conductivity of a material varies with temperature (Cengel & Ghajar, 2011). However in figure 4.3, the coating conductivity remains uniform in spite of increasing average heat transfer (and hence varying temperature). Obviously the conductivity-temperature dependence, over the temperature range 35 °C to 42 °C, is smaller than the uncertainty in these measurements. Therefore the temperature dependence is considered uniform in this range, and the arithmetic mean conductivity can be calculated.

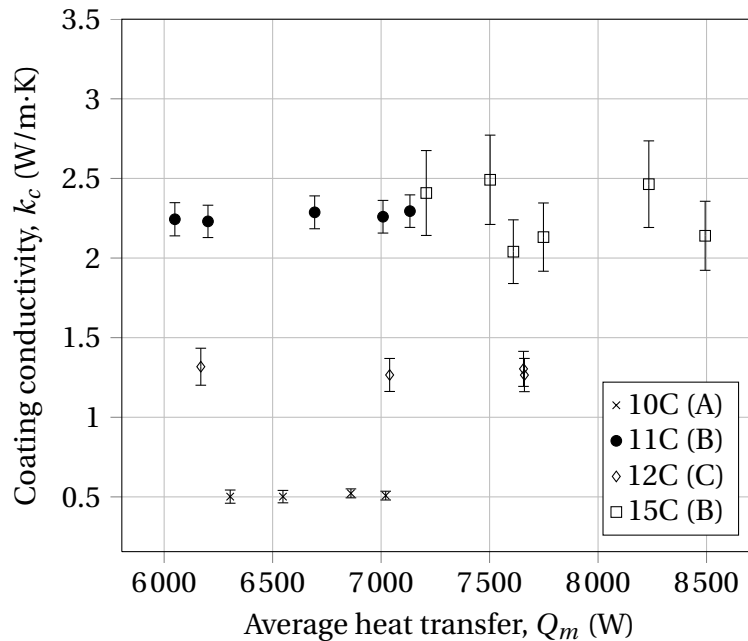


Figure 4.3: Measured coating thermal conductivity (coating in parentheses)

As described in chapter 2, the uncertainty in the measured conductivity consists of the random and systematic uncertainty estimates. The random uncertainty in the measured conductivity is directly calculated, using equations (2.57), (2.58), and (2.59). Table 4.7 shows the standard deviation of the measured conductivities ($s_{\bar{k}_c}$).

The systematic uncertainty is calculated from equation (2.71), using the systematic uncertainty component estimates shown in table 4.8. The estimates of the micrometer, vernier, and tape measure are based on the least count of these instruments, whereas the flow meter and temperature probes uncertainties are estimated using the manufacturers' quoted accuracy.

To investigate the relative contribution of each variable to the total uncertainty,

CHAPTER 4. EXPERIMENTAL TESTING

Table 4.7: Random uncertainty of the coating conductivity, s_{k_c}

Tube	Test 1	Test 2	Test 3	Test 4	Test 5
	W/m·K	W/m·K	W/m·K	W/m·K	W/m·K
10C	0.00025	0.00043	0.00088	0.00120	–
11C	0.00768	0.01037	0.01791	0.01028	0.00655
12C	0.01121	0.00503	0.00317	0.00556	–
15C	0.01846	0.01907	0.02414	0.00532	0.01509

Table 4.8: Systematic uncertainty component estimates (95% confidence level)

Source	Systematic uncertainty estimate $2b^\dagger$
Micrometer	0.001 mm
Internal vernier	0.01 mm
Tape measure	1 mm
Pt 100 RTD	0.05 °C
Flow meter	0.5% of actual reading
Thermopile	0.05 °C
Tube conductivity	10 W/m·K

†: Refers to 1.96σ for 95% confidence level

it is necessary to consult figure 4.4. The uncertainty magnification factors (UMFs) of the measured variables in the data reduction equation (2.37) are compared. The coated internal diameter d_1 , has the highest UMF and is greater than one, which means its uncertainty magnifies significantly as it propagates through the data reduction equation. Since the internal coated diameter has the largest UMF, and is a function of coating thickness, the measured thermal conductivity is most sensitive to the coating thickness.

It is inherently difficult to accurately measure the coating thickness on these small diameter tubes. The problem is exacerbated by very thin coatings, which cause traditional eddy current, or ultrasonic measurements to be unreliable. The most repeatable and accurate method, was found to be a mass measurement. This involves measuring the mass of coating before application. The volume, and hence thickness, is determined using the density of the coating. Density values are obtained from the manufacturer's specification sheet, and are verified by checking the mass of a finite volume. This method has been checked by destructive testing on other tubes, where the tube is sectioned and analyzed under a microscope. The results indicate approximately a 5 μm difference between the two techniques. Thus the mass-measurement method is confidently used to determine the coating thickness.

Figure 4.4 also shows that the magnification factor of the internal diameter d_1 ,

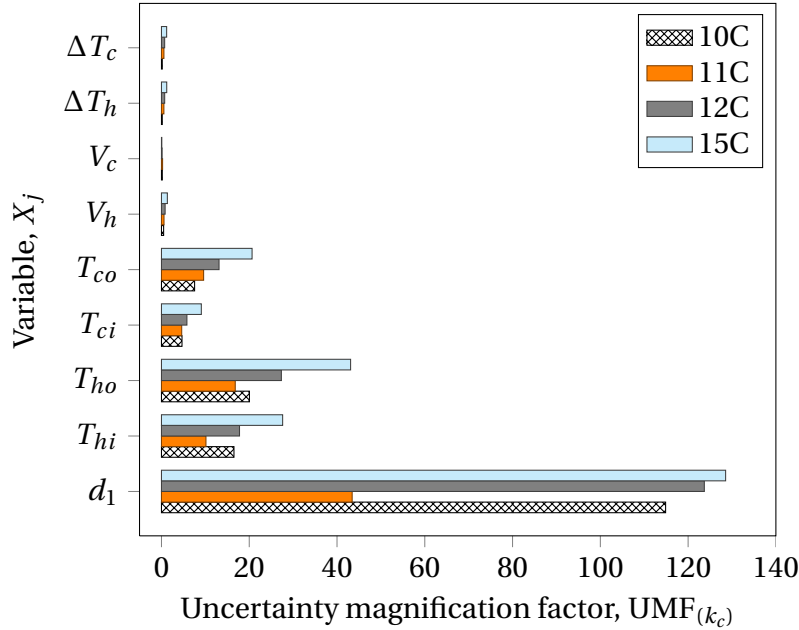


Figure 4.4: Uncertainty magnification factors in the thermal conductivity reduction equation (2.37)

of tube 11C is considerably smaller than those of the other three tubes. The only difference between tubes 11C and 15C is their coating thickness. In fact, the coating thickness of tube 11C is nearly three times larger than any of the other thicknesses. Therefore increasing the coating thickness causes a reduction in the UMF. However, from equation (2.56) the UMF is proportional to $\partial k_c / \partial d_1$. This explains the sensitivity of the uncertainty with coating thickness. The relative difference in the uncertainty between tube 11C (150 μm) and tube 15C (44 μm) in figure 4.3 is apparent.

The hot stream temperatures (T_{hi} and T_{ho}) and to a lesser extent, the cold stream temperatures (T_{ci} and T_{co}), also have large UMFs (figure 4.4). This means the uncertainties in the temperature measurements also magnify as they propagate through the data reduction equation. Thus, a high level of accuracy in temperature measurement is required in such experiments, particularly concerning the temperature difference measurements.

As was previously noted, the thermopiles are chosen to directly measure the temperature differences. Indirectly, the high accuracy RTD probes are also used to measure these differences. Finally the mean temperature differences between each thermopile and RTD pair, are averaged to further reduce the uncertainty.

The importance of properly accounting for the correlated uncertainties, is also illustrated in figure 4.5. Particularly the mean contribution from the correlation terms $CORR2$ and $CORR5$ are negative. These correlation terms account for the fact that the

same instruments are used in the uncoated and coated tests. Since the systematic uncertainties of each instrument remain constant, effectively these terms reduce the uncertainty. Correlation terms $CORR3$ and $CORR4$ are positive, but they are smaller than terms $CORR2$ and $CORR5$. Therefore, the total contribution from all the correlation terms is negative. This shows that the approach of testing the uncoated tube and then the coated tube is successful in reducing the overall uncertainty in the coating conductivity.

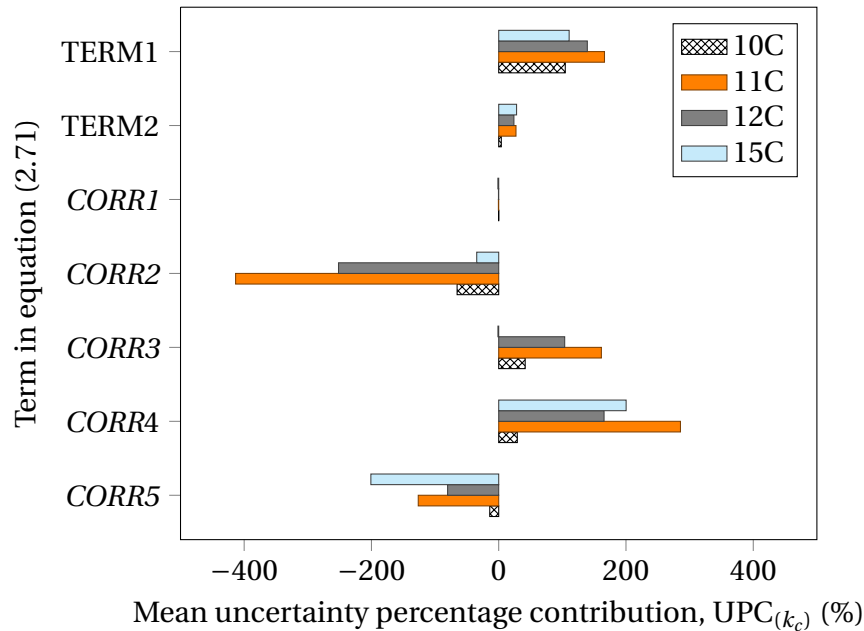


Figure 4.5: Relative systematic uncertainty contributions from each term in equation (2.71)

In summary, the annular convection Nusselt number is determined as a function of Reynolds number, using uncoated test data. As a result of this, the uncertainty in the measured conductivity is decreased as a result of correlated uncertainties between the uncoated and coated tests. In fact although back-to-back testing is conducted with exactly the same equipment, the systematic uncertainties cannot simply be ignored. Coleman & Steele (2009) address this issue in the general sense and similarly conclude that in general the systematic uncertainties do not cancel.

These three coatings are compared in terms of their arithmetic mean thermal conductivity in figure 4.6. The result from similar tests conducted by Honing & Kröger (2006) is also shown and labeled coating D. Coating B has the best performance in terms of the measured conductivity, equal to 2.27 ± 0.25 W/m·K. Coating C has the second best performance with a conductivity equal to 1.29 ± 0.11 W/m·K. Coating A has the lowest conductivity equal to 0.51 ± 0.03 W/m·K. Coating D has a comparable conductivity equal to 0.66 W/m·K.

CHAPTER 4. EXPERIMENTAL TESTING

The average coating conductivity of coating B measured on tube 11C is 2.31 W/m·K, whereas the conductivity of coating B applied to tube 15C is 2.23 W/m·K. This represents a 3.5% difference between the measured conductivity of the same coating tested on two separate tubes. As this difference is well within the uncertainty levels, the results are deemed repeatable.

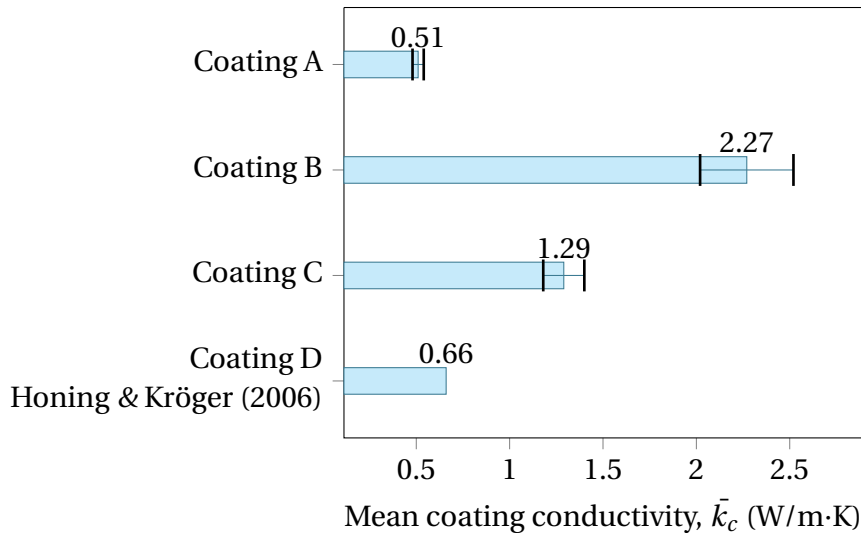


Figure 4.6: Average thermal conductivity comparison of coatings

4.4.3 The effective coated-tube conductivity

Figure 4.7 compares the average effective coated-tube conductivity \bar{k}_{eff} , determined using equation (2.40). Consider the coatings applied to tubes 10C, 12C, and 15C which have the same nominal coating thickness. Tube 10C has the lowest effective conductivity equal to 11.3 ± 1.3 W/m·K. Tube 12C has an effective conductivity 27.2 ± 1.2 W/m·K. And tube 15C has the largest conductivity, equal to 46.9 ± 3.2 W/m·K. By increasing the coating thickness of coating B to 130 μm , tube 11C has an effective conductivity equal to 19.3 ± 1.3 W/m·K. This highlights an inherent danger of misinterpreting the effective coated-tube conductivity results if the coating thicknesses are not taken into account.

Effective coated-tube conductivity is an extensive property which depends on the coating thickness, whereas the coating conductivity is an intensive property. This means that any specifications referring to coating limits, that are written in terms of effective coated-tube conductivity, need to also specify the tube material and size, as well as the nominal coating thickness.

This is also true for the coating factor shown in figure 4.7. The inverse relation-

ship between the effective conductivity and coating factor is evident, whereby a low effective conductivity results in a large coating factor. All three coating factors of tubes 10C, 12C, and 15C range from $9.8 \times 10^{-5} \text{ m}^2 \text{ W/K}$ to $3.6 \times 10^{-5} \text{ m}^2 \text{ W/K}$. Field testing performed by Sato, Nosetani & Hotta (1985) resulted in a coating factor of $3.2 \times 10^{-5} \text{ m}^2 \text{ W/K}$ for APCs with an average thickness of $22 \mu\text{m}$. Despite the fact that their tests were conducted on thinner coatings, the results are still comparable to those presented here. In fact, since these coatings are thicker, their performance is better than the ones tested by Sato, Nosetani & Hotta (1985).

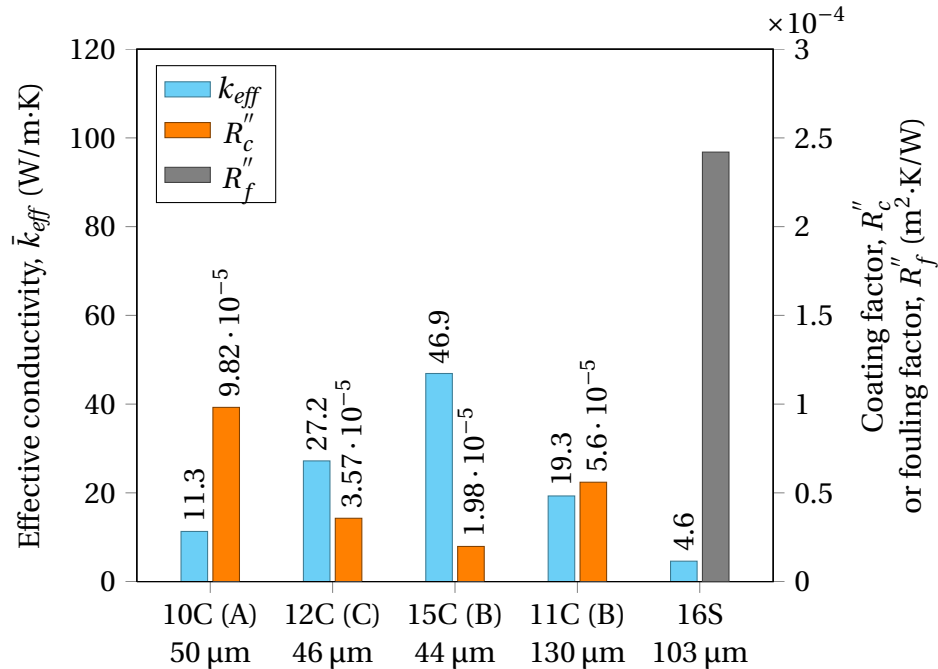


Figure 4.7: Average effective conductivity and coating factor of three coatings (coating letter in parentheses) and one scaled tube

The scaled tube 16S in figure 4.7 has a fouling factor which is equal to 2.5×10^{-4} . Obviously the fouling factor varies considerably with thickness, porosity and deposit type. However, the fouling factor from the scaled tube 16S represents the actual operating conditions experienced by an in-service condenser, which has subsequently been coated.

The uncertainty in the effective coated-tube follows the same method discussed in determining the coating conductivity. In this case the standard deviations of the measured effective coated-tube conductivities are shown in table 4.9

As seen in table 4.10, the UMF of d_1 in the effective coated-tube conductivity is nearly an order of magnitude smaller than the UMF in the coating conductivity. This is because the effective coated-tube does not directly rely on the intermediate diam-

CHAPTER 4. EXPERIMENTAL TESTING

Table 4.9: Random uncertainty of the effective coated-tube, $s_{k_{eff}}$

Tube	Test 1	Test 2	Test 3	Test 4	Test 5
	W/m·K	W/m·K	W/m·K	W/m·K	W/m·K
10C	0.005	0.008	0.019	0.026	0.000
11C	0.058	0.082	0.140	0.076	0.051
12C	0.212	0.089	0.062	0.106	0.061
15C	0.321	0.323	0.414	0.098	0.285

eter, d_2 . In fact the uncoated diameter is only necessary in determining the annular Nusselt number during the uncoated tests.

Table 4.10: Sensitivity of k_c with d_1 compared to sensitivity of k_{eff} with d_1

Tube	Sensitivity of k_c with d_1	Sensitivity of k_{eff} with d_1
	$\frac{\partial k_c}{\partial d_1}$	$\frac{\partial k_{eff}}{\partial d_1}$
	W/m·K/m	W/m·K/m
10C	114.9	4.400
11C	43.45	4.055
12C	123.7	3.978
15C	128.5	2.880

4.5 Pressure drop results

Throughout the analysis presented thus far, it has been assumed that the tube surface profile is smooth. New tubes are drawn in the manufacturing process and therefore are inherently smooth. However, this assumption is verified by measuring the pressure drop along the length of the tube.

Table 4.11 shows the length between the pressure tappings for the different tubes. The nominal length is 2.6 m, and an entrance length of approximately 27 diameters is provided before the upstream tapping point.

The measured friction factors are plotted on the log axis of figure 4.8. Comparison is made to equation (2.13). The data presented in figure 4.8 shows a deviation from

Table 4.11: Length between pressure tappings for the various tubes

Tube	$L_{\Delta p}$
	m
11C	2.608
12C	2.643
15C	2.598

CHAPTER 4. EXPERIMENTAL TESTING

equation 2.13 which is smaller than $\pm 5\%$. Comparatively all of the coatings tested exhibit the same friction factor as the smooth tube correlation. This validates the use of equation 2.13 in the determination of the inner convection coefficient. The mea-

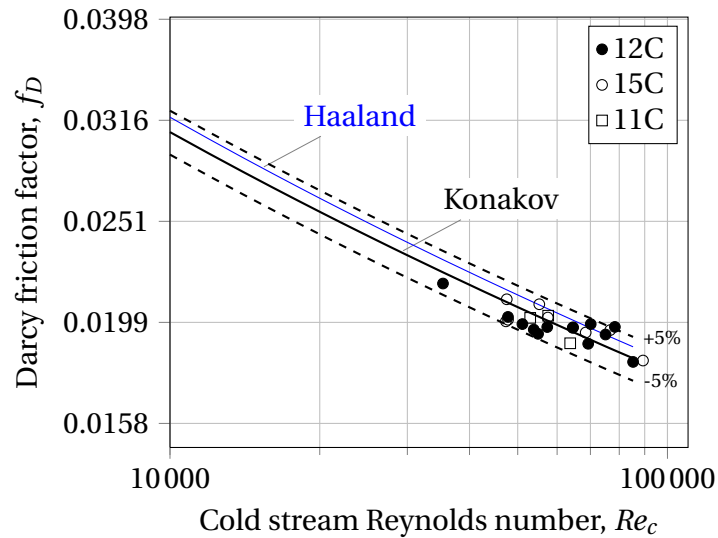


Figure 4.8: Measured friction factor versus Reynolds number

sured friction factors are also compared to the equation proposed by Haaland (1983) (equation 2.14) with the surface roughness ϕ , equal to $1.5 \mu\text{m}$ (Incropera, Dewitt, Bergman & Lavine, 2007).

Chapter 5

Coated condenser modeling

Overview

The relative effect on the condenser performance caused by artificial protective coatings (APCs) is investigated in this chapter. Starting with the Heat Exchange Institute (HEI) standards for steam surface condensers (Heat Exchange Institute, 2012), the performance of an uncoated condenser with realistic design specifications is predicted. Thereafter the thermal resistance method (from chapter 2) is used to separate the steam-side effects from the overall heat transfer coefficient predicted by the HEI standard. This allows the relative change after coating to be determined in terms of two measures: the number of heat transfer units (NTU) and the cleanliness factor. The sensitivity of these measures with respect to coating conductivity and thickness is then explored. Further analysis leads to the resultant change in steam temperature, which together with industry rules of thumb and actual turbine data, yields the change in power plant efficiency. Consolidating these results, the methodology for determining selection criteria of APCs are suggested.

5.1 The HEI method of analysis

The HEI standard assists purchasers in determining the viability of different condenser designs. The designer must ensure that the condenser is fabricated such that it achieves the same heat transfer rate as stipulated by the standard. The HEI method involves determining the overall heat transfer coefficient from empirical data.

This data is obtained from calorimetric experimentation using 1-inch 18 BWG Admiralty brass tubing, with an inlet water temperature equal to 21.1 °C (70 °F). Although, correction factors are given for different temperatures and tube materials. Together with experimental testing, the data is correlated with field tests to increase the accuracy thereof. From this data, the overall heat transfer coefficients for differ-

CHAPTER 5. COATED CONDENSER MODELING

ent tube sizes are tabulated and plotted in terms of water velocity in table 1 and figure 1 of the standard (Heat Exchange Institute, 2012). This is termed the uncorrected heat transfer coefficient, U_1 .

The corrected heat transfer coefficient is then given by

$$U_{\text{HEI}} = U_1 \times F_W \times F_M \times F_C \quad (5.1)$$

where F_W is the inlet water temperature correction factor and F_M is the material correction factor. These are necessary to determine the performance of other tube types and different cooling-water inlet temperatures. The cleanliness factor F_C is chosen by the purchaser; this factor accounts for fouling and other performance deficiencies during normal operation. The HEI method is illustrated by means of a sample calculation in appendix D.

It must be stated that the corrected overall heat transfer coefficient U_{HEI} , is applicable to tube bundles. The HEI standard (Heat Exchange Institute, 2012) states that this coefficient is not meant to be used by designers as a single tube heat transfer coefficient. This is because the corrected heat transfer coefficient takes into account operational aspects which cause the difference between the theoretical single-tube values, and the bundle values actually encountered in service. This is confirmed by the Electrical Power Research Institute (EPRI) (1987).

In order to make predictions regarding the effect on performance with respect to APCs, it is necessary to extract the steam-side effects from the HEI predicted overall heat transfer coefficient. This is achieved by using the thermal resistance method.

5.2 Thermal resistance method

5.2.1 Motivation for using the thermal resistance method

Although the HEI method gives a satisfactory estimate of condenser performance, it makes no provision for APCs. Therefore a model is developed based on the thermal resistance method of analysis, which individually considers the thermal resistances from the cooling-water convection, conduction through the tube wall and coating, and steam-side convection. These resistances are analogous to those shown in figure 2.4 from chapter 2 for a single tube.

This model is written in terms of the steam vapor velocity, which is generally unknown, as it varies through the condenser. However a mean value is found by iteratively equating the overall heat transfer coefficient to the value calculated using the HEI method. Thereafter this model is used to parametrically study the relative change in performance caused by APCs.

This method of analysis therefore includes the expected steam-side convection coefficient, as encountered in service, rather than single-tube values (which are typi-

CHAPTER 5. COATED CONDENSER MODELING

cally higher). A realistic indication of the relative influence of APCs is achieved in this way. Much of the theory presented in chapter 2 is applicable. However, treatment of the outer convection coefficient due to the condensing steam requires special attention.

5.2.2 Condensation onto horizontal tube bundles

Condensation onto a surface can occur either by drop-wise or film-wise mechanisms. Drop-wise condensation occurs when the surface has poor wetting properties and the condensate forms droplets which fall from the surface. Film-wise condensation is characterized by the condensate wetting the surface and forming a film, which slides off the surface in an almost sheet-like manner. Drop-wise condensation generally results in a larger convection coefficient, which can be up to 10 times that of film-wise condensation (Cengel & Ghajar, 2011). Film-wise condensation is however most commonly encountered in steam surface condensers (Putman, 2001) and will be the sole focus hereafter.

The film structure on a single tube is shown in figure 5.1 (a). The vapor is cooled below its saturation temperature as it comes into contact with the outer tube surface. Latent heat of vaporization is removed, which causes the vapor to change phase and condense. The liquid-condensate film then flows around the periphery of the tube, growing in thickness and ultimately falls from the surface.

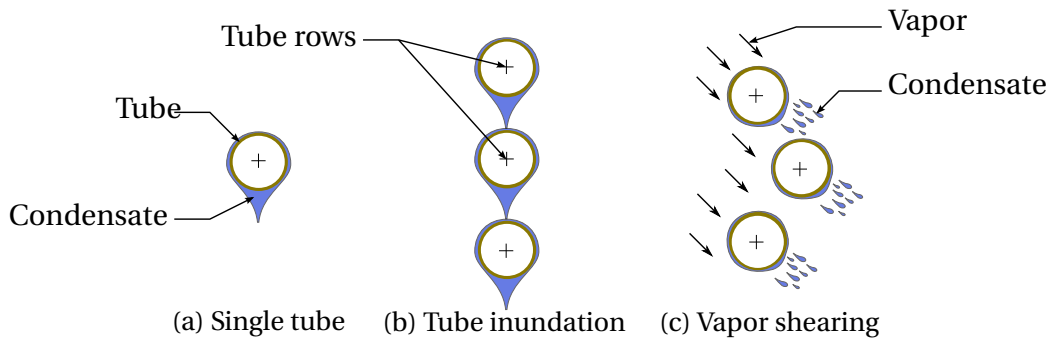


Figure 5.1: Modes of condensation

In condenser tube bundles there are three additional aspects affecting the condensation: tube inundation, vapor shearing, and the presence of non-condensable gases. Tube inundation occurs when falling condensate from vertical tube rows impacts lower tubes (figure 5.1 b) and causes flooding of these tubes. This decreases the heat transfer rate. Vapor shearing is shown in figure 5.1 (c), and involves a thinning of the condensate film caused by the flowing vapor. This process increases the rate of heat transfer because the thinner condensate film has less thermal resistance. Lastly

CHAPTER 5. COATED CONDENSER MODELING

small quantities of non-condensable gases are present (in spite of venting equipment) and impede heat transfer.

Non-condensable gases inevitably accumulate in plant condensers, typically at the coldest region of the condenser. They enter the steam system from equipment interface leaks and also from the boiler feed water, where small amounts of gases are dissolved. Silver (1963) commented that an amount of non-condensable gases as small as 1% by weight can have a significant effect on the overall heat transfer.

Figure 5.2 shows the effect of non-condensable gases (typically air) on the condensation process occurring on the outside of the tube. As the gas-vapor mixture comes into contact with the condenser tube, the steam condenses leaving behind the non-condensable gas. This causes a higher concentration of non-condensable gas around the condensate film. The concentration difference causes diffusion of the non-condensable gas to occur away from the condensate-vapor interface. Conversely the steam vapor has to diffuse towards the condensate-vapor interface. The partial pressure of the steam (and hence saturation temperature) at the condensate-vapor interface is therefore decreased. The smaller temperature difference across the condensate film reduces the heat transfer rate. Hence the presence of non-condensable gases act as a thermal resistance to heat transfer.

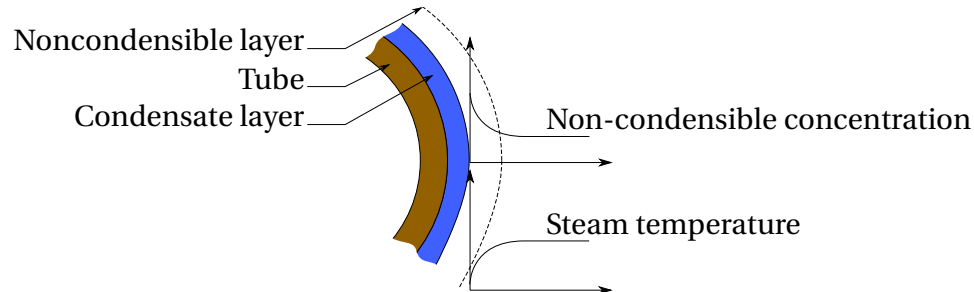


Figure 5.2: Condensation of steam in the presence of non-condensable gases

5.2.3 Condensation correlations

The convection coefficient associated with condensation of a fluid onto an isothermal horizontal tube was first investigated by Nusselt (1916), as cited by Silver (1963), who showed that the appropriate convection coefficient is

$$h_g = 0.68 \left[\frac{g \rho_{con}^2 i_{fg} k_{con}^3}{\mu_{con} d_3 (T_s - T_w)} \right]^{1/4} \quad (5.2)$$

where $(T_s - T_w)$ is the temperature difference across the condensate film. T_s is the steam (vapor) temperature and T_w is the wall temperature. The subscript *con* refers

CHAPTER 5. COATED CONDENSER MODELING

to the condensate properties evaluated at the mean film temperature, i.e. $0.5 \times (T_s + T_w)$.

Kröger (1998) extends Nusselt's analysis to find

$$h_g = 0.728 \left[\frac{g \rho_{con}^2 i_{fg} k_l^3}{\mu_{con} d_3 (T_s - T_w)} \right]^{1/4} \quad (5.3)$$

The effect of sub-cooling, where the condensate is cooled below the saturation temperature, is accounted for by using the modified enthalpy of formation i_{fg}^* (Cengel & Ghajar, 2011), which is given by

$$i_{fg}^* = i_{fg} + 0.68 c_{p,l} (T_s - T_w) \quad (5.4)$$

Butterworth (1981), cited by Hiroshi (2011), suggested that the overall heat transfer coefficient describing the condensation within a tube bundle is a function of the gravity-based coefficient h_g , and the vapor shear controlled coefficient h_{sh} . Specifically the mean convection coefficient \bar{h} , for n tube rows is

$$\bar{h} = n^{-0.16} \left[\frac{1}{2} h_{sh}^2 + \left(\frac{1}{4} h_{sh}^4 + h_g^4 \right)^{\frac{1}{2}} \right]^{\frac{1}{2}} \quad (5.5)$$

where the gravity controlled convection term h_g , is given by the single tube correlation (equation 5.3) and the shear component is given by

$$h_{sh} = \frac{k_f}{d_3} \cdot 0.59 \left(\rho_l \frac{d_3}{\psi \mu_l} v_\infty \right)^{0.5} \quad (5.6)$$

v_∞ is defined to be the vapor velocity based on the maximum flow area (i.e. in the absence of any tube). ψ is the void fraction of the bundle which is calculated as the free volume divided by the total volume of the bundle.

The resistance caused by the presence of the non-condensable gas can be determined from the following approximate equation given by Rose (1980), cited by Tarrad & Majeed (2010):

$$\frac{1}{R_a} = a \frac{D_{as}}{d_3} Re_{mix}^{0.5} \left(\frac{p_{mix} - p_s}{p_{mix}} \right)^{-b} p_{mix}^{1/3} \left(\frac{\rho_s i_{fg}^*}{T_s} \right)^{2/3} \frac{1}{T_s - T_{lv}}^{1/3} \quad (5.7)$$

where a and b are

$$(a, b) = \begin{cases} (0.82, 0.6), & Re_{mix} \leq 350 \\ (0.52, 0.7), & Re_{mix} > 350 \end{cases}$$

CHAPTER 5. COATED CONDENSER MODELING

In the above-mentioned equation T_{lv} is the liquid-vapor interface temperature. Note that noncondensable gases mean that T_s is replaced by T_{lv} in equations (5.3) and (5.4). D_{as} is the diffusion coefficient for air in steam calculated from experimental data. Marrero & Manson (1972), cited by Cengel & Ghajar (2011), determine this coefficient according to

$$D_{as} = 1.87 \times 10^{-10} \frac{(T_s)^{2.072}}{p_{mix}} \quad (5.8)$$

The Reynolds number of the mixture Re_{mix} , is defined in terms of the outer tube diameter d_3

$$Re_{mix} = \frac{\rho_{mix} v_{\infty} d_3}{\mu_{mix}} \quad (5.9)$$

Equation (5.7) shows how the resistance caused by the presence of the non-condensable gases depends on the vapor velocity. Silver (1963) commented on the danger of low vapor velocities, which lead to a severe decrease in heat transfer, as a result of the increased non-condensable gas concentration around the tube.

The mixture pressure is calculated from the vapor partial pressure using the ideal gas law, which means

$$p_{mix} = \left(1 + 0.622 \frac{w}{1-w}\right) p_s \quad (5.10)$$

where w is the air-steam mass fraction

$$w = \frac{m_a}{m_s + m_a} \quad (5.11)$$

5.2.4 Thermal resistance model

Consider defining a mean overall heat transfer coefficient \bar{U} for the whole condenser, which is based on the outer surface area of the tube bundles, namely A_o . Then the total heat transfer of the condenser is

$$Q_{duty} = \bar{U} A_o \Delta T_{lm} \quad (5.12)$$

The log mean temperature is defined to be

$$\Delta T_{lm} = \frac{T_{co} - T_{ci}}{\ln \frac{T_s - T_{ci}}{T_s - T_{co}}} \quad (5.13)$$

where T_s is the average steam temperature (i.e. the approaching steam temperature at the turbine neck). Using the mean steam-side convection coefficient \bar{h} (defined by

CHAPTER 5. COATED CONDENSER MODELING

equation 5.5), the mean overall heat transfer coefficient is

$$\bar{U} = \left(R_a + \frac{1}{h} + \frac{\ln \frac{d_3}{d_1}}{2k_{eff} \frac{1}{d_3}} + \frac{1}{h_i \frac{d_2}{d_3}} \right)^{-1} \quad (5.14)$$

where R_a is the thermal resistance across the condensate-vapor interface, which results from the presence of non-condensable gases.

The condensation correlations presented thus far refer to constant tube wall temperatures. However, in a condenser the temperature difference driving the condensation is larger at the inlet than at the outlet. This means that the condensate film will generally be thicker at the tube inlet than at the tube outlet.

This represents an intermediate situation between two idealized conditions: constant heat flux or constant wall temperature. As a result, the local convection coefficient and hence the surface temperature of the tube will vary along the length of the tube. Silver (1963) re-writes the convection coefficient in terms of condensation rate and integrates this expression along the length of the tube (as shown in appendix C). The mean condensation rate is used to then determine the mean convection coefficient. Putman (2001) uses the isothermal tube correlations with an average wall temperature T_w . This is determined using an iterative procedure, by solving

$$\frac{T_{lv} - T_w}{T_{lv} - T_b} = \frac{\bar{U}}{\bar{h}} \quad (5.15)$$

where T_{lv} is the mean condensate-vapor interface temperature and T_b is the bulk cooling water temperature

$$T_b = 0.5 \times (T_{ci} + T_{co}) \quad (5.16)$$

Similarly T_{lv} is iteratively solved by equating

$$\frac{T_s - T_{lv}}{T_s - T_b} = R_a \bar{U} \quad (5.17)$$

In a condenser the vapor velocity near the top row of tubes is not equal to that near tubes in the center of the tube bundle. The pressure drop experienced by the vapor causes this variation in vapor velocity. The effect of the vapor pressure drop can be included by defining a mean vapor velocity for the whole compartment, in which case the mean vapor velocity v^+ , is defined to be

$$v^+ = \gamma v_\infty \quad (5.18)$$

where the function γ is determined by equating

$$U_{HEI} = \bar{U} \quad (5.19)$$

CHAPTER 5. COATED CONDENSER MODELING

The vapor velocity is governed by the mechanisms of two phase flow. In addition to the physical geometry, the condition of the approaching steam (at the turbine neck) will affect the vapor velocity. Similarly the cooling water flow rate will dictate the rate of condensation. Bearing these physical arguments in mind, assume that the function γ can be described by a function that depends on the following variables:

$$\gamma \approx f^{cn}(\Delta T_{LM}, u_{\infty}, m_w c_{pw}, p_{mix}, TTD)$$

TTD is the terminal temperature difference ($T_s - T_{co}$).

For the purposes of this parametric study it is required to investigate the relative effect of coating the internal surface of the condenser tubes. Representative condenser geometry and operating conditions are given in appendix C. Using these parameters, the resulting multivariate regression is

$$\gamma = b_0 + b_1 \Delta T_{LM} + b_2 u_{\infty} + b_3 m_w c_{pw} + b_4 p_{mix} + b_5 TTD + b_6 w \quad (5.20)$$

where the regression coefficients are shown in table 5.1 and the sample calculation is given in appendix D. Some of the calculated values of γ are appended in table

Table 5.1: γ regression coefficients in equation (5.20)

b_0	b_1	b_2	b_3	b_4	b_5
8.5430	-0.7860	-0.11084	0.1263×10^{-3}	0.3161×10^{-3}	0.4744

C.2 (appendix C) and all of these values are less than one. In fact, the mean value is approximately 0.64, which shows that using the single-tube correlation equation (5.3) alone would over estimate the overall heat transfer coefficient.

This concludes the thermal resistance model. Before parameterizing the APCs, the model is verified against the HEI prediction to determine its goodness of fit.

5.2.5 Verifying the uncoated model with the HEI coefficient

Using the modeling parameters given in appendix C, the overall mean heat transfer coefficients are compared in figure 5.3. The similarity between the model and HEI values indicates that the regression fit of γ is successful. Only minor deviations are evident for the Admiralty brass values at the extremal velocities. The magnitude of the maximum deviation is 1.6%, which is negligibly small in comparison to the inherent uncertainty in condenser modeling.

Although this one-dimensional modeling is suited for the current study of the changes in relative performance caused by APCs, it can be extended to a two-dimensional model. Tarrad & Majeed (2010) use a similar approach as followed here, except they discretize the condenser along each row and solve for the vapor velocity by calculating the pressure drop. Good agreement was found with field data using this two-dimensional model technique (Tarrad & Majeed, 2010).

CHAPTER 5. COATED CONDENSER MODELING

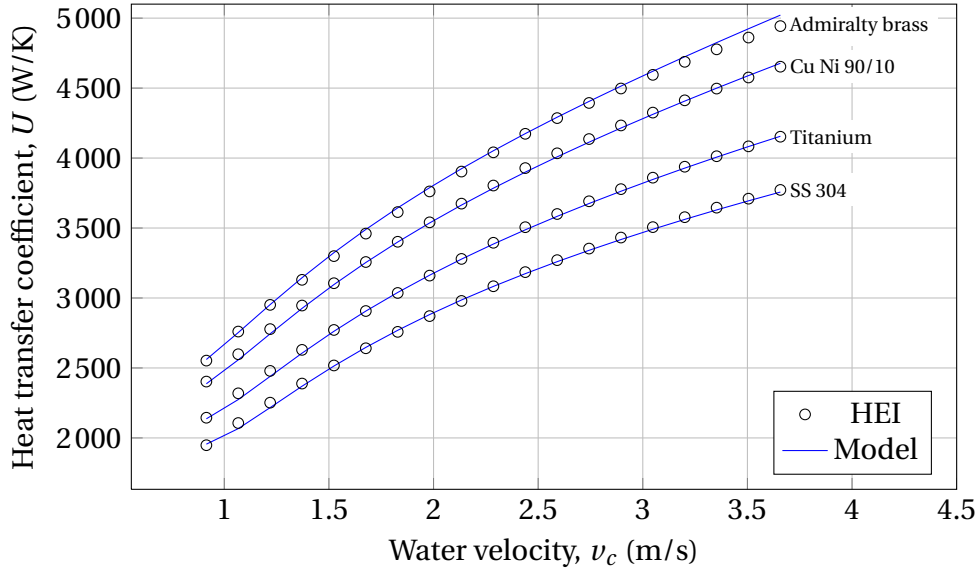


Figure 5.3: Model predicted coefficient versus HEI values as a function of velocity

Having verified the thermal resistance model is suitably developed it can be used to parametrically study the relative affect of APCs as detailed below.

5.3 Results of the parametric study

The results of the parametric study are focused on the overall effect on performance of the model condenser, caused by the application of APCs. Two measures are used: the first is a pseudo cleanliness factor CF , and the second is the number of transfer units NTU .

The cleanliness factor in this instance is defined to be

$$CF = \frac{(UA)_{\text{coated}}}{(UA)_{\text{uncoated}}} \quad (5.21)$$

which is analogous to the HEI defined cleanliness factor

$$F_c = \frac{Q/\Delta T_{lm}}{U_{HEI} A_s} = \frac{(UA)_{\text{operating}}}{(UA)_{HEI}} \quad (5.22)$$

The NTU is defined to be

$$NTU = \frac{UA}{m_c c_p} \quad (5.23)$$

In fact, the CF and NTU are simply related by

$$\frac{NTU}{NTU_{\text{uncoated}}} = CF \left(\frac{m_{w,\text{uncoated}}}{m_w} \right) \quad (5.24)$$

CHAPTER 5. COATED CONDENSER MODELING

Consider applying a fixed coating thickness of 50 μm to the model condenser and varying the coating conductivity. The steam temperature is then determined using the model condenser, whilst keeping the total heat transfer rate constant. The change in the NTU ratio with effective coated-tube conductivity ratio is presented in figure 5.4.

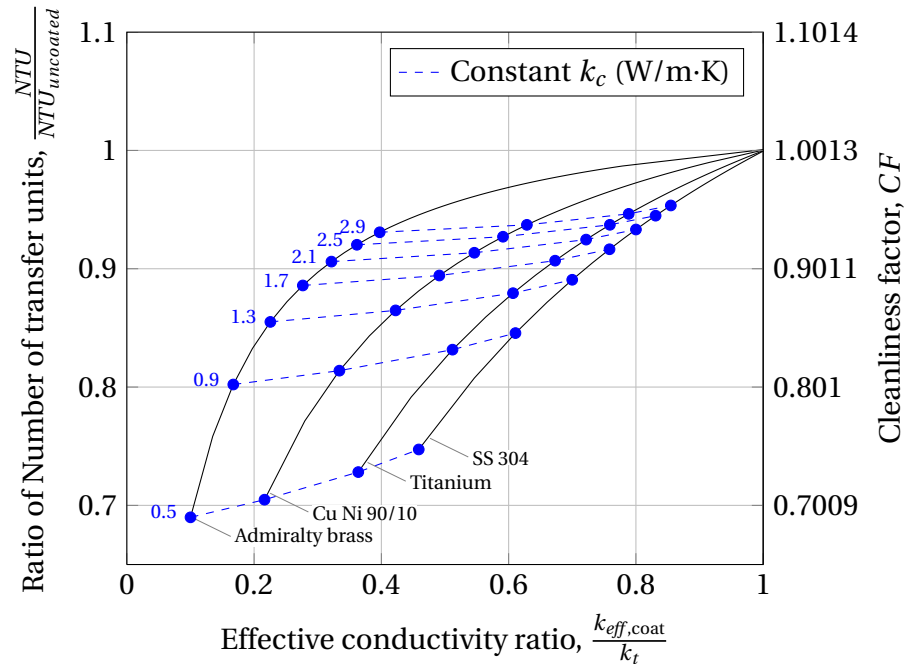


Figure 5.4: NTU versus effective coated-tube conductivity ratio for different tube materials (18 BWG 1-inch tubing)

Four tube materials are shown in figure 5.4: Admiralty brass, copper-nickel alloy (Cu Ni 90/10), titanium, and grade 304 stainless steel. Each tube shows that the NTU ratio decreases non-linearly with decreasing effective conductivity. The non-linear nature of this trend results from the logarithm in the conduction resistance term.

The cleanliness factor CF is approximately equal to the normalized NTU , as shown by the comparing the ordinates. Referring to equation (5.24), the similarity between CF and NTU ratio is explained by the marginal difference (0.13%) between the coated and uncoated mass flow rates (for a coating thickness of 50 μm). Note that the pumping power is fixed in this parametric study⁵. Therefore the reduction in internal diameter as a result of large coating thicknesses will change the cooling water flow rate. However, the maximum thickness tested in this study (150 μm) only causes a 0.39%

⁵In existing plants the pump is generally fixed (i.e. the pumping power is a function of the flow rate) and for smaller tube sizes this may be significant.

CHAPTER 5. COATED CONDENSER MODELING

reduction in the mass flow rate.

The NTU is very sensitive to coating conductivity as well as coating thickness. Figure 5.5 confirms this statement, where the cleanliness factor is plotted as a function of coating thickness. The results from tubes 10C, 12C, and 15C (given in chapter 4) are also plotted alongside the results from Horn & Mitchell (2005).

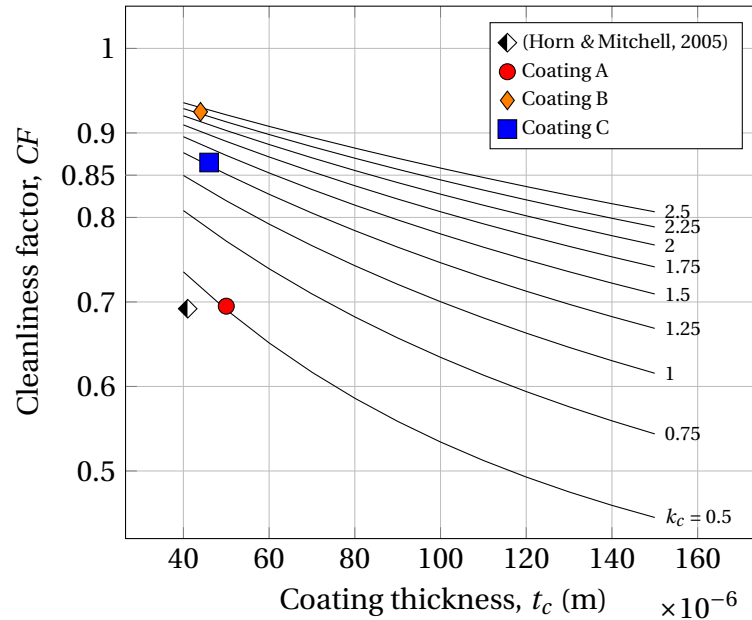


Figure 5.5: Variation in CF with coating thickness and conductivity (Admiralty brass 18 BWG 1-inch tubing)

Importantly coating criteria may be deduced from figure 5.5 for coatings applied to 1-inch 18 BWG Admiralty brass tubing. Fraze & Woodruff (1997) found that typical enhanced coatings designed for this application had cleanliness factors equal to 0.85. Therefore, if the average coating thickness is limited to $50 \mu\text{m}$, a minimum conductivity of $1.2 \text{ W/m}\cdot\text{K}$ is required to achieve this level of cleanliness factor. Comparatively if the average coating thickness of $100 \mu\text{m}$, the required minimum coating conductivity is then equal to $2.5 \text{ W/m}\cdot\text{K}$.

5.4 Modifying the HEI method to account for APCs

Instead of determining the cleanliness factor associated with a particular coating, the HEI method can be modified by adjusting the material correction factor in equation 5.1. The coated material correction factor is defined as

$$F_M^+ = A_{F_M} F_M \quad (5.25)$$

CHAPTER 5. COATED CONDENSER MODELING

where the coefficient A_{FM} is calculated by solving

$$A_{FM} = \frac{\bar{U}_{\text{coated}}}{U_{\text{HEI}}} \quad (5.26)$$

From equation (5.14), the coated overall heat transfer coefficient \bar{U}_{coated} can be written as

$$\begin{aligned} \bar{U}_{\text{coated}} &= \left(\frac{\ln \frac{d_3}{d_1}}{2k_{\text{eff}} \frac{1}{d_3}} + R_a + \frac{1}{h} + \frac{1}{h_i \frac{d_2}{d_3}} \right)^{-1} \\ &= \left(\frac{\ln \frac{d_3}{d_1}}{2k_{\text{eff}} \frac{1}{d_3}} - \frac{\ln \frac{d_3}{d_2}}{2k_t \frac{1}{d_3}} + \frac{\ln \frac{d_3}{d_2}}{2k_t \frac{1}{d_3}} + R_a + \frac{1}{h} + \frac{1}{h_i \frac{d_2}{d_3}} \right)^{-1} \end{aligned} \quad (5.27)$$

Recalling that for coating thicknesses less than 150 μm , the mass flow rate only changes by 0.39%. Therefore, assuming that the steam-side and water-side convection coefficients do not significantly change as a result of the coating, then

$$R_a + \frac{1}{h} + \frac{1}{h_i \frac{d_2}{d_3}} \approx \frac{1}{U_{\text{HEI}}} \quad (5.28)$$

Substituting this result into equation (5.28) means that equation (5.26) becomes

$$A_{FM} = \frac{1}{U_{\text{HEI}}} \left(\frac{\ln \frac{d_3}{d_1}}{2k_{\text{eff}} \frac{1}{d_3}} - \frac{\ln \frac{d_3}{d_2}}{2k_t \frac{1}{d_3}} + \frac{1}{U_{\text{HEI}}} \right)^{-1} \quad (5.29)$$

Note that the effective coated-tube conductivity can be calculated in terms of the tube conductivity (k_t) and coating conductivity (k_c) using

$$k_{\text{eff}} = \frac{\ln \frac{d_3}{d_1}}{\ln \frac{d_3}{d_2} / k_t + \ln \frac{d_2}{d_1} / k_c} \quad (5.30)$$

Finally the coated overall heat transfer coefficient is equal to

$$\bar{U}_{\text{coated}} = U_{\text{HEI}} \times F_M^+ \quad (5.31)$$

5.5 Coating performance and selection guidelines

Coating guidelines can be formulated in terms of a required HEI material correction factor A_{fm} (section 5.4). Supposing that the APC end user specifies the required HEI

CHAPTER 5. COATED CONDENSER MODELING

material correction factor that the coating must achieve. The required coating conductivity and thickness can be deduced using equation (5.29) to achieve this.

For example, suppose the end user wants an APC that achieves an HEI material correction factor of at least 0.85 on 1-inch Admiralty brass tubing. If it is known that the design value of the HEI overall heat transfer coefficient is $4000 \text{ W/m}^2\cdot\text{K}$, the coating conductivity and thickness can be parametrically solved to satisfy equation (?). The results of this are plotted in figure 5.6.

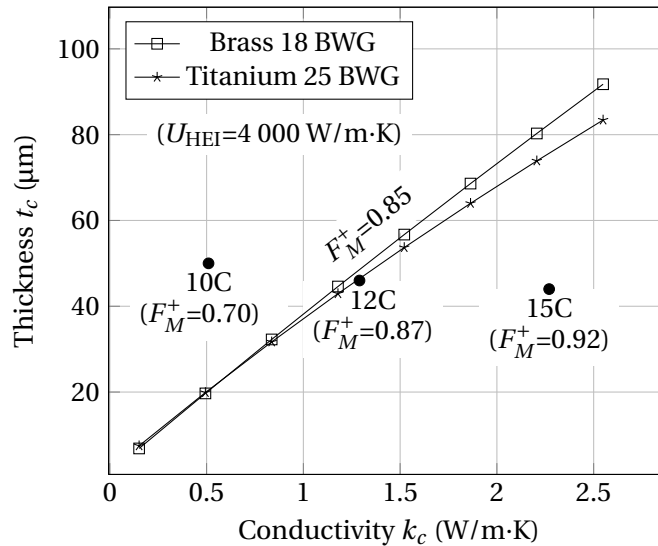


Figure 5.6: Coating thickness versus conductivity

This methodology is readily extended to other tube materials, such as Titanium which is also included in figure 5.6 as well as the results of tubes 10C, 12C, and 15C.

5.6 Relating the single tube tests to the effect on overall condenser performance

The change in ΔT_{lm} between uncoated and coated tests, provides a simple measure of the change in performance. If the flow rates are kept constant before and after coating, the ratio of the overall heat transfer coefficients is

$$\frac{(UA)_{\text{coat}}}{(UA)_{\text{uncoat}}} = \frac{Q_{\text{coat}}}{Q_{\text{uncoat}}} \times \frac{\Delta T_{lm,\text{coat}}}{\Delta T_{lm,\text{uncoat}}} \quad (5.32)$$

The following tests performed on tube 15C practically have the same flow rates before and after coating, as shown in table 5.2:

CHAPTER 5. COATED CONDENSER MODELING

Table 5.2: Tests performed before and after coating of tube 15C

Test	Hot stream flow rate V_h L/s	Cold Stream Flow rate V_c L/s	Mean heat transfer rate Q_m W/m·K	LMTD ΔT_{lm} K
31102	1.09	0.784	7563	10.796
40303	1.11	0.788	7609	11.77
Deviation	-1.80%	-0.51%	-0.60%	-8.28%

This means that

$$\frac{(UA)_{\text{coat}}}{(UA)_{\text{uncoat}}} = \frac{7609}{7563} \times \frac{10.796}{1.77} = 0.92 \quad (5.33)$$

which is within 0.54% of the value predicted by figure 5.4 (equal to 0.925)

5.7 Predicted effect on plant performance

The effect of using APCs on the overall plant efficiency is described using industry rules of thumb as well as actual turbine data. A thermal performance rule of thumb provided by EPRI (1998) states an increase of 0.388 kPa in the condenser back pressure can result in up to 4% increase in heat rate. The Electrical Power Research Institute (EPRI) (1998) defines heat rate to be the ratio of heat supplied by the boiler to the power generated, in metric units this becomes

$$HR = \frac{Q_{\text{fuel}}}{P_{\text{generated}}} \times 3600 \left| \frac{\text{kJ}}{\text{kW}\cdot\text{h}} \right| \quad (5.34)$$

Therefore, lowering the heat rate means more electrical power will be produced for a given amount of heat supplied, and the thermodynamic cycle efficiency will be greater. In terms of temperature, assuming a saturated steam temperature of 38.5 °C, this corresponds to an approximate decrease of 0.38% in efficiency per 1 K increase in saturation temperature. A similar result was concluded by Reuter (2010), who found that for typical wet-cooled systems, an increase of 1 K in steam saturation temperature results in a 0.33% decrease in the gross efficiency.

The power output versus steam temperature for an actual power plant Eskom Technology Group, Eskom Enterprises (2013) is shown in appendix D.5. The gradient of the curve is approximated at the design point and the fractional change in efficiency is thus $\Delta\eta/\eta/\Delta T = -0.39\%/K$.

Consolidating the above results, the average fractional change in efficiency is $\Delta\eta/\eta/\Delta T = -0.37\%/K$. Multiplying this estimate by the previously determined change in steam

CHAPTER 5. COATED CONDENSER MODELING

temperature, yields the fractional change in efficiency in terms of coating conductivity as shown in figure 5.7. Also plotted on this figure are the conductivities of the coatings A, B and C (measured in chapter 4). The respective change in efficiency for each of these coatings is -1.87%, -0.67%, and -0.34%, which shows the sensitivity of coating conductivity to performance. The dependence on thickness is also large and is exacerbated for coatings with low thermal conductivities.

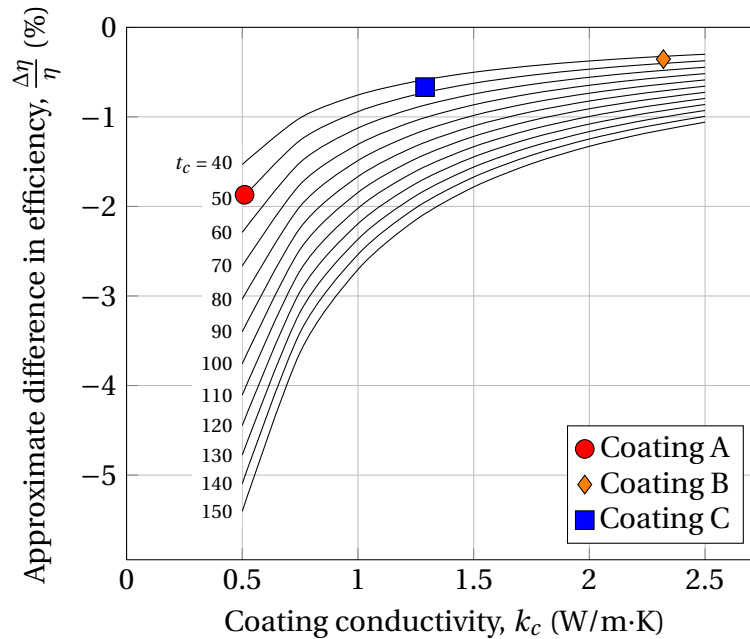


Figure 5.7: Difference in efficiency with coating conductivity and thickness (18 BWG 1-inch admiralty brass, t_c in μm)

During operation the service tubes become fouled despite regular cleaning. A cleanliness factor of around 0.85 is generally included in the design to account for this decreased condenser performance. If the coating is controlled to meet this cleanliness factor, the coated condenser can operate within the design specification. In fact, Frazee & Woodruff (1997) showed that coated tubes did in fact reduce the rate of fouling. Further investigation into the performance of coated tubes whilst in service with respect to their resistance to fouling is necessary.

In conclusion, if APCs are used as part of a refurbishment strategy and are carefully controlled, then the actual performance in-service is likely to be better than the estimates made here. The fouling aspects and in-service performance are the subject of further investigation.

Chapter 6

Conclusion

6.1 Conclusions

Vacuum steam surface condensers have a significant effect on overall plant performance. Degradation mechanisms, including fouling, erosion, and corrosion, lead to reduced performance and premature tube failures. Full-length artificial protective coatings (APCs) have been used to mitigate these mechanisms and are expected to extend the tube-life between 5 and 10 years. Application techniques and enhanced coatings have been developed in South Africa. This thesis details the investigation of these APCs, and the formulated conclusions are discussed below with reference to the objectives stated on page 14.

Objective 1: Details are provided of the double-pipe counter-flow heat exchanger that was successfully built and used to measure the thermal conductivity of these APCs. The measured effective coated-tube conductivity and coating factor of the tested tubes are shown in table 6.1.

Table 6.1: Effective coated-tube conductivities and coating factors

Tube	Effective tube coating conductivity k_{eff} W/m·K	Coating factor R_c $m^2/W\cdot K$
10C	11.3 ± 1.3	$9.82e-5$
11C	19.3 ± 1.3	$5.60e-5$
12C	27.2 ± 1.2	$3.57e-5$
15C	46.9 ± 3.2	$1.98e-5$

Similarly the measured arithmetic mean thermal conductivities of the three coatings used in these tests are listed in table 6.2.

The testing range covers mean water temperatures inside the tube between 17 °C

CHAPTER 6. CONCLUSION

Table 6.2: Measured thermal conductivities

Coating	Thermal conductivity \bar{k}_c W/m·K
A	0.51 ± 0.03
B	2.27 ± 0.25
C	1.29 ± 0.110

and 24 °C. Likewise the mean annular water temperature is in the range of 30 °C to 45 °C. The coating thicknesses range from 44 µm to 130 µm. 1 inch 18 BWG cartridge brass tubing is used in these tests as an alternative to Admiralty brass, although the difference in tube conductivity is only 8.1%.

Objective 2: Using data from static pressure drop measurements, the coated friction factors are compared to the Konakov (cited by Gnielinski, 2009) and Haaland (Haaland, 1983, cited by Kröger, 1998) friction factor correlations. The data is within 5% of these correlations, validating the assumption of the smooth tube analysis.

Objective 3 Condenser tubes experience tube inundation, vapor shearing, and the presence of non-condensable gases. These effects are extracted from the empirical data given by the Heat Exchange Institute (2012) standard, by using the thermal resistance method of analysis. The results of the parametric study show a logarithmic relationship with effective coated-tube conductivity and the number of transfer units (NTU). The cleanliness factor is approximately equal to the ratio of the coated NTU to uncoated NTU, and the cleanliness factor can be used as a measure of the change in performance caused by APCs. Alternatively the HEI method of analysis can be modified by adjusting the material correction factor to account for the APCs.

The experimentally measured uncoated overall heat transfer coefficients are in the range of 4000 W/m²·K to 4500 W/m²·K. These are similar to the HEI calculated values, which indicate condenser conditions with the same cooling water flow rate are approximately 3700 W/m²·K. The ratio of uncoated to coated temperature differences from a particular single tube test is shown to be within 2 % of the results of the parametric study. This provides a very simple relative test to determine the effect on condenser performance, by performing heat transfer tests on a single tube.

Objective 4: To achieve a cleanliness factor of at least 0.85 (on 25.4 mm brass tubing) with coating thickness not exceeding 50 µm, it is recommended that the coating conductivity should be not less than 1.2 W/m·K. For the same cleanliness factor with coating thicknesses not exceeding 100 µm, the coating conductivity must be no less than 2.4 W/m·K.

The expected fractional change in efficiency of a new condenser coated with 50 µm of either coating A, B or C, is approximately -1.9%, -0.36%, or -0.67% respectively. Importantly these results consider coatings applied to new tubes. In practice APCs

CHAPTER 6. CONCLUSION

are applied to in-service (used) tubes, after the removal of any fouling layer. These in-service tubes may also have reduced wall thicknesses. These factors must be considered when predicting the actual performance on a case-specific condition.

6.2 Recommendations

In practice, when evaluating different coatings it is recommended that heat transfer testing is conducted to verify the actual coating performance (at conditions similar to those experienced in service). This also ensures that the application technique is suitable and meets the minimum average coating thickness specification.

This investigation has been focused on the thermal performance aspects of APCs. It is recommended that an evaluation of the resistance to fouling for each coating is completed. That data could then be used together with the information provided here to schedule optimum cleaning and coating procedures. Furthermore, the fundamental thermal resistance model presented here should be extended to two- and three-dimensional models to better understand the steam-side effects.

List of references

- American Society of Mechanical Engineers (ASME). 2006. *Test Uncertainty. National standard PTC-19.1-2005*, American Society of Mechanical Engineers (ASME), New York.
- Brown, K.K., Coleman, H.W., Steele, W.G. & Taylor, R.P. 1996. Evaluation of correlated bias approximations in experimental uncertainty analysis. *AIAA Journal*, 5:1013–1018.
- Butterworth, D. 1981. Inundation without vapor shear. In P.J. Marto & R.H. Nunn (eds.), *Power condenser heat transfer technology*, pages 271–278. New York: Hemisphere Publishing Corporation.
- Cengel, A.Y. & Ghajar, A. 2011. *Heat and Mass Transfer Fundamentals and Applications*. New York: McGraw Hill.
- Coleman, H.W. & Steele, W.G. 2009. *Experimentation, Validation, and Uncertainty Analysis for Engineers*. 3rd edition. Hoboken, New Jersey: John Wiley and Sons, Inc.
- Davis, J.R. 2001. Copper and copper alloys. In *ASM Specialty Handbook*. ASM International.
- Dirker, J. & Meyer, J.P. 2005. Convective heat transfer coefficients in concentric annuli. *Heat Transfer Engineering*, 26(2):38–44.
- Dobersek, D. & Goricanec, D. 2007. Influence of water scale on thermal flow losses of domestic appliances. *International Journal of Mathematical Models and Methods in Applied Sciences*, 1(2):55–61.
- Electrical Power Research Institute (EPRI). 1987. *Recommended practices for operating and maintaining steam surface condensers*. Technical Report RP1689-8, Electrical Power Research Institute, Boston, Massachusetts.
- Electrical Power Research Institute (EPRI). 1998. *Thermal Performance Engineer's Handbook: Introduction to Thermal Performance*. Technical Report TR-107422-V1, Electrical Power Research Institute, Palo Alto, California.
- Eskom Technology Group, Eskom Enterprises. 2013. Private communication.
- Fraze, R.O. & Woodruff, B.N. 1997. *In-situ Coating of Condenser Tubes as an Alternative to Retubing*. Technical Report TR-107068, Electrical Power Research Institute, Palo Alto, California.

LIST OF REFERENCES

- Gnielinski, V. 2007. Berechnung des Druckverlustes in glatten konzentrischen Ringspalten bei ausgebildeter laminarer und turbulenter Strömung. *Chemie Ingenieur Technik*, 79:91–95.
- Gnielinski, V. 2009. Heat transfer coefficients for turbulent flow in concentric annular ducts. *Heat Transfer Engineering*, 30(6):431–436.
- Goodfellow Cambridge Ltd. 2013. Available: [http://www.goodfellow.com/E/Brass'.html](http://www.goodfellow.com/E/Brass%20.html), [2013, August 22].
- Haaland, S.E. 1983. Simple and explicit formulas for the friction factor in turbulent pipe flow. *American Society of Mechanical Engineers (ASME) Journal of Fluids Engineering*, 105:89–90.
- Heat Exchange Institute. 2012. *Standards for steam surface condensers*. Heat Exchange Institute (HEI), Cleveland, Ohio, 11th edition.
- Hiroshi, H. 2011. *Condensation heat transfer in tube banks* [online]. Available: <http://www.thermopedia.com/content/1210/>, [2013, June 26].
- Honing, W. & Kröger, D.G. 2006. Thermal-flow characteristics of condenser tubes. Confidential report to Eskom, ITM/DGK/23/01/06, Stellenbosch University: Institute for Thermodynamics and Mechanics.
- Horn, M.J. & Mitchell, J.E. 2005. New developments in condenser tube coatings. In *Condenser Technology Conference*, TR-1010322, pages 429–436. Electrical Power Research Institute (EPRI).
- Incropera, F.P., Dewitt, D.P., Bergman, T.L. & Lavine, A.S. 2007. *Introduction to Heat Transfer*. 5th edition. United States of America: Wiley.
- Inglesi, R. & Pouris, A. 2013. Forecasting electricity demand in south africa: A critique of Eskom's projections. *South African Journal of Science*, 106(16):50–53. Available: <http://www.scielo.org.za/pdf/sajs/v106n1-2/v106n1-2a16.pdf> [2013, April 04].
- Kröger, D.G. 1998. *Air-cooled Heat Exchangers and Cooling Towers: Thermal-flow performance evaluation and design*. Stellenbosch University: Department of Mechanical Engineering.
- Marrero, T.R. & Manson, E.A. 1972. Gaseous diffusion coefficients. *Journal of physical chemistry reference data*, 1:3–118.
- McEwan, J.J. 2004. *Corrosion Control in Southern Africa*. 2nd edition. Corrosion Institute of Southern Africa.
- McMillen, E.L. & Larson, R.E. 1994. Annular heat transfer coefficients for turbulent flow. *Transactions of the American Institute of Chemical Engineering*, 40:177–202.

LIST OF REFERENCES

- Munson, B., Young, D. & Okiishi, T. 2006. *Fundamentals of Fluid Mechanics*. 5th edition. Wiley.
- Northcott, K. 2009. *An Eskom Overview of Condenser and Heat Exchanger Life Extension Technologies*. Presentation to IAHR Conference.
- Nusselt, W. 1916. Die oberflächenkondensation des wasserdampfes. *Zeitschrift des Vereins Deutscher Ingenieure*, 60:541.
- Petukhov, B.S. 1970. Heat transfer and friction in turbulent pipe flow with variable physical properties. *Advances in heat transfer*, 6:504–564.
- Petukhov, B.S. & Krillov, V.V. 1958. On heat exchange at turbulent flow of liquids in pipes. *Teploenergetika*, 4:63–68.
- Prandtl, L. 1944. *Führer durch die Strömungslehre*. Braunschweig: Verlag Vieweg.
- Putman, R.E. 2001. *Steam surface condensers: Basic principles, performance monitoring, and maintenance*. New York: ASME press.
- Rabas, T.J. & Cane, D. 1983. An update of intube forced convection heat transfer coefficients of water. *Desalination*, 44:109–119.
- Reuter, H.C.R. 2010. *Performance evaluation of natural draught cooling towers with anisotropic fills*. Ph.D. thesis, Department of Mechanical and Mechatronic Engineering, Stellenbosch University.
- Rose, J.W. 1980. Approximate equations for forced convection condensation in the presence of non-condensing gas on a flat and horizontal tube. *International Journal of Heat and Mass Transfer*, 23:539–546.
- Sato, S., Nohetani, T. & Hotta, Y. 1985. Improvement of surface condenser performance by in-situ artificial protective film coating. In *Effects of Fouling and Corrosion on Heat Transfer*, volume 50, pages 17–24. Miami Beach, Florida: The American Society of Mechanical Engineers (ASME).
- Sieberts, D. 2011. Condenser life extension technology at eskom. In *Condenser technology*, page 244. Chicago, Illinois: Electrical Power Research Institute (EPRI).
- Silver, R.S. 1963. An approach to a general theory of surface condensers. In *Proceedings of the Institution of Mechanical Engineers*, volume 178, pages 339–376. Institution of Mechanical Engineers.
- Tarrad, A.H. & Majeed, L.M. 2010. The application of a step by step technique for the performance prediction of thermal power plant surface condensers. *Journal of Engineering*, 16:4748–4770.

LIST OF REFERENCES

Tsou, J. 2002. *Condenser Performance Monitoring Practices*. Technical Report TR-1007309, Electrical Power Research Institute (EPRI).

United States Energy Information Administration. 2013. *South Africa – Analysis [Online]*. Available: <http://www.eia.gov/countries/cab.cfm?fips=SF>, [2013, April 04].

Weisbach, J. 1855. *Die Experimental-Hydraulik*. Freiberg: Engelhardt.

White, F.M. 2005. *Fluid Mechanics*. 5th edition. McGraw Hill.

Appendices

Appendix A

Properties of fluids

A.1 Thermophysical properties of saturated water from 273.15 K to 380 K (Kröger, 1998)

- Density (kg/m³):

$$\rho = (1.49343 \times 10^{-3} - 3.7164 \times 10^{-6} T_w + 7.09782 \times 10^{-9} T_w^2 - 1.90321 \times 10^{-20} T_w^6)^{-1} \quad (\text{A.1})$$

- Specific heat (J/kg·K):

$$c_p = 8.15599 \times 10^3 - 2.80627 \times 10^1 T_w + 5.11283 \times 10^{-2} T_w^2 - 2.17582 \times 10^{-13} T_w^6 \quad (\text{A.2})$$

- Kinematic viscosity (kg/m·s)

$$\mu = 2.414 \times 10^{-5} \times 10^{\frac{247.8}{(T_w - 140)}} \quad (\text{A.3})$$

- Thermal conductivity (W/m·K)

$$k_f = -6.14255 \times 10^{-1} + 6.9962 \times 10^{-3} T_w - 1.01075 \times 10^{-5} T_w^2 + 4.74737 \times 10^{-12} T_w^4 \quad (\text{A.4})$$

- Prandtl number

$$Pr = \frac{\mu c_p}{k_f} \quad (\text{A.5})$$

- Latent heat of vaporization (J/kg)

$$i_{fg} = 3.4831814 \times 10^6 - 5.8627703 \times 10^3 T + 12.139568 T^2 - 0.0140290431 T^3 \quad (\text{A.6})$$

APPENDIX A. PROPERTIES OF FLUIDS

A.2 Thermophysical properties of saturated water vapor from 273.15 K to 380 K (Kröger, 1998)

- Vapor pressure (Pa):

$$p_v = 10^z \quad (\text{A.7})$$

with

$$\begin{aligned} z = & 10.79586(1 - 273.16/T) + 5.2808 \log_{10}(273.16/T) \\ & + 1.50474 \times 10^{-4} \{1 - 10^{-8.29692[(T/273.16)-1]}\} \\ & + 4.2873 \times 10^{-4} \{10^{4.76955(1-273.16/T)} - 1\} + 2.78618312 \end{aligned}$$

A.3 Thermophysical properties of mixtures of air and water vapor (Kröger, 1998)

- Density (kg air-vapor /m³)

$$\rho_{mix} = (1 + w) \left[1 - \frac{w}{w + 0.62198} \right] p_{mix} / (287.08T) \quad (\text{A.8})$$

- Kinematic viscosity (kg/m·s)

$$\mu_{mix} = (X_a \mu_a M_a^{0.5} + X_v \mu_v M_v^{0.5}) / (X_a M_a^{0.5} + X_v M_v^{0.5}) \quad (\text{A.9})$$

where $M_a = 28.97$ kg/mole, $M_v = 10.016$ kg/mole, $X_a = 1/(1+1.608w)$ and $X_v = w/(w+0.622)$.

- Dynamic viscosity of air (kg/m·s)

$$\mu_a = 2.287973 \times 10^{-6} + 6.2598 \times 10^{-8} T - 3.132 \times 10^{-11} T^2 + 8.15038 \times 10^{-15} T^3 \quad (\text{A.10})$$

Appendix B

Experimental data

The experimental data is grouped into three sections. The first contains all of the isothermal test data. Thereafter the uncoated test data is listed. Thirdly the coated test data is given.

B.1 Isothermal tests

Table B.1 records the mean temperatures and flow rates of the isothermal tests.

Table B.1: Isothermal tests: recorded temperatures and flow rates

Tube	T_{hi} °C	T_{ho} °C	T_{ci} °C	T_{co} °C	V_h L/s	V_c L/s	ΔT_h K	ΔT_c K
15U	24.76	24.75	24.72	24.74	1.29	1.28	0.01	0.02
10C	36.12	36.10	36.07	36.08	1.51	1.50	-0.01	0.08
12C	25.13	25.13	25.12	25.13	1.38	1.38	0.04	-0.01
15C	23.40	23.38	23.35	23.37	1.09	1.08	0.02	0.02

APPENDIX B. EXPERIMENTAL DATA

B.2 Uncoated tube tests

The recorded temperatures and flow rates from tube 10U are listed in table B.2, and the processed in table B.3.

Table B.2: Tube 10U: recorded temperatures and flow rates

Test	T_{hi} °C	T_{ho} °C	T_{ci} °C	T_{co} °C	Av_h L/s	Av_c L/s	ΔT_h °C	ΔT_c °C	EB %
012908	34.873	33.486	24.150	26.143	1.22	0.85	1.397	1.980	-0.60
012909	34.965	33.510	24.182	26.180	1.10	0.80	1.460	1.996	0.50
013001	34.715	33.153	23.546	25.535	1.03	0.80	1.510	2.013	1.60
013002	35.044	33.338	23.529	25.523	0.94	0.80	1.671	2.016	0.90
013003	35.617	33.488	23.515	25.395	0.71	0.80	2.139	1.892	-0.40
013004	36.665	33.919	23.452	25.244	0.52	0.79	2.773	1.810	0.20
013005	36.816	34.491	23.471	25.560	0.72	0.80	2.347	2.108	-0.30
013006	36.810	34.457	23.503	25.578	0.69	0.78	2.376	2.121	0.20
013007	36.066	34.774	23.565	26.110	1.52	0.77	1.292	2.574	0.80
013101	36.896	34.572	23.933	25.965	0.69	0.78	2.333	2.031	-0.70
013102	36.850	34.770	24.072	26.207	0.81	0.78	2.066	2.127	-0.30
013104	36.788	35.095	24.434	26.709	1.04	0.77	1.691	2.263	0.00
013105	36.804	35.162	24.549	26.813	1.11	0.80	1.648	2.258	-0.10
013106	36.724	35.230	24.624	26.944	1.25	0.80	1.493	2.300	-0.30
013107	36.435	35.032	24.742	27.011	1.30	0.80	1.401	2.251	-0.10
013108	36.614	35.344	24.796	27.201	1.48	0.78	1.279	2.393	-0.20
013109	36.432	35.265	24.827	27.240	1.61	0.78	1.162	2.400	0.70
013110	36.270	35.188	24.842	27.263	1.75	0.78	1.072	2.408	0.90

Table B.3: Tube 10U: Average temperature trends, mean heat transfer, and inner convection coefficient

Test	AHTT °C1/min	ACTT °C1/min	Q_m W	h_i W/m ² ·K
012908	$4.40 \cdot 10^{-3}$	$5.90 \cdot 10^{-3}$	7055.7	16873.69
012909	$3.30 \cdot 10^{-3}$	$-3.90 \cdot 10^{-3}$	6671.4	18794.53
013001	$-2.10 \cdot 10^{-3}$	$-3.10 \cdot 10^{-3}$	6627.4	19147.97
013002	$-1.20 \cdot 10^{-3}$	$-3.80 \cdot 10^{-3}$	6625.8	19406.54
013003	$1.00 \cdot 10^{-4}$	$-3.20 \cdot 10^{-3}$	6301.1	19287.86
013004	$-1.40 \cdot 10^{-3}$	$-9.20 \cdot 10^{-3}$	5959.8	19648.17
013005	$7.70 \cdot 10^{-3}$	$6.90 \cdot 10^{-3}$	6967.6	19424.68
013006	$-2.00 \cdot 10^{-4}$	$-8.00 \cdot 10^{-4}$	6784.6	20496.45
013007	$-3.80 \cdot 10^{-3}$	$-1.60 \cdot 10^{-3}$	8169.9	20663.31

APPENDIX B. EXPERIMENTAL DATA

Table B.3 – continued from previous page

013101	$-7.00 \cdot 10^{-3}$	$1.32 \cdot 10^{-2}$	6630.1	20101.30
013102	$-3.20 \cdot 10^{-3}$	$7.10 \cdot 10^{-3}$	6919.2	20148.01
013104	$3.90 \cdot 10^{-3}$	$1.97 \cdot 10^{-2}$	7307.0	20204.54
013105	$1.95 \cdot 10^{-2}$	$1.22 \cdot 10^{-2}$	7562.9	18584.67
013106	$-2.00 \cdot 10^{-3}$	$1.60 \cdot 10^{-2}$	7711.0	18657.30
013107	$1.01 \cdot 10^{-2}$	$8.10 \cdot 10^{-3}$	7539.3	18624.15
013108	$1.05 \cdot 10^{-2}$	$3.00 \cdot 10^{-3}$	7826.0	19441.10
013109	$1.87 \cdot 10^{-2}$	$5.90 \cdot 10^{-3}$	7805.1	19479.79
013110	$2.29 \cdot 10^{-2}$	$-1.00 \cdot 10^{-3}$	7853.9	19306.85

Similarly table B.4 contains the recorded temperatures and flow rates pertaining to tests conducted on tube 15U. The processed data is given in table B.5.

Table B.4: Tube 15U: recorded temperatures and flow rates

Test	T_{hi} °C	T_{ho} °C	T_{ci} °C	T_{co} °C	Av_h L/s	Av_c L/s	ΔT_h °C	ΔT_c °C	EB %
030703	35.464	33.890	23.116	25.408	1.16	0.79	1.565	2.301	0.00
030704	35.379	33.562	23.090	25.201	0.94	0.80	1.800	2.111	0.20
030706	35.755	33.673	22.955	25.041	0.80	0.79	2.085	2.086	-0.50
031001	34.146	32.947	22.190	24.585	1.62	0.81	1.201	2.415	0.20
031002	34.178	32.918	22.005	24.424	1.53	0.79	1.268	2.436	-0.10
031003	34.710	33.313	22.043	24.509	1.41	0.80	1.413	2.478	-0.60
031004	34.709	33.225	22.095	24.489	1.30	0.80	1.500	2.402	-0.70
031101	34.617	33.014	21.571	23.996	1.21	0.79	1.578	2.456	0.50
031102	34.176	32.501	21.387	23.691	1.09	0.78	1.662	2.332	0.80
031103	34.322	32.507	21.310	23.575	1.00	0.80	1.801	2.290	0.60
031104	34.582	32.612	21.263	23.516	0.91	0.79	1.963	2.271	0.20
031105	34.661	32.527	21.216	23.403	0.81	0.79	2.132	2.206	0.00
031106	34.897	32.490	21.151	23.241	0.70	0.80	2.412	2.115	-0.50
031107	35.282	32.618	21.149	23.185	0.61	0.79	2.657	2.052	0.50

Table B.5: Tube 15U: Average temperature trends, mean heat transfer, and inner convection coefficient

Test	AHTT °C1/min	ACTT °C1/min	Q_m W	h_i W/m ² ·K
030703	$1.45 \cdot 10^{-2}$	$3.20 \cdot 10^{-3}$	7581.2	7559.15
030704	$-1.20 \cdot 10^{-3}$	$-3.10 \cdot 10^{-3}$	7055.9	7495.37
030706	$8.60 \cdot 10^{-3}$	$-7.30 \cdot 10^{-3}$	6889.7	7602.81
031001	$-6.90 \cdot 10^{-3}$	$-9.60 \cdot 10^{-3}$	8076.3	7495.12

APPENDIX B. EXPERIMENTAL DATA

Table B.5 – continued from previous page

031002	$-9.80 \cdot 10^{-3}$	$-3.80 \cdot 10^{-3}$	8050.4	7594.17
031003	$1.56 \cdot 10^{-2}$	$3.90 \cdot 10^{-3}$	8229.9	7578.83
031004	$2.80 \cdot 10^{-3}$	$4.90 \cdot 10^{-3}$	8007.4	7568.56
031101	$8.20 \cdot 10^{-3}$	$-6.60 \cdot 10^{-3}$	8036.7	7649.18
031102	$-1.01 \cdot 10^{-2}$	$-5.40 \cdot 10^{-3}$	7556.2	7733.79
031103	$7.00 \cdot 10^{-4}$	$-5.00 \cdot 10^{-3}$	7537.2	7647.85
031104	$-6.80 \cdot 10^{-3}$	$-1.80 \cdot 10^{-3}$	7478.0	7671.49
031105	$-5.20 \cdot 10^{-3}$	$-4.00 \cdot 10^{-3}$	7206.3	7741.14
031106	$1.91 \cdot 10^{-2}$	$-1.50 \cdot 10^{-3}$	7039.2	7628.87
031107	$-3.60 \cdot 10^{-3}$	$3.40 \cdot 10^{-3}$	6724.0	7725.53

B.3 Coated tube tests**Table B.6:** Tube 10C: recorded temperatures and flow rates

Test	T_{hi} °C	T_{ho} °C	T_{ci} °C	T_{co} °C	V_h L/s	V_c L/s	ΔT_h °C	ΔT_c °C	EB %
032804	37.466	36.225	22.017	24.132	1.330	0.770	1.249	2.151	-0.07
032801	37.249	36.183	22.043	24.126	1.590	0.800	1.050	2.133	0.53
031109	36.380	35.273	21.640	23.650	1.430	0.780	1.111	7.467	-1.02
031108	35.296	34.372	21.417	23.346	1.650	0.780	0.874	16.619	-1.08

Table B.7: Tube 10C: processed heat transfer data

Test	AHTT °C/min	Q_m W	k_c W/m·K	Δk_c W/m·K	k_{eff} W/m·K	R_c'' K/W
032804	$1.05 \cdot 10^{-2}$	6860.9	0.52	0.03	11.66	$9.55 \cdot 10^{-5}$
032801	$9.00 \cdot 10^{-3}$	7021.2	0.51	0.03	11.32	$9.82 \cdot 10^{-5}$
031109	$8.72 \cdot 10^{-3}$	6547.6	0.50	0.04	11.21	$9.94 \cdot 10^{-5}$
031108	$1.38 \cdot 10^{-3}$	6304.5	0.50	0.04	11.20	$9.95 \cdot 10^{-5}$

Table B.8: Tube 11C: recorded temperatures and flow rates

Test	T_{hi} °C	T_{ho} °C	T_{ci} °C	T_{co} °C	V_h L/s	V_c L/s	ΔT_h °C	ΔT_c °C	EB %
022301	36.530	35.213	23.267	25.283	1.220	0.800	1.319	2.016	-0.02
022202	39.446	37.275	23.833	25.979	0.790	0.780	2.108	2.153	0.74
022201	37.534	35.656	23.941	25.809	0.790	0.780	1.776	1.874	1.78
022003	37.051	35.785	24.253	26.270	1.180	0.740	1.274	2.002	-0.25

APPENDIX B. EXPERIMENTAL DATA

Table B.8 – continued from previous page

022002	36.856	35.656	24.018	25.897	1.420	0.910	1.223	1.878	-0.64
--------	--------	--------	--------	--------	-------	-------	-------	-------	-------

Table B.9: Tube 11C: processed heat transfer data

Test	AHTT °C/min	Q_m W	k_c W/m·K	Δk_c W/m·K	k_{eff} W/m·K	R_c'' K/W
022301	0.00	6693.8	2.29	0.10	19.17	0.00
022202	0.18	7008.7	2.26	0.10	18.98	0.00
022201	0.04	6049.4	2.24	0.10	18.79	0.00
022003	0.00	6202.0	2.23	0.10	18.82	0.00
022002	-0.01	7132.9	2.29	0.10	18.95	0.00

Table B.10: Tube 12C: recorded temperatures and flow rates

Test	T_{hi} °C	T_{ho} °C	T_{ci} °C	T_{co} °C	V_h L/s	V_c L/s	ΔT_h °C	ΔT_c °C	EB %
020802	36.295	35.047	23.065	25.302	1.480	0.820	1.234	2.249	0.35
020801	36.190	35.037	22.959	25.262	1.610	0.800	1.127	2.320	1.18
012406	34.595	33.482	23.959	25.494	1.510	1.110	1.139	1.495	-0.74
012405	34.734	33.753	23.981	25.833	1.500	0.800	1.014	1.818	-1.22

Table B.11: Tube 12C: processed heat transfer data

Test	AHTT °C/min	Q_m W	k_c W/m·K	Δk_c W/m·K	k_{eff} W/m·K	R_c'' K/W
020802	0.03	7656.4	1.30	0.11	27.90	0.00
020801	0.00	7660.6	1.27	0.10	27.31	0.00
012406	-0.01	7039.4	1.27	0.10	25.90	0.00
012405	0.03	6169.0	1.32	0.12	27.94	0.00

Table B.12: Tube 15C: recorded temperatures and flow rates

Test	T_{hi} °C	T_{ho} °C	T_{ci} °C	T_{co} °C	V_h L/s	V_c L/s	ΔT_h °C	ΔT_c °C	EB %
040308	35.469	33.726	21.227	23.565	1.060	0.780	1.803	2.366	-1.80
040307	35.477	34.142	21.333	23.893	1.520	0.780	1.380	2.590	-1.62
040303	35.909	34.260	22.165	24.457	1.110	0.790	1.674	2.316	-1.05
032810	35.894	34.293	22.940	25.132	1.080	0.780	1.627	2.213	-0.51
032809	35.892	34.422	22.957	25.223	1.220	0.790	1.500	2.284	-1.15
032806	36.162	34.863	22.724	25.226	1.510	0.790	1.321	2.528	0.48

APPENDIX B. EXPERIMENTAL DATA

Table B.13: Tube 15C: processed heat transfer data

Test	AHTT °C1/min	Q_m W	k_c W/m·K	Δk_c W/m·K	k_{eff} W/m·K	R_c'' K/W
040308	$-7.06 \cdot 10^{-3}$	7748.3	2.13	0.21	45.43	$2.06 \cdot 10^{-5}$
040307	$-4.53 \cdot 10^{-2}$	8493.6	2.14	0.22	45.86	$2.05 \cdot 10^{-5}$
040303	0.00	7609.5	2.04	0.20	43.26	$2.16 \cdot 10^{-5}$
032810	$8.85 \cdot 10^{-3}$	7208.2	2.41	0.27	49.38	$1.82 \cdot 10^{-5}$
032809	$-1.98 \cdot 10^{-3}$	7502.6	2.49	0.28	50.84	$1.76 \cdot 10^{-5}$
032806	$-5.60 \cdot 10^{-4}$	8234.0	2.46	0.27	50.86	$1.78 \cdot 10^{-5}$

Appendix C

Condenser modeling

C.1 Axial variation in condenser tube wall temperature

The variation in wall temperature may be dealt with using the method proposed by Silver (1963). First it is necessary to rewrite the outer convection coefficient in terms of the rate of condensation per unit area to be r .

Consider the elemental length of a condenser tube shown in figure C.1.

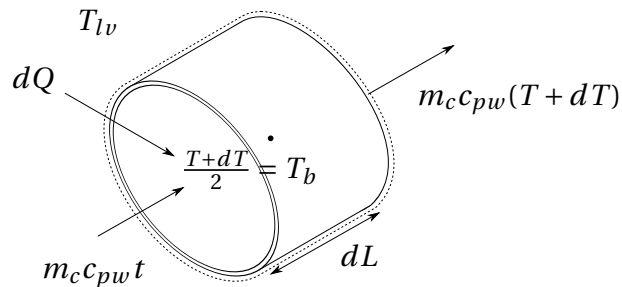


Figure C.1: Elemental length of condenser tube

In the absence of vapor shearing, the energy balance of the steam across yields

$$\frac{dQ}{dA} = m_{con} i_{fg}^* \quad (C.1)$$

$$= r \cdot i_{fg}^* \quad (C.2)$$

The outer convection coefficient is related to the heat transfer by

$$\frac{dQ}{dA} = h_g (T_{lv} - T_b) \quad (C.3)$$

APPENDIX C. CONDENSER MODELING

Combining equations (C.2) and (C.3)

$$h_g(T_{lv} - T_w) = r \cdot i_{fg} \quad (C.4)$$

and hence substituting into equation (5.3) yields the convection coefficient in terms of the condensation rate,

$$\frac{1}{h_g} = \frac{1}{0.728^{\frac{4}{3}} k_{con}} \left[\frac{\mu_l d_3}{\rho_{con}(\rho_{con} - \rho_v) g} \right]^{\frac{1}{3}} \cdot r^{\frac{1}{3}} \quad (C.5)$$

Next the outer convection coefficient is related to the cooling water temperature. The heat transfer across the element is given in terms of the overall heat transfer coefficient U , as

$$\frac{dQ}{dA} = U(T_{cv} - T_b) \quad (C.6)$$

where t is the mean water temperature. But from the energy balance of the cooling water,

$$dQ = m_{cw} c_{p,cw} dT \quad (C.7)$$

Therefore

$$m_{cw} c_{p,cw} dT = h_g \pi d_3 (T_{lv} - T_b) dL \quad (C.8)$$

Rearranging this result,

$$\frac{dt}{h_g(T_{lv} - T_b)} = \frac{\pi d_3 dL}{m_{cw} c_{p,cw}} \quad (C.9)$$

Equate equations (C.2) and (C.2) and differentiate with respect to dT :

$$\frac{d}{dt} \left(\frac{r}{U} \cdot i_{fg}^* \right) = -1 \quad (C.10)$$

in which case dT may be expressed as

$$\begin{aligned} dT &= -d \left(\frac{r}{U} \right) \cdot i_{fg}^* \\ &= -i_{fg}^* \left\{ \left(\frac{1}{h_i \cdot \frac{d_2}{d_3}} + \frac{\ln \frac{d_3}{d_2}}{2\pi k_t \frac{1}{d_3}} \right) dr + \frac{4}{3} \cdot \frac{1}{0.655 k_{con}} \left(\frac{\mu_l d_3}{\rho_{con}(\rho_{con} - \rho_v) g} \right)^{\frac{1}{3}} \cdot r^{\frac{1}{3}} dr \right\} \end{aligned} \quad (C.11)$$

Equations (C.2) and (C.11) are substituted into equation (C.9) to yield

$$\frac{1}{r} \left\{ \left(\frac{1}{h_i \cdot \frac{d_2}{d_3}} + \frac{\ln \frac{d_3}{d_2}}{2\pi k_t \frac{1}{d_3}} \right) dr + \frac{4}{3} \cdot \frac{1}{0.655 k_{con}} \left[\frac{\mu_{con} d_3}{\rho_{con}(\rho_{con} - \rho_v) g} \right]^{\frac{1}{3}} \cdot r^{\frac{1}{3}} dr \right\} = \frac{\pi d_3 dL}{m_{cw} c_{p,cw}} \quad (C.12)$$

APPENDIX C. CONDENSER MODELING

Integrating this result from $L = 0$ to $L = L$, noting that at $L = 0$: $r = r_1$,

$$\left(\frac{1}{h_i \cdot \frac{d_2}{d_3}} + \frac{\ln \frac{d_3}{d_2}}{2\pi k_t \frac{1}{d_3}} \right) \ln \frac{r_1}{r} + 4 \frac{1}{0.655 k_{con}} \left[\frac{\mu_{con} d_3}{\rho_{con}(\rho_{con} - \rho_v) g} \right]^{\frac{1}{3}} \left(r_1^{\frac{1}{3}} - r^{\frac{1}{3}} \right) = \frac{T_{cv} d_3 L}{m_{cw} c_{p,cw}} \quad (C.13)$$

r_1 is calculated using equation (C.2), i.e.

$$\left(\frac{1}{h_i \cdot \frac{d_2}{d_3}} + \frac{\ln \frac{d_3}{d_2}}{2\pi k_t \frac{1}{d_3}} \right) r_1 + \frac{1}{0.655 k_{con}} \left[\frac{\mu_{con} d_3}{\rho_{con}(\rho_{con} - \rho_v) g} \right]^{\frac{1}{3}} r_1^{\frac{4}{3}} = \frac{T_{lv} - T_{ci}}{i_{fg}} \quad (C.14)$$

Using this result with equation (C.13), the condensation rate at the outlet of the tube, i.e. r_2 , can be determined. With these results the mean rate of condensation is

$$\bar{r} = \frac{r_1 + r_2}{2} \quad (C.15)$$

Giving the following result for the mean heat transfer coefficient

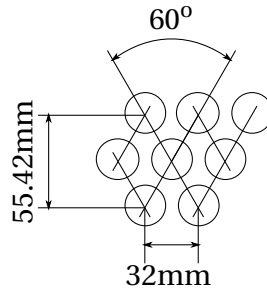
$$\bar{h}_g = \frac{1}{0.655 k_{con}} \left(\frac{\mu_{con} d_3}{\rho_{con}(\rho_{con} - \rho_v) g} \right)^{\frac{1}{3}} \cdot \bar{r}^{\frac{1}{3}} \quad (C.16)$$

C.2 Modeling parameters

For the purposes of this study, consider a typical single shell, single pass condenser (with Admiralty brass tubes) and representative parameters as follows:

Condenser duty per compartment (100% load)	Q_{duty}	=	265.1 MW
Cleanliness factor	F_c	=	1.0
Cooling water flow	V_w	=	6.5 m ³ /s
Water temperature in	T_{ci}	=	21.1 °C
Tube outer diameter	d_3	=	25.4 mm
Tube inner diameter	d_2	=	22.91 mm
Effective length	L	=	9 m
Number of tubes per pass	N_p	=	8400
Number of tube rows	n	=	100
Pumping power (only along tube length)	$\Delta p \cdot V$	=	90 kW
Initial air concentration	w	=	0.05%

APPENDIX C. CONDENSER MODELING

**Figure C.2:** Tube spacing in bundle

The tube spacing is shown in figure C.2, from which it follows that ψ is equal to 0.49.

C.3 Steam vapor velocity regression

An excerpt from the calculated γ values for $w=0.05\%$ is shown below in table C.2.

Table C.2: Calculated γ values for Admiralty brass and $w = 0.05\%$

γ	ΔT_{lm} K	v_{∞} m/s	$m_w c_{pw}$ W	p_s kPa	TTD K
0.560	17.04	24.09	1567.7	11598.6	8.91
0.566	15.76	27.82	1830.0	9931.4	8.68
0.572	14.74	31.12	2092.3	8805.5	8.46
0.580	13.90	34.07	2354.7	7993.3	8.26
0.589	13.19	36.71	2617.0	7380.0	8.06
0.600	12.57	39.10	2879.3	6900.9	7.88
0.612	12.04	41.26	3141.6	6516.2	7.71
0.625	11.57	43.24	3404.0	6200.2	7.54
0.638	11.14	45.05	3666.3	5935.9	7.39
0.651	10.77	46.72	3928.6	5711.0	7.24
0.665	10.42	48.26	4191.0	5518.0	7.11
0.669	10.15	49.60	4453.3	5360.6	7.02
0.674	9.90	50.84	4715.6	5222.3	6.93
0.678	9.67	51.98	4978.0	5100.4	6.85
0.682	9.47	53.04	5240.3	4992.8	6.77
0.685	9.28	54.03	5502.6	4896.8	6.71
0.689	9.11	54.94	5765.0	4810.4	6.64
0.692	8.95	55.79	6027.3	4732.9	6.59

Appendix D

Sample calculations

Four sample calculations are included: the uncoated tube 15U, the coated tube 15C, the HEI method, and finally a calculation using the thermal resistance method.

D.1 Analysis of uncoated tube 15U

The geometry and recorded test data of test number 031107 are:

Effective heat transfer length	L	=	1.981 m
Annulus diameter	d_4	=	0.03355 m
Tube outer diameter	d_3	=	0.02534 m
Tube inner diameter	d_2	=	0.023125 m
Cold inlet temperature	T_{ci}	=	21.149 °C
Cold outlet temperature	T_{co}	=	23.185 °C
Annulus inlet temperature	T_{hi}	=	35.282 °C
Annulus outlet temperature	T_{ho}	=	32.618 °C
Cold volumetric flow rate	V_c	=	0.79 l/s
Hot volumetric flow rate	V_h	=	0.61 l/s
Thermal conductivity of tube	k_t	=	120 W/m·K
Cold stream temperature difference	ΔT_c	=	2.657 K
Hot stream temperature difference	ΔT_h	=	2.052 K

APPENDIX D. SAMPLE CALCULATIONS

The bulk mean temperature of the cold stream is

$$T_{cm} = \frac{21.149 + 23.185}{2} + 273.15 = 295.3 \text{ K}$$

Evaluating the thermophysical property data at this temperature yields:

- the density using equation A.1

$$\begin{aligned} \rho_c &= [1.49343 \times 10^{-3} - 3.7164 \times 10^{-6}(295.3) + 7.09782 \times 10^{-9}(295.3)^2 - 1.90321 \times 10^{-20}(295.3)^6]^{-1} \\ &= 997.7 \text{ kg/m}^3 \end{aligned}$$

- the specific heat according to equation A.2

$$\begin{aligned} c_{ph} &= 8.15599 \times 10^3 - 2.80627 \times 10^1(295.3) + 5.11283 \times 10^{-2}(295.3)^2 - 2.17582 \times 10^{-13}(295.3)^6 \\ &= 4183.3 \text{ J/kg}\cdot\text{K} \end{aligned}$$

- the viscosity using equation A.3

$$\begin{aligned} \mu_c &= 2.414 \times 10^{-5} \times 10^{\frac{247.8}{(295.3)-140}} \\ &= 0.9510 \times 10^{-3} \text{ kg/m}\cdot\text{s} \end{aligned}$$

- the thermal conductivity according to equation A.4

$$\begin{aligned} k_{fc} &= -6.14255 \times 10^{-1} + 6.9962 \times 10^{-3}(295.3) - 1.01075 \times 10^{-5}(295.3)^2 + 4.74737 \times 10^{-12}(295.3)^4 \\ &= 0.60645 \text{ W/m}\cdot\text{K} \end{aligned}$$

- the Prandtl number according to equation A.5

$$\begin{aligned} Pr_c &= \frac{(0.9510 \times 10^{-3})(4183.3)}{(0.60645)} \\ &= 6.560 \end{aligned}$$

APPENDIX D. SAMPLE CALCULATIONS

Similarly for the annular (hot) stream with $T_{hm} = 307.10 \text{ K}$ find

$$\begin{aligned}\rho_h &= 994.5 \text{ W/m}\cdot\text{K} \\ c_{ph} &= 4177.3 \text{ J/kg}\cdot\text{K} \\ \mu_h &= 0.734 \times 10^{-3} \text{ kg/m}\cdot\text{s} \\ k_{fh} &= 0.62326 \text{ W/m}\cdot\text{K} \\ Pr_h &= 4.919\end{aligned}$$

The cold mass flux is evaluated as

$$\begin{aligned}m_c &= \rho_c V_c = (997.7)(0.79) \left| \frac{1}{\text{s}} \right| \left| \frac{1}{1000 \text{ l}} \right| \\ &= 0.7881 \text{ kg/s}\end{aligned}$$

The hot stream mass flow rate is

$$\begin{aligned}m_h &= (994.5)(0.61) \left| \frac{1}{\text{s}} \right| \left| \frac{1}{1000 \text{ l}} \right| \\ &= 0.5761 \text{ kg/s}\end{aligned}$$

The flow cross-sectional area of the cold stream is calculated using the coated internal diameter

$$\begin{aligned}A_c &= \frac{\pi d_2^2}{4} = \frac{\pi(0.023125)}{4} \\ &= 0.4200 \times 10^{-3} \text{ m}^2\end{aligned}$$

The cross-sectional area of the annulus is found to be

$$\begin{aligned}A_{ann} &= \frac{\pi(d_4^2 - d_3^2)}{4} = \frac{\pi(0.03355^2 - 0.02534^2)}{4} \\ &= 0.3797 \times 10^{-3} \text{ m}^2\end{aligned}$$

which means the velocity of the cold stream is

$$\begin{aligned}v_c &= \frac{0.79}{0.4200 \times 10^{-3}} \left| \frac{1}{\text{s}} \right| \left| \frac{1}{1000 \text{ l}} \right| \\ &= 1.881 \text{ m/s}\end{aligned}$$

And for the annulus

$$\begin{aligned}v_{ann} &= \frac{0.61}{0.3797 \times 10^{-3}} \left| \frac{1}{\text{s}} \right| \left| \frac{1}{1000 \text{ l}} \right| \\ &= 3.996 \text{ m/s}\end{aligned}$$

APPENDIX D. SAMPLE CALCULATIONS

From equation 2.11 the Reynolds number characterizing the cold stream is

$$Re_c = \frac{(997.7)(1.881)(0.023125)}{0.9510 \times 10^{-3}} = 45628$$

which is indeed fully turbulent. Thus the friction factor can be evaluated using equation 2.13

$$f_{D,c} = [1.8 \log_{10}(45628) - 1.5]^{-2} = 0.02109$$

Although constant properties have been assumed thus far, the temperature dependence of the viscosity can be accounted for by multiplying the internal Nusselt number by a correction factor. Petukhov (1970), cited by Kröger (1998) found this correction factor to be

$$M = \left(\frac{Pr}{Pr_w} \right)^{0.11}$$

where Pr_w is the Prandtl number evaluated at the average wall temperature. This temperature is found following an iterative solution, however, it will be shown that the resultant value is 28.02 °C. At this temperature find

- the specific heat according to equation A.2

$$\begin{aligned} c_{pw} &= 8.15599 \times 10^3 - 2.80627 \times 10^1 (301.2) + 5.11283 \times 10^{-2} (301.2)^2 - 2.17582 \times 10^{-13} (301.2)^6 \\ &= 4179.5 \text{ J/kgK} \end{aligned}$$

- the viscosity using equation A.3

$$\begin{aligned} \mu_w &= 2.414 \times 10^{-5} \times 10^{\frac{247.8}{(301.2)-140}} \\ &= 0.8325 \times 10^{-3} \text{ kg/m}\cdot\text{s} \end{aligned}$$

- the thermal conductivity according to equation A.4

$$\begin{aligned} k_{fw} &= -6.14255 \times 10^{-1} + 6.9962 \times 10^{-3} (307.0) - 1.01075 \times 10^{-5} (307.0)^2 + 4.74737 \times 10^{-12} (307.0)^4 \\ &= 0.6151 \text{ W/m}\cdot\text{K} \end{aligned}$$

- the Prandtl number according to equation A.5

APPENDIX D. SAMPLE CALCULATIONS

$$Pr_w = \frac{(0.7813 \times 10^{-3})(4178.2)}{0.6192} = 5.656$$

The correction factor is then

$$M = \left(\frac{6.560}{5.656} \right)^{0.11} = 1.016$$

The inner Nusselt number is calculated by multiplying equation (2.22) by this correction factor, in which case

$$Nu_i = \frac{\left(\frac{0.02109}{8} \right) (45628)(6.560)}{1 + 12.7 \left(\frac{0.02109}{8} \right)^{0.5} ((6.560)^{2/3} - 1)} \times 1.016 = 304.5$$

This means that the inner convection coefficient is

$$\begin{aligned} h_i &= \frac{k_{fh}}{d_e} \cdot Nu_i \\ &= \frac{0.62326}{0.023125} \times 304.5 \\ &= 7987.5 \text{ W/m}^2 \cdot \text{K} \end{aligned}$$

From equations (4.1) and (4.2), the averaged mean temperature differences are respectively:

$$\Delta \bar{T}_{hm} = 0.5 [2.657 + (35.282 - 32.618)] = 2.661 \text{ K}$$

and

$$\Delta \bar{T}_{cm} = 0.5 [2.052 + (23.185 - 21.149)] = 2.044 \text{ K}$$

That means the averaged mean heat transfer rate from equation (4.3) is

$$\begin{aligned} Q_m &= 0.5 [(994.5)(0.6069)(4177.36)(2.661) + (997.7)(0.7899)(4183.3)(2.044)] \\ &= 6723.9 \text{ W} \end{aligned}$$

The outer convection coefficient is calculated according to equation 4.5

$$\begin{aligned} Nu_{ann} &= \frac{0.03355 - 0.02534}{0.62326 \times \pi(0.02534)(1.981)} \times \left[\frac{308.4 - 296.3 - (305.8 - 294.3)}{6723.9 \ln \left(\frac{308.4 - 296.3}{305.8 - 294.3} \right)} \right. \\ &\quad \left. - \frac{1}{\pi(1.981)(0.6064)(304.5)} - \frac{\ln \frac{0.02534}{0.023125}}{2\pi(120)(1.981)} \right]^{-1} \\ &= 101.5 \end{aligned}$$

Finally the wall temperature is verified using

$$\begin{aligned} T_w &= T_{cm} + \frac{Q}{h_{ann}A} \\ &= 295.3 + \frac{6723.9}{7987.5 \times \pi 0.023125 \times 1.981} \\ &= 301.1 \text{ K (28.00 } ^\circ\text{C)} \end{aligned}$$

APPENDIX D. SAMPLE CALCULATIONS

D.2 Analysis of coated tube 15C

The geometry and recorded test data of test number 040308 are:

Effective heat transfer length	L	=	1.981 m
Annulus diameter	d_4	=	0.03355 m
Tube outer diameter	d_3	=	0.02534 m
Tube inner diameter	d_2	=	0.023125 m
Coating internal diameter	d_1	=	0.023032 m
Cold inlet temperature	T_{ci}	=	21.227 °C
Cold outlet temperature	T_{co}	=	23.565 °C
Annulus inlet temperature	T_{hi}	=	35.469 °C
Annulus outlet temperature	T_{ho}	=	33.726 °C
Cold volumetric flow rate	V_c	=	0.782 l/s
Hot volumetric flow rate	V_h	=	1.062 l/s
Hot temperature difference	ΔT_h	=	1.803 K
Cold temperature difference	ΔT_c	=	2.366 K
Thermal conductivity of tube	k_t	=	120 W/m·K
Pressure drop	Δp	=	3835 Pa
Length between pressure tapings	$L_{\Delta p}$	=	2.598 m
Coefficient	A_{Nu}	=	0.0134
Exponent	B_{Nu}	=	0.8646

The bulk mean temperature of the cold stream is

$$T_{cm} = \frac{21.227 + 23.565}{2} + 273.15 = 295.6 \text{ K}$$

Evaluating the thermophysical property data at this temperature yields:

- the density using equation A.1

APPENDIX D. SAMPLE CALCULATIONS

$$\rho_c = 997.6 \text{ kg/m}^3$$

- the specific heat according to equation A.2

$$c_{pc} = 4183.1 \text{ J/kgK}$$

- the viscosity using equation A.3

$$\mu_c = 0.946 \times 10^{-3} \text{ kg/m}\cdot\text{s}$$

- the thermal conductivity according to equation A.4

$$k_{fc} = 0.6068 \text{ W/m}\cdot\text{K}$$

- the Prandtl number according to equation A.5

$$Pr_c = 6.52$$

Similarly for the hot stream with $T_{hm} = 308.01 \text{ K}$ find

$$\rho_h = 994.3 \text{ W/m}\cdot\text{K}$$

$$c_{ph} = 4177.2 \text{ J/kgK}$$

$$\mu_h = 0.724 \times 10^{-3} \text{ kg/m}\cdot\text{s}$$

$$k_{fh} = 0.6241 \text{ W/m}\cdot\text{K}$$

$$Pr_h = 4.85$$

The cold mass flow rate is evaluated as

$$\begin{aligned} m_c &= \rho_c V_c \\ &= (997.6)(0.782) \left| \frac{1}{\text{s}} \right| \left| \frac{1}{1000 \text{ l}} \right| \\ &= 0.7801 \text{ kg/s} \end{aligned}$$

The hot stream mass flow rate is

$$\begin{aligned} m_h &= (994.3)(1.062) \left| \frac{1}{\text{s}} \right| \left| \frac{1}{1000 \text{ l}} \right| \\ &= 1.056 \text{ kg/s} \end{aligned}$$

The flow cross-sectional area of the cold stream is calculated using the coated internal diameter

$$\begin{aligned} A_c &= \frac{\pi d_1^2}{4} = \frac{\pi(0.023037)}{4} \\ &= 0.4168 \times 10^{-3} \text{ m}^2 \end{aligned}$$

APPENDIX D. SAMPLE CALCULATIONS

The cross-sectional area of the annulus is found to be

$$A_h = \frac{\pi (d_4^2 - d_3^2)}{4} = \frac{\pi (0.03355^2 - 0.02534^2)}{4} \\ = 0.3797 \times 10^{-3} \text{ m}^2$$

which means the velocity of the cold stream is

$$v_c = \frac{0.782}{0.4168 \times 10^{-3}} \left| \frac{1}{\text{s}} \right| \left| \frac{1}{1000 \text{ l}} \right| = 1.876 \text{ m/s}$$

And for the annulus

$$v_{ann} = \frac{1.602}{0.3797 \times 10^{-3}} \left| \frac{1}{\text{s}} \right| \left| \frac{1}{1000 \text{ l}} \right| = 2.797 \text{ m/s}$$

From equation 2.11 the Reynolds number characterizing the cold stream is

$$Re_c = \frac{(997.6)(1.876)(0.023037)}{0.9116 \times 10^{-3}} = 45586$$

which is indeed fully turbulent. Thus the friction factor can be evaluated using equation 2.13

$$f_{D,c} = [1.8 \log_{10}(45586) - 1.5]^{-2} = 0.02109$$

This is compared to the measured value (equation 2.12), viz.

$$f_{D,c} = \frac{4017}{\left(\frac{2.598}{0.23037}\right) \left(\frac{(997.6)(1.876)^2}{2}\right)} = 0.02029$$

This represents a 3.8 % difference with the theoretical smooth tube value.

Once again the wall temperature requires an iterative solution. However, it will now be shown that the resultant value is 29.09 °C. At this temperature find

- the specific heat according to equation A.2

$$c_{pw} = 8.15599 \times 10^3 - 2.80627 \times 10^1 (302.3) + 5.11283 \times 10^{-2} (302.3)^2 - 2.17582 \times 10^{-13} (302.3)^6 \\ = 4179.0 \text{ J/kgK}$$

- the viscosity using equation A.3

$$\mu_w = 2.414 \times 10^{-5} \times 10^{\frac{247.8}{[(302.3)^{-1.40}]} } = 0.8122 \times 10^{-3} \text{ kg/m}\cdot\text{s}$$

- the thermal conductivity according to equation A.4

APPENDIX D. SAMPLE CALCULATIONS

$$\begin{aligned}
 k_{fw} &= -6.14255 \times 10^{-1} + 6.9962 \times 10^{-3} (302.3) \\
 &\quad - 1.01075 \times 10^{-5} (302.3)^2 + 4.74737 \times 10^{-12} (302.3)^4 \\
 &= 0.6166 \text{ W/m}\cdot\text{K}
 \end{aligned}$$

- the Prandtl number according to equation A.5

$$Pr_w = \frac{(0.8122 \times 10^{-3})(4179)}{(0.6166)} = 5.504$$

The correction factor is then

$$M = \left(\frac{6.521}{5.504} \right)^{0.11} = 1.019$$

The inner Nusselt number is calculated by multiplying equation (2.22) by this correction factor, in which case

$$Nu_i = \frac{\left(\frac{0.02109}{8} \right) (45600) (6.521)}{1 + 12.7 \left(\frac{0.02109}{8} \right)^{0.5} ((6.521)^{2/3} - 1)} \times 1.016 = 304.4$$

This means that the inner convection coefficient is

$$h_i = \frac{k_{fh}}{d_e} \cdot Nu_i = \frac{0.62326}{0.023032} \times 304.4 = 8018.6 \text{ W/m}^2\cdot\text{K}$$

From equations (4.1) and (4.2), the averaged mean temperature differences are respectively:

$$\Delta \bar{T}_{hm} = 0.5 [1.803 + (35.469 - 33.726)] = 1.773 \text{ K}$$

and

$$\Delta \bar{T}_{cm} = 0.5 [2.366 + (23.565 - 21.227)] = 2.352 \text{ K}$$

That means the averaged mean heat transfer rate from equation (4.3) is

$$\begin{aligned}
 Q_m &= 0.5 [(994.3)(1.062)(4177.2)(2.352) + (997.6)(0.782)(4183.31)(2.352)] \\
 &= 7748 \text{ W}
 \end{aligned}$$

The Reynolds number of the annulus is

$$Re_h = \frac{(994.3)(2.797)(0.03355 - 0.02534)}{0.7244 \times 10^{-3}} = 31509$$

APPENDIX D. SAMPLE CALCULATIONS

Consolidating the above terms, the thermal conductivity is calculated according to equation 2.37

$$\begin{aligned}
 k_c &= \frac{\ln\left(\frac{0.023125}{0.023032}\right)}{2\pi(1.981)} \times \left\{ \frac{(35.469 - 23.565) - (33.726 - 21.227)}{7748 \times \ln\left(\frac{35.469-23.565}{33.726-21.227}\right)} \right. \\
 &\quad - (\pi \times 1.981 \times 0.6068 \times 304.4) - \frac{\ln\left(\frac{0.02534}{0.023125}\right)}{2\pi \times 120 \times 1.981} \\
 &\quad \left. - \left[\frac{\pi \times 0.02534 \times 1.981 \times 0.6241}{(0.03355 - 0.02534)} \times 0.01336 \times (45874.6^{0.8646} 4.823^{0.3}) \right]^{-1} \right\}^{-1} \\
 &= \underline{2.13 \text{ W/m}\cdot\text{K}}
 \end{aligned}$$

The effective tube-coating conductivity using equation (2.40) is

$$\begin{aligned}
 k_{eff} &= \frac{\ln\left(\frac{0.02534}{0.023032}\right)}{2\pi \times 1.981} \left[\frac{(35.469 - 23.565) - (33.726 - 21.227)}{7748 \times \ln\left(\frac{35.469-23.565}{33.726-21.227}\right)} \right. \\
 &\quad \left. - \left(\frac{\pi \times 0.02534 \times 1.981 \times 0.6241}{0.03355 - 0.02534} \times 0.01336 \times 45874.6^{0.8646} 4.823^{0.3} \right)^{-1} \right. \\
 &\quad \left. - (\pi \times 1.981 \times 0.6068 \times 304.4)^{-1} \right]^{-1} \\
 &= 45.43 \text{ W/m}\cdot\text{K}
 \end{aligned}$$

and similarly using equation (2.38) the coating factor is

$$\begin{aligned}
 R''_{fc} &= \pi \times 0.023125 \times 1.981 \times \left[\frac{(35.469 - 23.565) - (33.726 - 21.227)}{7748 \times \ln\left(\frac{35.469-23.565}{33.726-21.227}\right)} \right. \\
 &\quad \left. - \left(\frac{\pi \times 0.02534 \times 1.981 \times 0.6241}{0.03355 - 0.02534} \times 0.01336 \times 31509.4^{0.8646} 4.848^{0.3} \right)^{-1} \right. \\
 &\quad \left. - \frac{\ln\left(\frac{0.02534}{0.023125}\right)}{2\pi \times 120 \times 1.981} - (\pi \times 1.981 \times 0.6068 \times 304.4)^{-1} \right] \\
 &= 2.03 \times 10^{-5} \text{ W/K}
 \end{aligned}$$

Finally the wall temperature is verified using

$$\begin{aligned}
 T_w &= T_{cm} + \frac{Q}{h_i A_i} \\
 &= 295.5 + \frac{7748.3}{8018.6 \times \pi \times 0.023032 \times 1.981} \\
 &= 302.2 \text{ K (29.09 } ^\circ\text{C)}
 \end{aligned}$$

APPENDIX D. SAMPLE CALCULATIONS

D.3 Calculating the heat transfer coefficient using the HEI method

Based on the HEI standard, the heat transfer coefficient is calculated by first determining the cooling water velocity. The velocity in each tube is determined by dividing the total volumetric flow rate by the cross-sectional area:

$$v_c = \frac{6.86}{8400 \times \pi \times 0.02291^2 / 4} = 1.981 \text{ m/s}$$

The velocity in imperial units is then

$$v_c = 1.981 \left| \frac{\text{ft/s}}{3.048 \times 10^{-1} \text{ m/s}} \right| = 6.489 \text{ ft/s}$$

The uncorrected heat transfer coefficient U_1 can then be obtained from table 1 of the HEI standard at this velocity, thus

$$U_1 = 670.5 \text{ BTU/hr} \cdot \text{ft}^2 \cdot ^\circ\text{F}$$

The inlet water temperature and material correction factors, from tables 2 and 3 of the HEI standard, are respectively

$$F_W = 1$$

$$F_M = 0.988$$

The corrected heat transfer is thus

$$\begin{aligned} U_{HEI} &= 670.5 \times 0.998 \times 1 \\ &= 669.2 \text{ BTU/hr} \cdot \text{ft}^2 \cdot ^\circ\text{F} \left| \frac{5.678263 \text{ W/K}}{\text{BTU/hr}} \right| \\ &= 3800 \text{ W/K} \end{aligned}$$

The surface area based on the outer diameter of the tubes is

$$A_s = \pi 0.0254 \times 9 \times 8400 = 6032.6 \text{ m}^2$$

The product between the corrected heat transfer coefficient and the surface area is

$$U_{HEI} A_s = 3803 \times 149161 = 22.92 \times 10^6 \text{ W/K}$$

The outlet water temperature is iteratively calculated. It will be shown that $T_{co} = 30.38 \text{ }^\circ\text{C}$ satisfies this iteration.

APPENDIX D. SAMPLE CALCULATIONS

The mean water temperature is

$$T_{mc} = \frac{21.11 + 30.38}{2} + 273.15 = 298.9 \text{ K}$$

Using this temperature the thermophysical property data is: $\rho_c = 996.9 \text{ kg/m}^3$, $c_{pc} = 4180.8 \text{ J/kg}\cdot\text{K}$, $\mu_c = 0.0008755 \text{ kg/m}\cdot\text{s}$ From equation (2.4)

$$\begin{aligned} T_{co} &= 294.3 + \frac{265.1 \times 10^6}{996.9 \times \pi \times \frac{0.02291^2}{4} \times 1.981 \times 8400 \times 4180.8} \\ &= 303.53 \text{ K (30.38 } ^\circ\text{C)} \end{aligned}$$

D.4 Calculating γ in the thermal resistance model

The solution requires an iterative procedure. It will now be verified that the values: $T_s = 37.93 \text{ } ^\circ\text{C}$, $T_{lv} = 33.44 \text{ } ^\circ\text{C}$, $T_w = 28.96 \text{ } ^\circ\text{C}$, and $\gamma = 0.4928$ satisfy the governing equations.

D.4.1 Waterside

The waterside Reynolds number is

$$Re_c = \frac{996.86 \times 1.981 \times 0.02291}{0.8755 \times 10^{-3}} = 51\,684.6$$

and from equation (2.13)

$$f_D = (1.8 \log_{10}(51684.6) - 1.5)^{-2} = 0.02077$$

To account for developing flow, the convection coefficient is evaluated using equation (2.23), therefore

$$\begin{aligned} h_c &= \left(\frac{0.6118}{0.02291} \right) \cdot \frac{\left(\frac{0.02077}{8} \right) (51684.6 - 1000) 5.982 \left[1 + \left(\frac{0.02291}{9} \right)^{0.67} \right]}{1 + 12.7 \left(\frac{0.02077}{8} \right)^{0.5} (5.982^{2/3} - 1)} \\ &= 8569.3 \text{ W/m}\cdot\text{K} \end{aligned}$$

APPENDIX D. SAMPLE CALCULATIONS

D.4.2 Steamside

The steam temperature is calculated according to

$$\begin{aligned} T_s &= \frac{T_{ci} - T_{co} e^{[U_{HEIAs}(T_{co}-T_{ci})/Q_{duty}]} }{1 - T_{co} e^{[U_{HEIAs}(T_{co}-T_{ci})/Q_{duty}]} } \\ &= \frac{294.26 - 303.53 e^{[22.921 \times 10^6 (303.53 - 22.921) / 265.1 \times 10^6]} }{1 - 303.53 e^{[22.921 \times 10^6 (303.53 - 22.921) / 265.1 \times 10^6]} } \\ &= 311.08 \text{ K (37.93 } ^\circ\text{C)} \end{aligned}$$

Which means from equation (A.7) the saturation pressure is

$$\begin{aligned} z &= 10.79586(1 - 273.16/311.08) + 5.2808 \log_{10}(273.16/311.08) \\ &\quad + 1.50474 \times 10^{-4} \{1 - 10^{-8.29692[(311.08/273.16)-1]}\} \\ &\quad + 4.2873 \times 10^{-4} \{10^{4.76955(1-273.16/311.08)} - 1\} + 2.78618312 \\ &= 3.8196 \end{aligned}$$

and

$$p_{sat} = 10^3 \cdot 3.8196 = 6600.8 \text{ Pa}$$

Multiplying this by the steam quality, the steam pressure is

$$\begin{aligned} p_s &= 0.94 \times 6600.8 \\ &= 6204.8 \text{ Pa} \end{aligned}$$

Using equation (5.10) the mixture pressure is

$$\begin{aligned} p_{mix} &= \left[1 + 0.622 \left(\frac{0.0005}{1 - 0.0005} \right) \right] \times 6204.8 \\ &= 6598 \text{ Pa} \end{aligned}$$

Evaluating the thermophysical properties of the air-steam mixture using equations (A.8) and (A.9) yields the following results: $\rho_{mix} = 0.07386 \text{ kg/m}^3$, $\mu_{mix} = 0.0000190 \text{ kg/m}\cdot\text{s}$. Also the diffusion coefficient from equation (5.8) is $0.0004106 \text{ m}^2/\text{s}$.

The average film temperature is

$$\begin{aligned} T_f &= 0.5(33.44 + 28.96) + 273.15 \\ &= 304.35 \text{ K} \end{aligned}$$

and the condensate properties evaluated at this temperature are: $\rho_l = 995.3 \text{ kg/m}^3$, $\mu_l = 0.7772 \times 10^{-3} \text{ kg/s}\cdot\text{m}$, $c_{pl} = 4178.14 \text{ J/kg}\cdot\text{K}$ and $Pr_l = 5.241$.

APPENDIX D. SAMPLE CALCULATIONS

The latent heat of vaporization from equation (A.6) is then

$$\begin{aligned} i_{fg} &= 3.4831814 \times 10^6 - 5.8627703 \times 10^3 (311.08) + 12.139568 (311.08)^2 - 0.0140290431 (311.08)^3 \\ &= 2.4118354 \times 10^6 \text{ J/kg} \end{aligned}$$

in which case the modified latent heat of vaporization is

$$\begin{aligned} i_{fg}^* &= 2.4118354 \times 10^6 + 0.68 \times 4178.14 (304.35 - 302.1) \\ &= 2.4245774 \times 10^6 \text{ J/kg} \end{aligned}$$

Now u_∞ is approximated from the conditions at the turbine neck (cross-sectional area equal to $6.1 \times 9 = 54.9 \text{ m}^2$)

$$\begin{aligned} u_\infty &= \frac{265.1 \times 10^6}{0.04606 \times 54.9 \times 2.4245774 \times 10^6} \\ &= 43.238 \text{ m/s} \end{aligned}$$

And the modified mean velocity becomes

$$u' = 0.6268 \times 43.238 = 27.102$$

The mixture Reynolds number is evaluated in terms of the velocity,

$$\begin{aligned} Re_{mix} &= \frac{0.07386 \times 27.102 \times 0.0254}{0.0000190} \\ &= 2680.3 \end{aligned}$$

Now the resistance due to the presence of air (equation 5.7) is

$$\begin{aligned} R_a &= \left[0.82 \frac{D_{as}}{d_3} Re_{mix}^{0.5} \left(\frac{p_{mix} - p_s}{p_{mix}} \right)^{-0.6} p_{mix}^{1/3} \left(\frac{\rho_s i_{fg}^*}{T_s} \right)^{2/3} \frac{1}{T_s - T_{cv}}^{1/3} \right]^{-1} \\ &= 19.95 \times 10^{-6} \text{ m}^2 \cdot \text{K/W} \end{aligned}$$

The gravity dominated component of the steam-side convection coefficient (equation 5.3)

$$\begin{aligned} h_g &= 0.728 \left[\frac{9.81 \times 995.3^2 \times 2.4245774 \times 10^6 \times 0.61952^3}{0.7772 \times 10^{-3} \times 0.0254 \times (306.59 - 302.1)} \right]^{1/4} \\ &= 11543.1 \text{ W/m}^2 \cdot \text{K} \end{aligned}$$

and the shear component (equation 5.6)

$$\begin{aligned} h_{sh} &= \frac{0.6195}{0.0254} \cdot 0.59 \left(995.3 \times \frac{0.0254}{0.49 \times 0.7772 \times 10^{-3}} \times 27.102 \right)^{0.5} \\ &= 19303.1 \text{ W/m}^2 \cdot \text{K} \end{aligned}$$

APPENDIX D. SAMPLE CALCULATIONS

These results are combined in equation (5.5) to yield the mean steam side convection coefficient

$$\begin{aligned}\bar{h} &= 100^{-0.16} \left[0.5 \times 19303.1^2 + (0.25 \times 19303.1^4 + 11543.1^4)^{0.5} \right]^{\frac{1}{2}} \\ &= 9798.5 \text{ W/m}^2 \cdot \text{K}\end{aligned}$$

The mean steam-side convection coefficient can be used to verify the condensate-vapor interface temperature

$$\begin{aligned}T_{lv} &= T_s - \frac{Q_{\text{duty}}}{\bar{h}A_s} \\ &= 311.08 - \frac{265.1 \times 10^6}{9798.5 \times 6032.6} \\ &= 306.6 \text{ K (33.45 }^\circ\text{C)}\end{aligned}$$

Now the overall heat transfer coefficient from equation (5.14) is

$$\begin{aligned}\bar{U} &= \left[19.95 \times 10^{-6} + 9798.5^{-1} + \frac{\ln \frac{0.0254}{0.02291}}{2 \times 111/0.0254} + (8569.3 \times 0.02291/0.0254)^{-1} \right]^{-1} \\ &= 3800 \text{ W/K}\end{aligned}$$

which is equal to the HEI value.

D.5 Actual turbine data from a particular power station

The figure below shows the steam temperature versus output for a particular turbine Eskom Technology Group, Eskom Enterprises (2013).

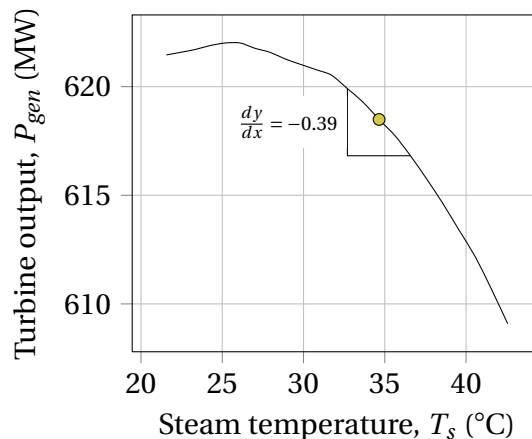
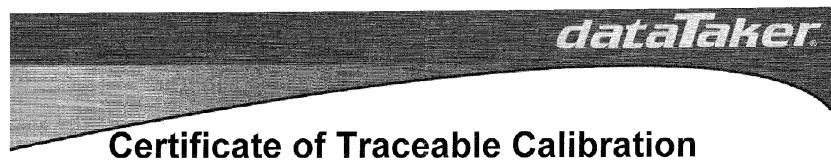


Figure D.1: Power output versus steam temperature from an actual power plant

Appendix E

Instrument certification

The relevant instruments of calibration for each instrument are included below.



Product Description

Model: DT80-2
 Serial: 088945
 Kernel Assembly: AS1208B0 1421-047
 Terminal Assembly: AS1210B0 1418-239
 Firmware: 80 Version 7.12.0001

Calibration Details

Calibration Date: 2010/02/03 13:33:58
 Test Location: Unit 7, 2 Pinnacle Street Brendale QLD 4500
 Ambient Temperature: 24.5 °C
 NATA Certified Reference: Fluke 8840A Serial 5141011
 Calibration Reference: DT80 Tester JIG-250 Version 1.44.0000, Calibrated 2010/02/01 10:32:12

Calibration Results

The following table lists measurements performed against traceable references.

Range	Channel(options)	Reference	Actual Reading	Allowable Error ¹	Error	Status
+30 V	1+HV(GL30V)	+2.4965 V	+2.4966	± 0.1 %	0.005 %	PASS
+3000 mV	1*V(GL3V)	+2501.0 mV	+2500.9	± 0.1 %	-0.002 %	PASS
+300 mV	1+V(GL300MV)	+250.10 mV	+250.11	± 0.1 %	0.004 %	PASS
+30 mV	1-V(GL30MV)	+25.014 mV	+25.013	± 0.1 %	-0.003 %	PASS
-30 V	1+HV(GL30V)	-2.4965 V	-2.4975	± 0.1 %	0.040 %	PASS
-3000 mV	1*V(GL3V)	-2501.1 mV	-2501.7	± 0.1 %	0.025 %	PASS
-300 mV	1+V(GL300MV)	-250.11 mV	-250.15	± 0.1 %	0.017 %	PASS
-30 mV	1-V(GL30MV)	-25.010 mV	-25.016	± 0.1 %	0.024 %	PASS
10 k Ω	1R(4W,I)	100.0055 Ω	100.013	± 0.2 %	0.008 %	PASS

¹Allowable Error indicates the maximum allowable difference between the Reference and the Actual Reading, specified as a percentage of the Actual Reading, when the ambient temperature is between 5°C and 40°C.

The product covered by this certificate meets or exceeds the required performance specified by Thermo Fisher Scientific Australia Pty. Ltd.

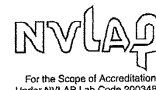
The measurements performed to generate this certificate are traceable to Australian national standards of measurement.

This product has been manufactured under an ISO9001:2008 quality system.

APPENDIX E. INSTRUMENT CERTIFICATION

Fluke Corporation-
Hart Scientific Division
799 E Utah Valley Drive
American Fork, Utah 84003-9775

Report of Calibration



Model: 1551A	Serial No.: 1635062	Customer: Fluke Nederland B.V.
Description: Digital Thermometer with Probe		Son 5692
Received Condition: New		NL
Procedure: HCC132 - 0		As Left Condition: In Tolerance

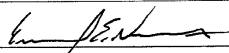
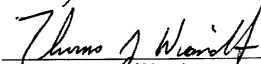
The above referenced digital thermometer was calibrated by comparison to a laboratory standard precision digital thermometer readout and Standard Platinum Resistance Thermometer (SPRT) at the temperatures indicated on page 2 of this report. Routine calibration consists of As Found data collection, alignment, and As Left data collection. The As Left data was taken with new coefficients programmed into the instrument.

All known uncertainties have been considered and a Test Uncertainty Ratio (TUR) of at least 4:1 was maintained throughout the calibration unless otherwise indicated. This calibration is traceable to NIST, radiometric techniques, or natural physical constants and is in compliance with ANSI/ISO/IEC 17025:2005 and ANSI/NCCL Z540.1. This calibration report applies only to the item described. This calibration report shall not be used to claim product endorsement by NVLAP or any agency of the U.S. Government. Calibration reports without signatures are not valid.

Test Equipment

Instrument	Model	Serial No.	Recall Date
Precision Digital Thermometer	1595A	B17050	01/19/2012
SPRT, Metal Sheath	5699	0425	06/12/2012
SPRT, Metal Sheath	5699	0651	11/08/2013
SPRT, Metal Sheath	5699	0652	11/10/2013
SPRT, Metal Sheath	5699	0654	11/03/2013
155x Test Station		9	

Environmental Conditions:
Temperature: 23.1°C
Humidity: 40.4% RH
Calibration Date: 09/08/2011
Calibration Due: Not Defined
PO Number: 619012498-FCO-0/ZA/COMTE
Report Number: B1913022

Technician: 
Approved by: 
Director of Metrology

APPENDIX E. INSTRUMENT CERTIFICATION

Calibration Report

Model: 1551A
 Serial No.: 1635062
 Report No: B1913022

As Found Data

No As Found Data Required

As Left Data

Data ID: B1250161259901

Calibration Constants		Nominal (°C)	Actual (°C)	Measured (°C)	Error (°C)	Tolerance (°C)	Pass/Fail
R0	100.012216	-50	-50.0162	-50.0163	-0.0001	±0.0500	P
A	3.920511E-03	-25	-25.0077	-25.0129	-0.0052	±0.0500	P
B	-6.442960E-07	0	-0.0043	0.0041	0.0084	±0.0500	P
C	-7.695850E-12	100	99.9933	99.9925	-0.0008	±0.0500	P
MINOP	-60	157	157.0353	157.0358	0.0005	±0.0500	P
MAXOP	170						

Name	Reference	Offset
Device Calibration Constants		
DEVICE CAL 1	50.0090	0.0926
DEVICE CAL 2	100.0020	0.0862
DEVICE CAL 3	150.0080	0.0811
DEVICE CAL 4	200.0010	0.0820

User Calibration Constants		
USER CAL 1	-50.0000	0.0000
USER CAL 2	0.0000	0.0000
USER CAL 3	157.0000	0.0000

APPENDIX E. INSTRUMENT CERTIFICATION

Blanes **PRESSURE SOLUTIONS**
 P.O.Box 3357, Benoni 1500. 169, Elston Ave, Benoni, 1501, Gauteng, South Africa
 Phone 422-1749/1840 Fax 421-5379 Dial code international +2711 local 011
 E-mail: rod@pressuresolutions.co.za Web: www.pressuresolutions.co.za

TEST CERTIFICATE No. AK5150

Test of Bailey & Mackey Differential Pressure Transmitter, serial No. 12C2708.1 Tag No. None, Range 0 – 100 mbar,

Conducted for Transducer Technology at Benoni on Thursday, October 18, 2012.

Act No. 18 Notice: The pressure standard used was an air deadweight tester, serial no. 13375/D701, traceable to SA National Standards. The relevant certificate is 0511P718-1 issued by SANAS Accredited Calibration Laboratory No.205 with an uncertainty of 0,04% of pressure generated. The weights are not compensated for local gravity, so gravitational correction has been done as laid out below.

The current standard used was an Ametek calibrator, serial no. 537491-04875, traceable to SA National Standards. The relevant certificate is 20463 issued by SANAS Accredited Calibration Laboratory No.101 with an uncertainty of 2µA.

Test Conditions: Local Gravity 9,7853 m/s² Temperature 21 °C

Applied Pressure (kPa)	Corrected Pressure (kPa)	Calculated Signal (mA)	Rising Pressure Signal (mA)	Falling Pressure Signal (mA)
0	0	4,000	4,039	4,148
5	4,989	11,983	12,180	12,310
10	9,978	19,965	30,371	20,415

Comments:
 Certified Correct as Stated above

For Blanes Pressure Solutions CC


 Authorised Signatory

Z:\My Documents\Certificates\ak5150.docx
 Page 1 of 1
 2002/092848/23
 RAC McLeman Bsc.Mech.Eng. B.Com.

Products for Pressure Professionals

APPENDIX E. INSTRUMENT CERTIFICATION

FLOWMETRIX SA CC

P.O.Box 17143 Congella 4013 Tel 031-2060630 Fax 031-2060635

C E R T I F I C A T E O F C A L I B R A T I O N

Certificate # 20122636

Calibration of MAGNETIC FLOWMETER

Make : 25mm SAFMAG
Type : 025B2HDSSR003W
Serial No. : FMX16581
Range : 0 - 4 l/s

- REFERENCE EQUIPMENT -

Reference Converter : BETA
Serial No. : 05098318
Reference Meter : No 1
Check Meter : 40mm MAG

- ENVIRONMENT / PIPEWORK -

Liquid temperature : 26.7 deg.C
Upstream / Downstream ID : 25mm

Non-adherence to the above pipe ID could introduce measurement errors.

- PROCEDURE -


By reference to 270 - 500 secs

- DATE OF CALIBRATION -

Calibration performed on 13-12-2011

- UNCERTAINTY OF MEASUREMENT -

Uncertainty of measurement is $\pm 0.5\%$

Calibrated by S.KEOGH 

Checked by 

APPENDIX E. INSTRUMENT CERTIFICATION

FLOWMETRIX SA CC

P.O.Box 17143 Congella 4013 Tel 031-2060630 Fax 031-2060635

CERTIFICATE OF CALIBRATION

Certificate # 20122638

Calibration of MAGNETIC FLOWMETER

Make : 25mm SAFMAG
Type : 025B2HDSSR003W
Serial No. : FMX16575
Range : 0 - 4 l/s

- REFERENCE EQUIPMENT -

Reference Converter : BETA
Serial No. : 05098318
Reference Meter : No 1
Check Meter : 40mm MAG

- ENVIRONMENT / PIPEWORK -

Liquid temperature : 28.2 deg.C
Upstream / Downstream ID : 25mm

Non-adherence to the above pipe ID could introduce measurement errors.

- PROCEDURE -

By reference to 270 - 500 secs

- DATE OF CALIBRATION -

Calibration performed on 13-12-2011

- UNCERTAINTY OF MEASUREMENT -

Uncertainty of measurement is $\pm 0.5\%$

Calibrated by S.KEOGH

Checked by